FH MÜNSTER
University of Applied Sciences

Bachelor Thesis

Development of an Inorganic Temperature Sensitive Paint for High Temperature Environments

by

Marlies Maroka
1062463

Department of Chemical Engineering

FH Münster University of Applied Sciences

September 20th, 2022

Primary Reviewer: Prof. Dr. Thomas Jüstel
Secondary Reviewer: Dr. Michael Hilfer

Eidesstaatliche Erklärung

Hiermit versichere ich, die vorliegende Bachelorarbeit selbstständig und nur unter Verwendung der von mir angegebenen Quellen und Hilfsmittel verfasst zu haben. Sowohl inhaltlich als auch wörtlich entnommene Inhalte wurden als solche kenntlich gemacht. Die Arbeit hat in dieser oder vergleichbarer Form noch keinem anderem Prüfungsgremium vorgelegen.

Datum: 20.09.2022 Unterschrift: Marlies Marska

Danksagung

Ich bedanke mich bei dem Institut Deutsches Zentrum für Luft- und Raumfahrt und bei allen Kollegen der Abteilung Experimentelles Verfahren für die Ermöglichung dieser Arbeit. Insbesondere danke ich Herrn Dr. Michael Hilfer für die Betreuung und Hilfestellung, die er stets geleistet hat.

Ebenso möchte ich mich herzlichst bei Prof. Dr. Thomas Jüstel für die Bereitstellung des Labors und Messequipments, für die hilfreichen fachlichen Antworten zu meinen Fragestellungen und vor allem für die Betreuung meiner Abschlussarbeit bedanken. An dieser Stelle gilt der Dank auch an Viktor Anselm, der mich tatkräftig während meiner Laborarbeit an der FH Münster betreut hat und darüber hinaus eine große Hilfe gewesen ist.

Ganz besonders möchte ich mich für die stetige Motivation und Unterstützung bei meiner Familie und meinen Kommilitonen und mittlerweile guten Freunden Daniel Tennhoff, Jan Alexander Rethmeier, Jendrik Kromminga, Malte Deters, Max Kalus und Miguel Mikosch bedanken. Ohne deren Rückhalt wäre mir das Studium in diesem Maße nicht gelungen.

Abstract

Temperature sensitive paint (TSP) is a measurement technique based on luminescent molecules which exhibit property change (i.e. increasing, decreasing emission intensity or luminescence lifetime) due to changing local temperature. It is used to measure surface temperature distributions and heat flow fields for specific temperature ranges with high spatial resolution. In recent years, much research has been carried out on organic luminophores for cryogenic and ambient temperatures and, more recently, on inorganic phosphor materials for a temperature range from 30 up to 230 °C at the German Aerospace Center in Göttingen. In this work, inorganic phosphor materials are investigated which exceed the upper temperature limit of organic luminophores. These include $((Sr_{1-x}Ca_x)AlSiN_3:Eu^{2+}$, $YVO_4:Dy^{3+}$, $Y(V,P)O_4Eu^{3+}$, $YAG:Eu^{3+}$, $YAG:Dy^{3+}$ and $LuAG:Dy^{3+}$ covering individual temperature ranges between 300 and 1300 °C. Excitation and emission spectra, reflectance spectra, particle size distributions, external quantum efficiencies, thermal quenching curves and powder X-ray diffraction patterns were measured to characterize the phosphors which proved to be suitable towards the development of a high temperature TSP.

The phosphors were mixed with liquid binder (Ceramabind 643-1, Ceramabind 800, ZAP Binder) and sprayed by an airbrush gun onto plates made of aluminum and a nickel-steel alloy. All sprayed samples were subjected to mechanical tests. Emission spectra as well as lifetime measurements were executed at 0 °C – 59 °C and 30 - 200 °C, respectively, to determine the suitability of this paint for aerodynamic experiments. However, it has been shown that there is an interaction between the binder and the phosphor, which causes a decrease in luminescence due to quenching processes. Nevertheless, an inorganic TSP made of $(Sr_{1-x}Ca_x)AlSiN_3:Eu^{2+}$ and Ceramabind 800 was successfully developed for a temperature range between 150 °C and 450 °C, which exhibits high emission intensities and a fast lifetime of ~ 1 µs due to the allowed interconfigurational $[Xe]4f^65d^1 \rightarrow [Xe]4f^7$ transition.

Contents

List of Figures

List of Tables

List of Abbreviations

CCD	charge-coupled device
CMOS	complementary metal oxide semiconductor
CTS	charge transfer state
CVD	chemical vapor deposition
d_{50} – value	median value
E	electronic excited state
E_A	activation energy
EQE	external quantum efficiency
$Eu(TTFA)_3$	europium(III) tristhenoyltrifluoroacetonate
FG	frequency generator
g	gerade
G	electronic ground state
h	Planck constant
HEG	High-Enthalpy Shock Tunnel
IC	internal conversion
ISC	intersystem crossing
J	total angular momentum
k_{nr}	temperature dependent non-radiative process
k_{nr0}	temperature independent non-radiative rate
k_{nr1}	temperature dependent non-radiative transition rate
L	total orbital angular momentum
LED	light-emitting diode
$Lu_3Al_5O_{12}:Dy^3$, $LuAG:Dy^{3+}$	dysprosium-doped lutetium aluminum garnet
m_l	magnetic quantum number
N_{em}	number of emitted photons
N_{abs}	number of absorbed photons
OV322	europium 1,3-diketone complex embedded in a polyurethane polymer
PL	photoluminescence
PMT	photomultiplier tube
PSP	pressure sensitive paint
PVD	physical vapor deposition
R	universal gas constant

r_0	equilibrium distance in the ground state
R-profile	roughness profile
R_z	value giving information on roughness of a surface
S	total spin
S_0	ground state
S_1, S_2	singlet state
SCASN :Eu^{2+}, $(Sr_{1-x}Ca_x)AlSiN_3:Eu^{2+}$	europium(II)-doped strontium calcium aluminum silicon nitride
SCS	solution combustion synthesis
T_1	triplet state
TQ	thermal quenching
TRIS	tris(hydroxymethyl)aminomethane
T_{sens}	temperature sensitivity
TSP	temperature sensitive paint
TTL	transistor-transistor logic
u	ungerade
VO_4^{3-}	orthovanadate anion
VR	vibrational relaxation
wt.-%	weight per cent
XRD	x-ray powder diffraction
$Y_3Al_5O_{12}:Dy^{3+}$, YAG:Dy^{3+}	dysprosium doped yttrium aluminum garnet
$Y_3Al_5O_{12}:Eu^{3+}$, YAG:Eu^{3+}	europium doped yttrium aluminum garnet
$YVO_4:Dy^{3+}$	dysprosium - doped yttrium vanadate
$YVO_4:Eu^{3+}$	europium - doped yttrium vanadate
ΔR	value of shifted parabolas relative to each other
τ	lifetime

1 Introduction

Aerospace systems are often affected by high ambient temperatures as well as blackbody background radiation, vibration, rotation, combustion process, pressures and noise [1], which leads together with limited available space to a limited number of conventional thermal sensors used to detect surface temperatures. To detect the effects of local temperature changes on exposed surfaces, temperature sensitive paint (TSP) is used as an alternative to conventional sensors. TSP consists of a luminescent material that is usually mixed with a binder and applied to the examined surface. The principle of this technique is based on the process of thermal quenching, also called fluorescence quenching.
Conventional thermal sensors have high model preparation costs and are deposited at discrete locations, which limit the spatial resolution. In contrast to this technique, TSP is an optical measurement technique and offers minimal-invasive and non-contact method and can be applied to the entire surface with high spatial resolution. TSPs can be used to investigate flow phenomena such as laminar-turbulent flow transition by determining surface temperature and heat transport. To increase the sensitivity, TSPs are used for a restricted temperature range of up to 200 K. For this reason, the development of a range of TSPs is required to cover temperature from 300 up to 1700 °C. So far, organic TSPs for cryogenic and ambient temperatures have been developed at DLR in Göttingen and successfully investigated on model surfaces in research and industrial measurements in wind tunnels. The research on inorganic TSPs up to 230 °C has been recently initiated at DLR Göttingen and this work is the continuation of this effort.

In this project, the goal is to develop high temperature TSPs covering ranges between 300 and 1300 °C. In addition, the prepared paint should fulfill the following criteria for a successful application:

- Stability of the paint under various environmental conditions
- Good adhesion
- Sprayability with an airbrush gun
- Wide temperature range
- High temperature sensitivity
- Short lifetime, which is at most 100 µs
- Sufficient intensity at high temperature
- Low roughness of the coating (R_z = 1 - 10 µm)

- Thin layer thickness (≤ 10 µm)
- λ_{ex} ≈ 365 - 500nm, λ_{em} ≈ 580 – 670 nm

A good adhesion, low roughness, a thin layer thickness and stability of the paint are essential requirements in order to enable application in wind tunnels and flight tests for hypersonic environments. The remaining criteria listed must be observed in order to be able to determine the heat transport and surface temperature with the given equipment. In order to fulfill all criteria, pre-tests have to be carried out in addition to the correct selection and combination of materials.
After researching suitable luminescent materials and binders, some of these were synthesized and characterized at the department of Chemical engineering of FH Münster University of Applied Sciences. Using different binders as well as varying the concentrations of the selected phosphors, these compositions were spray coated onto sample plates made of aluminum and a nickel-steel alloy, also called surgical steel. The plates were spectroscopically measured and subjected to lifetime measurements for a certain temperature range. Furthermore, mechanical tests such as the determination of roughness, adhesion and layer thickness were carried out.

2 Theoretical Background

2.1 Literature review

TSP was discovered in the 1980s by Paul Kolodner and J. Anthony Tyson when they measured the surface temperature of an integrated circuit using the luminescent material europium(III) thenoyltrifluoroacetone (EuTTA) embedded in a binder [2].

For temperature above 100 °C the TSP usually consists of a phosphor mixed with a non-oxygen permeable binder and are often diluted in a solvent. Oxygen impermeability of the binder is essential to suppress the pressure dependence of the TSP and thus to avoid oxygen quenching [3]. Furthermore, phosphors show significant sensitivity only for a certain temperature range, so the choice of the phosphor has to be adapted to the application area. For this purpose, a list of phosphors with their respective temperature range of sensitivity can be found in [4].

The TSP is painted on or applied to a surface by using an airbrush gun. By using an airbrush gun it is possible to create a homogeneous coating. In contrast to other coating methods such as the sol-gel method, physical vapor deposition (PVD) or chemical vapor deposition (CVD),

using an airbrush gun has the advantage that the phosphor synthesis and the preparation of the TSP are carried out in two separate steps, which allows numerous optimizations [4].

The preparation of TSP differs if using organic or inorganic luminescent materials and respective binders. Usually, the organic materials are used for cryogenic temperatures and up to a maximum of 300 °C, since above this temperature thermal decomposition occurs [5]. For this range, much research has been done on Eu^{3+} complexes such as $[Eu(TTFA)_3]$ as well as Ru complexes as tris(bipyridine)ruthenium(II) chloride. These were mixed with polymer binders such as modified nylon, dope (nitrocellulose lacquer) or polyurethanes [3]. To perform measurements over a temperature range from cryogenic temperatures up to 1700 °C [3], inorganic materials must be used as thermographic luminescent materials. Ceramic hosts such as garnets, oxysulfides, vanadates and oxides doped with rare earth or transition metal elements are used [3]. For high-temperature TSP, ceramic binders are used, mostly based on water, water-alcohol or on silica [6]. A few examined commercially available binders are listed in Table 1.

Table 1: List of commercially available binders [7–9]

Binder	Company	Composition
Respond 793	Coltronics Corporation	SiO_2
Respond 795	Coltronics Corporation	Al_2O_3
HPC	Zyp Coatings	$MgO\text{-}SiO_2$
LK	Zyp Coatings	$Li_2O\text{-}K_2O\text{-}SiO_2$

2.2 Application and use of TSP

The desired model surface is coated with it. To excite the TSP, illumination sources such as lasers, light-emitting diode (LED) arrays, ultraviolet (UV) lamps and xenon lamps which emit in the required wavelength are used [3]. When the TSP has been excited it shows a Stokes shifted emission. At higher temperatures, a decrease in the luminescence intensity is observed as well as a shorter lifetime, which describes the average time it takes for an excited electron to emit to a photon to reach a vibrational state of the ground state. As a result, the emission appears darker. These observations can be recorded using a detector such as the charge-coupled device (CCD), a complementary metal oxide semiconductor (CMOS) camera or a photomultiplier tube. The choice of the setup depends on the measurement technique. For surface temperature measurements the intensity-based method and lifetime-based method are used which are considered in more detail in the chapter 3.2.

Due to higher temperatures, intensity and lifetime measurements are limited by the available equipment when a high signal-to-noise ratio occurs or when the lifetimes become too fast to record them. Furthermore, there is a larger blackbody radiation with increasing temperature, which might make it difficult to separate it from the luminescent intensity [5] .

When the measurements are performed within the limits of the available equipment, TSP can be used for many applications. It is used in hypersonic wind tunnels such as in the High Enthalpy Shock Tunnel (HEG) Göttingen of DLR, where measurements are performed with different Mach and Reynold numbers as well as temperatures. In HEG it is possible to reproduce super- and hypersonic flow conditions to which space- and aircraft are subjected [10], for example during re-entry into the planets atmosphere [1]. Here, heat transfer and surface temperatures can be investigated with the help of TSP. Furthermore, the laminar-to-turbulent boundary-layer transition can be determined, since in the laminar flow the heat transfer coefficient is smaller than in the turbulent flow, resulting in a dark and a light region on the model. In the wind tunnel heat-flux measurements are performed as for example on a slender cone or on a hypersonic inlet ramp [2].

2.3 Response time of TSP

Since many flow conditions can be simulated in wind tunnels such as DLR's HEG with a test duration of only a few milliseconds at most, it is important that the TSP has a short response time to enable time-resolved measurement and for capturing high-speed phenomena [11]. A short response time of the TSP allows to resolve high frequencies up to 10 kHz. For this reason, the applied phosphor should have a short lifetime. At this point it should also be noted that the lifetime of the phosphor differs from the lifetime of the TSP consisting of the phosphor and binder due to quenching processes. Similarly, a thin film is necessary to reduce the diffusion time of temperature into the TSP, since the response time decreases with a smaller square of the film thickness [12]. However, with a thin film, the quantum efficiency of the phosphor should be sufficiently high and a suitable excitation source should be available to measure sufficient emission intensity.

For example, TSPs with a short lifetime of 100 µs allow the measurement of temperature changes at a frequency of 3.33 kHz. This value is referred to as the cutoff frequency and was divided by three because a gain or phase attenuation of -3 dB usually occurs when using a Bode plot. This gain attenuation is caused by unsteady temperature fluctuations and is used as a correction factor for the frequency response of the TSP [13]. Such frequency characteristics are shown in [14]

2.4 Blackbody radiation

A black body is an idealized body that absorbs all incident electromagnetic radiation of any wavelength and emits the maximum possible energy at any temperature. Thus, no real body can emit more thermal radiation than a black body. In this regard, Planck's radiation law describes the spectral intensity distribution of this blackbody radiation as a function of wavelength (λ) and is given in equation (1) [15, 16] .

$$I_s(\lambda) = \frac{2\pi hc^2}{\lambda^5} * \frac{1}{\exp\left(\frac{hc}{\lambda k_B T}\right) - 1} \quad (1)$$

In addition to this law, Wien's shift law states that the wavelength at which the maximum of the radiation lies is inversely proportional to the temperature. The result is that the radiation maximum shifts to shorter wavelengths as the temperature increases, as shown in Figure 1 [18]. From this it is concluded that at high temperatures the luminescence intensity of phosphors competes with blackbody radiation.

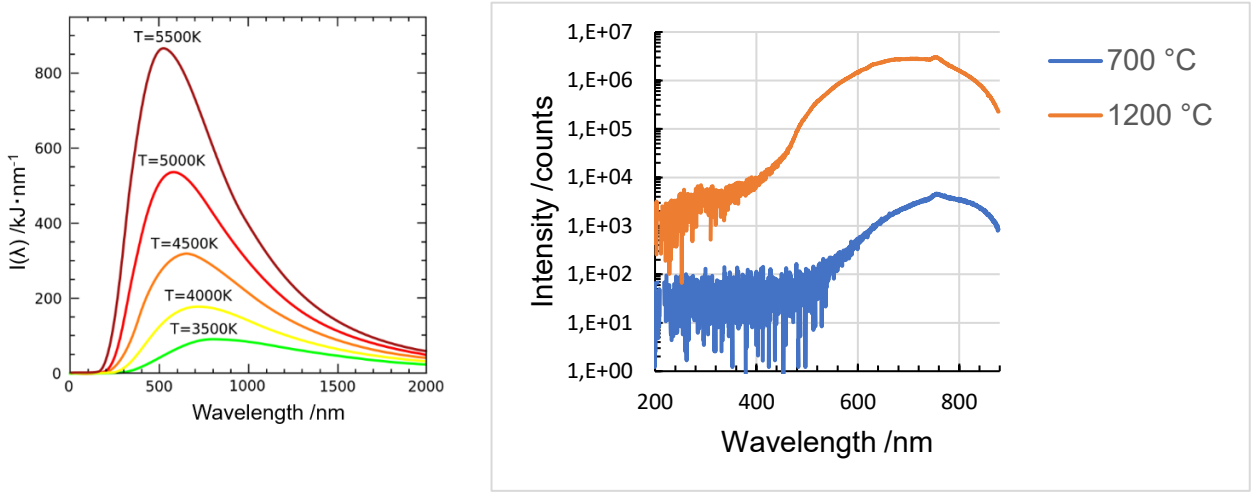

Figure 1: The spectra of blackbody radiation for two temperatures were measured at DLR in Augsburg (right) in a sample heating oven, whereas the measurements for several temperatures (left) were taken from [17] and modified

2.5 Choice of materials

Inorganic binders and luminescent materials were selected for the high temperature TSP project. The choice of phosphors is limited to the search for luminescent materials with a large Stokes shift of at least 100 nm to avoid overlap of the excitation light with the emission spectrum of the phosphor. Due to this and the available equipment at the DLR Göttingen the phosphor should be excitable from 365 nm and emit in the wavelength range 580-670 nm. The

lifetime should be at most 100 µs in the range of sensitivity while providing sufficient intensity. On this basis, europium(II)-doped strontium calcium aluminum silicon nitride ($(Sr_{1-x}Ca_x)AlSiN_3:Eu^{2+}$, SCASN:$Eu^{2+}$), dysprosium-doped yttrium vanadate ($YVO_4:Dy^{3+}$) and europium-doped yttrium phosphate vanadate ($Y(V,P)O_4:Eu^{3+}$) for the temperature range 300 - 800 °C are chosen [18]. Furthermore, europium doped yttrium aluminum garnet ($Y_3Al_5O_{12}:Eu^{3+}$, YAG:Eu^{3+}), dysprosium-doped lutetium aluminate ($Lu_3Al_5O_{12}:Dy^{3+}$, LuAG:Dy^{3+}) and dysprosium doped yttrium aluminum garnet ($Y_3Al_5O_{12}:Dy^{3+}$, YAG:Dy^{3+}) are suitable for a temperature range > 800 °C, since garnets are characterized by their high temperature stability. The temperature lifetime characteristic of some of these examined phosphors can be seen in Figure 2, which was reproduced by using Allison and Gillies data [19].

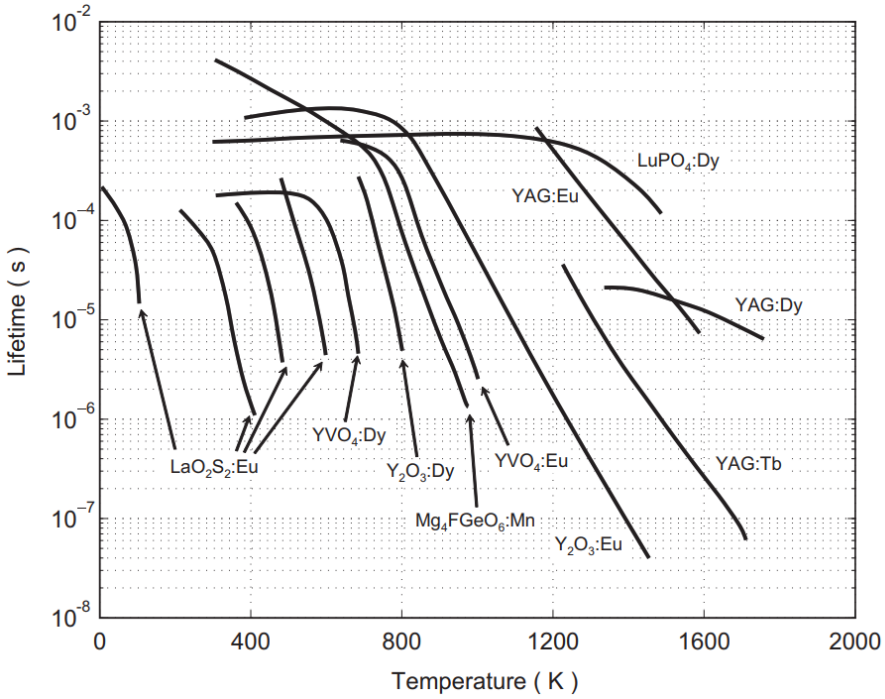

Figure 2: Temperature sensitivity of different phosphor materials [4]

The phosphors $YVO_4:Dy^{3+}$ and YAG:Eu^{3+} were synthesized as a part of this work using the combustion solution method at Münster University of Applied Sciences while LuAG:Dy^{3+} and YAG:Dy^{3+} were synthesized and provided by Prof. Jüstel and his research group. The phosphor $(Sr_{1-x}Ca_x)AlSiN_3:Eu^{2+}$, which was produced by Grirem Advanced Materials, and the phosphor $YVO_4:Eu^{3+}$, which was stabilized with phosphorus and was prepared by Tailorlux GmbH, were also provided by Prof. Jüstel.

To develop a TSP from these phosphors, three different binders were used. One of the three binders selected is Ceramabind 643-1 from Aremco. It has been used in previous work for high temperature TSP at DLR in Göttingen and showed good mechanical properties, especially

regarding adhesion. However, due to its alkaline pH value, it is not used for phosphors containing alkaline or alkaline earth metals to avoid chemical reactions between them. Another binder from the same company is Ceramabind 880, whose properties are promising because of the neutral pH value which allows mixing with phosphors containing alkali or alkaline earth metals. Since the temperature resistance reaches 650 °C, it is used exclusively for $(Sr_{1-x}Ca_x)AlSiN_3:Eu^{2+}$, $YVO_4:Dy^{3+}$ and $Y(V,P)O_4:Eu^{3+}$ [7]. The components of both binders from Aremco are not known. The third binder is the water-alcohol-based ZAP Binder which is manufactured by Zyp Coatings. It consists mainly of aluminum oxide and phosphorus pentoxide [8]. It has been used in previous work for high temperatures [9] and has a maximum use temperature of 1600 °C. Since it has an acidic pH value, it is used, like Ceramabind 643 - 1, exclusively for phosphors that do not contain alkali or alkaline metals.

2.6 Electronic states

The interaction between the orbital and spin moments of electrons results in different microstates that can be assumed for an element with a certain electron configuration. For light elements up to lanthanum, this interaction is described with the help of the Russel-Saunders coupling. In this case, the spins and orbital angular momentum of all electrons are taken into consideration, allowing the total angular momentum *J* to be calculated. For heavy elements, there is a strong coupling between the spins and orbital angular momentum of the individual electron, which is called JJ-coupling and leads to a multiplet splitting of the individual energy levels [20].

Russel-Saunders terms are used to describe the individual energy states, which are composed of the total spin *S*, the total orbital angular momentum *L* and the resulting total angular momentum *J* due to the coupling of *S* and *L*. From these, the term result in the form $^{2S+1}L_J$ [20, 21].

The total spin S is calculated by the sum of the spins of all valence electrons. Each has a value of $s = \pm ½$. The total spin is given with the spin multiplicity 2S+1 [22].

$$S = \sum_{i=1}^{n} s_i \tag{2}$$

The total orbital angular momentum *L* is the sum of the individual orbital angular momentums l, which characterize the shape of the orbital. Consequently, the value of l is assigned to a letter as shown in Table 2. In addition, a spatial orientation can be assigned to the orbital angular momentum with the help of the magnetic quantum number m_l, which can assume

values from +l to -l. The number of m_l values indicates how many states of the given orbital exist [20].

$$L = \sum_{i=1}^{n} l_i \tag{3}$$

Table 2: Assignment of the orbital angular momentum of an orbital shape [20]

L	0	1	2	3	4	5
Label	S	P	D	F	G	H

The total orbital angular momentum J is formed from the coupling of the spin and the orbital angular momentum and takes values between $|L + S|$ and $|L - S|$ [21].

Spectroscopic energy levels result from the electron-electron interaction (*Coulomb* interaction) and the spin-orbit interaction. The ground state is determined as the energetically most favorable state. In order to determine the associated term of the ground state, Hund's rules are used. These state that the ground term must have the maximum value of the spin multiplicity 2S+1. If there are several terms with the maximum spin multiplicity, the term with the greater total orbital angular momentum is the ground state. If the values for the spin multiplicity and for L are the same, the ground state is at the smallest *J* value for a less than half-filled shell and at the largest *J* value for a more than half-filled shell [20].

Referring to Hund's rule, the basic terms are determined for the activators used in this work (see Table 3).

Table 3: Russel-Saunders terms of the ground states of the used activators, taken from [20] and modified

Activator	Electron configuration	Ground term
Eu^{3+}	$[Xe]4f^6$	$^7F_0$
Eu^{2+}	$[Xe]4f^7$	$^8S_{7/2}$
Dy^{3+}	$[Xe]4f^9$	$^6H_{15/2}$

2.7 Luminescence

In a luminescence process, external energy is supplied to a system, which is later emitted as electromagnetic radiation beyond thermal equilibrium. This process is fundamentally different from blackbody radiation or incandescence because luminescence means that no thermal equilibrium exists between electrons and photons. In this case, the system is transferred to an excited state by the absorption of energy. Subsequently, the system relaxes back to the ground

state and electromagnetic radiation is partially emitted. The emitted radiation is mostly in the visible range, but can also be in the ultraviolet or infrared spectral range [23]. In addition to this process, also electron transitions take place that cause non-radiative deactivation. Further details on these mechanisms will be given in chapter 2.9. Luminescence can be classified into different categories depending on its excitation source. While photoluminescence (PL) is excited by photons, electroluminescence uses an electric field, triboluminescence uses mechanical energy, or chemiluminescence uses the energy of a chemical reaction for excitation. Further types of luminescence are listed in [24]. This thesis refers to the photoluminescence.

Luminescent materials are mostly solids. Inorganic luminescence materials comprise a host lattice, which are doped by ions in low concentrations. In most cases, these ions are responsible for the light emission and make up the luminescence center. They are called activators. Absorption occurs through the host lattice material or through the activators. If the absorption of these activators is weak, a second ion can be used, which is called a sensitizer. These exhibit high absorption in the required spectral range and subsequently transfer the excitation energy to the activator. A low concentration of these activators is necessary because a higher doping level can cause concentration quenching. This means that energy transfer of the excitation energy can occur between the ions which is called energy migration, due to the lower dopant spacing from each other. This increases the probability that the energy will find a quenching center, causing a loss of radiation [13, 25].

In the photophysical process of luminescence, apart from the radiative transitions, the non-radiative transitions also take place, as already mentioned in the previous chapter. To understand the whole process, the Jablonski energy level diagram is used (see Figure 3). The thicker lines represent the electronic states while the thinner lines represent the vibrational states of each electronic state. The lowest line depicts the ground state which is denoted by S_0. The upper lines illustrate the singlet and triplet states which are denoted by S_1, S_2 and T_1. The energy of the first singlet state is lower than the energy of the second singlet state. Both singlet states are normally higher in energy than the first triplet state.

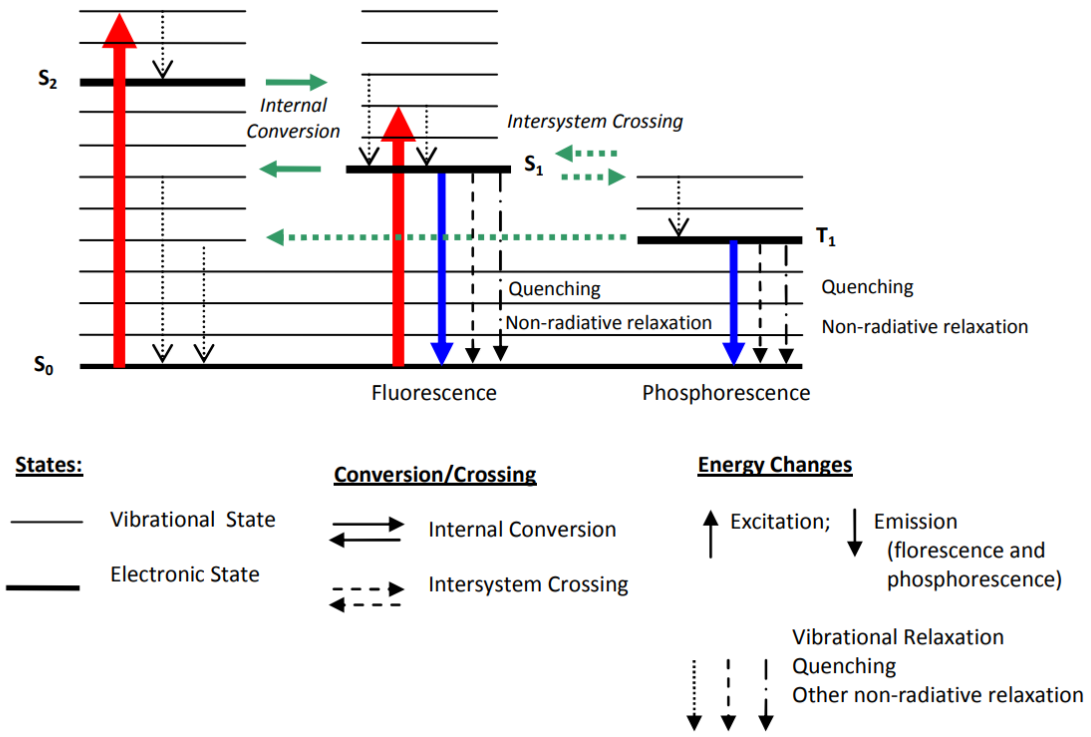

Figure 3: Jablonski energy level diagram [5]

After the absorption of photons, electrons gets excited from the electronic singlet ground state (S_0) to higher vibrational states of the first or second excited electronic singlet state (S_1, S_2) This process can be expressed as $S_0 + h\nu \rightarrow S_1$, while h is the Planck constant ($\approx 6.626 * 10^{-34}$ Js) and ν is the frequency of the excitation light. Since these two states are not stable, the absorbed energy is released in different relaxation mechanisms [3].

The excited electrons within an electronic state can relax from higher vibrational states to lower vibrational states which is called vibrational relaxation (VR). In this process energy is released in form of heat. Through internal conversion (IC), it is possible that excited electrons converse from the lowest vibrational level of one electronic excited state to the highest vibrational level of a lower second electronic excited state, if these two are sufficiently close. A VR can result from this transition. When the excited electrons from the lowest electronic excited singlet state (S1) return to the ground state, the transition is called fluorescence. This process can be depicted as $S_1 \rightarrow S_0 + h\nu_f$. This is a radiative transition, since this transition is not spin forbidden and the two mentioned states have the same spin multiplicity. Accordingly, this results in a fast lifetime τ between 10^{-11} and 11^{-6} s [3]. In addition, it can be noted that the wavelength of this emission is lower in energy than the vibrational relaxation and the associated heat release.

The emission from T_1 to the ground state S_0 is called phosphorescence or afterglow. The non-radiative transition from S_1 to T_1 is called as intersystem crossing (ISC). It leads to an

inversion of the spin of the excited electrons and thus the electrons are oriented in parallel. Therefore, phosphorescence is spin forbidden, since the electrons in the excited triplet state do not have the same spin multiplicity as in the ground state. This results in longer lifetimes, spanning orders of magnitude from milliseconds to minutes. Moreover, the energy difference between the absorbed and emitted photons is bigger than in fluorescence because T_1 is lower in energy than S_1 which leads to a larger Stokes shift [11] . This process can be expressed as $T_1 \rightarrow S_0 + h\nu_p$ [3, 5].

In addition to these radiative and non-radiative transitions, quenching processes also take place, which lead to the deactivation of the excited electronic states and consequently result in non-radiative transitions. These are caused by energy transfer between the excited molecules and the system. Thus, it is possible that concentration quenching occurs (chapter 2.7.1) or oxygen quenching is induced. Oxygen quenching deals with a decrease in emission intensity with increasing oxygen partial pressure. This occurrence is used in pressure sensitive paint (PSP), which will not be considered in detail in this project. Similar to PSP, the emission intensity also decreases with increasing temperature which is called thermal quenching (TQ). TSP is based on this phenomenon and will be discussed in more detail in the next chapter [5].

2.8 Selection rules

Electronic dipole transitions are subject to quantum mechanical selection rules which determine whether a transition is considered forbidden or allowed. If these rules are not followed, the transition is classified as forbidden. The probability of a forbidden transition occurring tends towards 0 [26]. However, since the conditions of the selection rule are not completely taken into consideration, forbidden transitions take place with a smaller probability and intensity compared to allowed transitions [27]. Rules that are essential for this project are the parity, the spin and the conversion of the angular momentum.

According to Laport's rule, an electronic-dipole transition between two energy levels with the same parity is not allowed to occur in a molecule with an inversion symmetrical environment. In these molecules, the parity describes the behavior of an orbital at the inversion center and is called *gerade* (g) if the wave function does not change its sign when mirrored at the inversion center. Otherwise, when the sign changes, it is called *ungerade* (u) parity. Hence, u parity applies to *p* and *f* orbitals while g parity applies to *s* and *d* orbitals. Thus, transitions between $u \rightarrow u$ and $g \rightarrow g$ are not allowed, while $u \rightarrow g$ and $g \rightarrow u$ are allowed. Accordingly, transitions within *f* and *d* orbitals, as well as between *d* and *s* orbitals, are parity forbidden [22, 27].

However, this rule can be weakened so that low intensities are observed. The absence of a center of symmetry onto a certain crystallographic site of a rare earth ion creates a crystal field with uneven components. This allows the formation of mixed orbitals with opposite parity such as 5d with 4f orbitals, so that the 4f orbitals no longer have a purely u character. As a result, the parity violation no longer applies strictly to the 4f-4f transitions. This can also be applied to other electronic-dipole transitions between two energy levels with the same parity. Furthermore, asymmetric stretching and deformation vibrations occur in the inversion symmetrical environment, which can remove the inversion symmetry temporary. This results in coupling of electronic transitions with vibrations which increase the transition probability of forbidden transitions [23, 26].

The spin selection rule states that the multiplicity M is not allowed to change during a transition between two electronic states. Since the multiplicity is 2S+1, it depends on the total spin S. As long as the spin of the electron does not change in an electronic transition, it is a spin-allowed transition. However, this rule can be weakened by spin-orbit coupling, i.e. by interaction between spin momentum and orbital momentum. This interaction is more intense in heavy atoms than in light atoms, which is why spin forbidden transitions are more likely to be observed in lanthanides than in those with a smaller atomic number. Nevertheless, those transitions are less intense than the allowed transitions [22, 23].

A photon carries the angular momentum of h/2π or 1, which is conserved during absorption or emission. The total angular momentum J of a multi electronic system, which is composed of the total spin S and the total orbital angular momentum L, will change by 1 during a transition. However, $\Delta J = 0$ is also possible with the condition that for the magnetic orbital angular momentum quantum number $\Delta m_j \neq 0$ applies. A transition from $J = 0$ to $J = 0$ is forbidden since there is no angular momentum in the ground state that could be transferred [26, 27].

2.9 Thermal quenching

The process of thermal quenching describes the decrease of emission intensity and is caused by the activation energy E_A, which is illustrated in Figure 4 with the help of a configuration coordination diagram. In the diagram, the potential energy is plotted against the distance of the surrounding ligands to the luminescence center. The parabolic curves represent the electronic ground state (G) and the excited state (E) which intersect at one point. These arise with the assumption that the vibrational movements are following a harmonic oscillator. The shift of the parabolas is caused by a change in the equilibrium distance between the center and its chemical environment, which results in a strong electron-phonon coupling and will be

discussed in more detail in the next chapter. The thin horizontal lines represent the vibrational states. At the minimum r_0 the system is in equilibrium and an equilibrium distance in the ground state applies [5, 25].

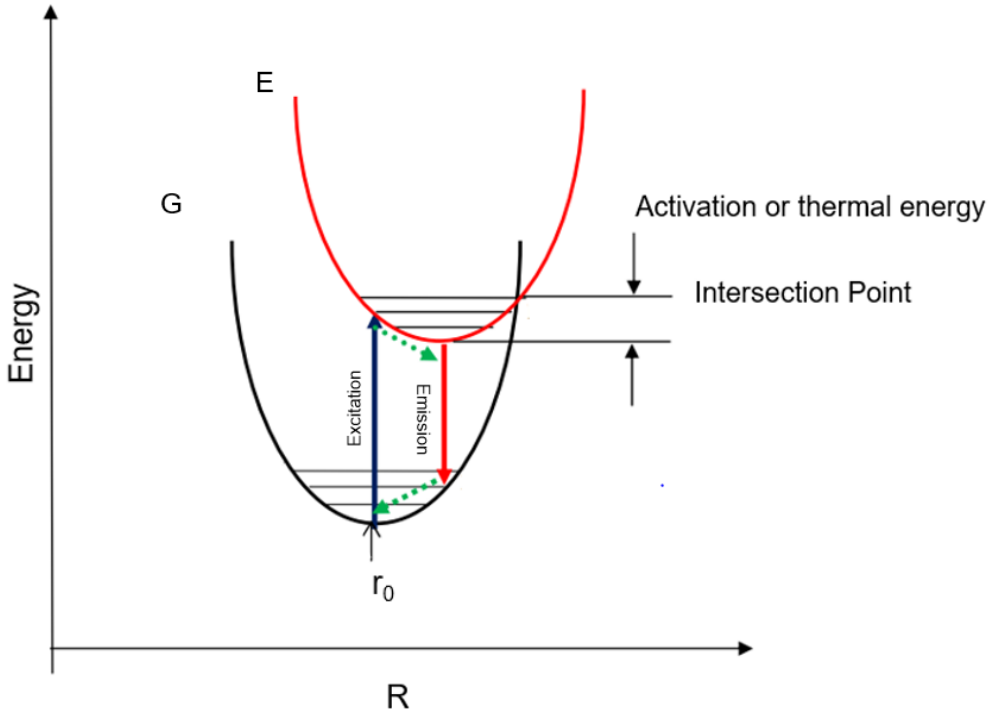

Figure 4: Illustration of thermal quenching using a configuration coordination diagram, taken from [5] and modified

Similar to the Jablonski diagram, the vertical arrows are used to describe absorption and emission processes. This alignment of the arrows is due to the fact that these electronic transitions are faster than the nuclear movement due to the lower mass of the electrons, according to the Franck-Condon principle. Accordingly, vertical transitions result from the nuclear coordinate remaining [27].

After photon absorption, electrons are transferred to an excited vibrational state. A relaxation into the lowest vibrational state of the excited state follows while releasing energy in form of lattice vibrations. From this point, radiative transitions take place to higher vibrational state of the ground state, whereupon the electrons relax back into the ground state equilibrium with the release of heat. At this point, the Stokes shift can be observed since there is an energy difference between absorbed and emitted radiation due to the shift of the parabolas to each other over a value ΔR.

The energy difference between the intersection point and the equilibrium distance of the excited state is called activation energy (E_A). With increasing temperature, the electrons reach

higher excited vibrational states and can exceed this energy barrier. That leads to reaching the intersection point, from where vibrational relaxation occurs and the electrons return radiationless to the ground state with the release of heat. With the help of the Boltzmann relation $E = k * T$ the corresponding temperature of E_A can be determined, which is called the quenching temperature and is abbreviated as $T_{1/2}$. With increasing ΔR, the intersection point gets at a lower energy. Therefore, E_A and $T_{1/2}$ decrease while the Stokes shift increases [5, 25].

Besides vibrational relaxation, photoionization is another cause of thermal quenching (see Figure 5). In this process, the energetic distance between the excited state of the activator and the conduction band is so small that it can be overcome by thermal activation E_A [25]. As a result, the excited electrons in the conduction band can recombine with holes without radiation, so that thermal quenching occurs [23]. It can be concluded from this that the probability of the photoionization process increases as the energy of the excited state increases and decreases with an increasing band gap. For this reason, phosphors with a small band gap are particularly affected, whereby the quenching temperature decreases as the band gap decreases [26].

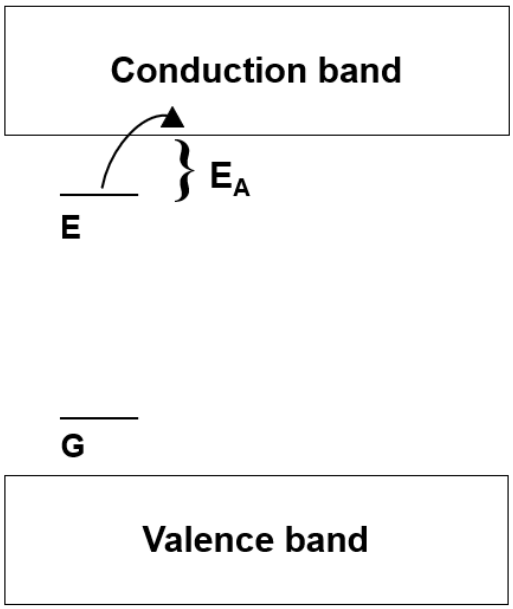

Figure 5: Schematic illustration of photoionization with ground state G and excited state E, taken from [26] and modified

The non-radiative process k_{nr} can be expressed with an Arrhenius equation:

$$k_{nr} = k_{nr0} + k_{nr1} * \exp(-\frac{E_{nr}}{RT}) \quad (4)$$

While knr_0 represents the temperature-independent term and starting point at T = 0, respectively, k_{nr1} describes the rate constant of the temperature dependent non-radiative

processes. E_{nr} represents the activation energy of the non-radiative processes, while R denotes the universal gas constant and the absolute temperature is denoted by T. From this equation it can be concluded that the probability of non-radiative transitions increases with increasing temperature and thus also the luminescence intensity [3].

As the lifetime depends on both rate constants for radiative (k_r) and for non-radiative relaxation (k_{nr}) to the ground state, it is also temperature dependent.

$$\tau = \frac{1}{k_r + k_{nr}} \tag{5}$$

Since the luminescence intensity I(t) is proportional to the number of excited electrons N(t) at time t:

$$N(t) = N_0 * \exp\left(-\frac{k_r + k_{nr}}{\tau}\right) \tag{6}$$

a decrease in luminescence intensity over time is observed with decreasing excited electrons. This decay process can be illustrated with equation (7):

$$I(t) = I_0 * \exp\left(\frac{-t}{\tau}\right) \tag{7}$$

with I_0 being the initial intensity, I the intensity at time t and τ the lifetime [28, 29].

2.10 Electron-phonon coupling

As it was already worked out in the previous chapter, the Stokes shift and the associated shift ΔR of the parabolas to each other determines the strength of the electron-phonon coupling, which can provide information about the emission and absorption since the absorption bandwidth corresponds with ΔR [28]. Figure 6 shows electron-phonon couplings for different ΔR.

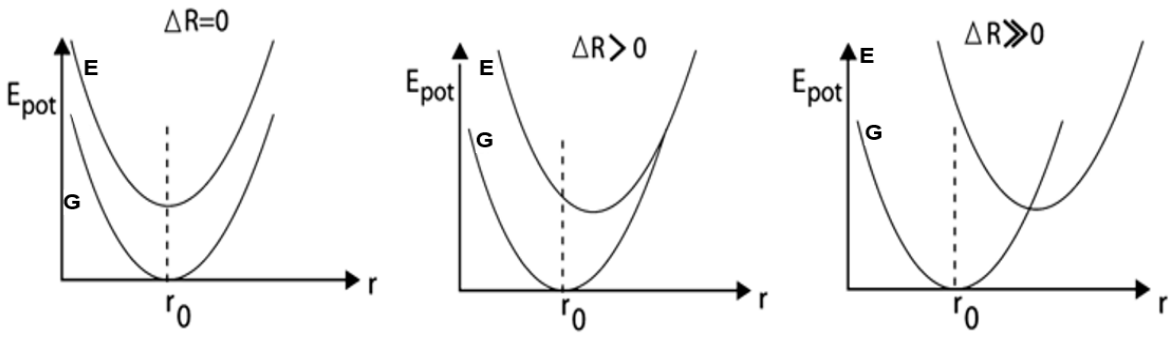

Figure 6: Schematic illustration of different strong electron-phonon couplings in configuration coordination diagrams, taken from [28] and modified

If the shift of the parabolas is ΔR = 0, there is a small Stoke shift as well as a weak electron-phonon coupling. Therefore, the chemical bonding character of the two electronic states remains almost unchanged. This can be observed in 4f → 4f transitions of trivalent rare earth ions such as Eu^{3+} and Dy^{3+}, since the 4f electrons are shielded by the outlying 5s and 5p orbitals which are energetically higher and thus hardly contribute to the chemical bonding. This results in narrow absorption lines and sharp emission bands which are also arised from spin and parity forbidden transitions [23, 28].

Quenching often occurs by multiphonon relaxation or by photoionization [28]. Besides that, depending on the host lattice, there is a low-lying charge transfer state (CTS) that has an intersection with the ground state and the excited state. This allows the transfer of the excited electrons into the charge transfer state at higher temperatures and the returning to the ground state radiationless via the charge transfer state when thermal activation is reached. This enables phosphors with weak electron-phonon coupling to exhibit a large Stokes shift, as shown in Figure 7 [20].

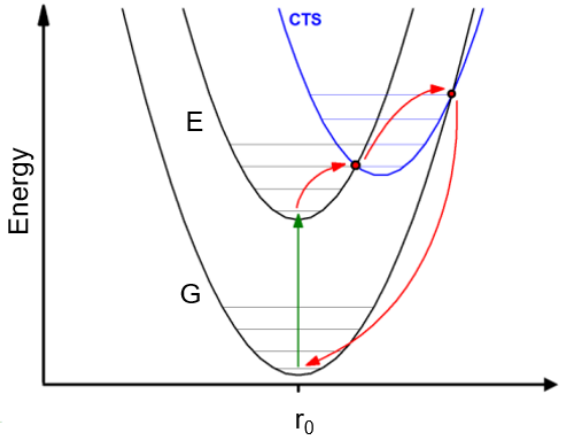

Figure 7: Schematic illustration of thermal quenching by a low-lying CTS, taken from [26] and modified

At ΔR > 0, an intermediate electron-phonon coupling is present, which leads to a moderate stoke shift and thus a change in the chemical bonding between the ground and excited state. This coupling strength is observed in the allowed 4f → 5d transition and thus in rare earth ions such as Eu^{2+} and Ce^{3+}, which leads to broad emission bands. The quenching is mainly triggered by photoionization or tunneling effects [23, 28].

There is strong electron-phonon coupling at ΔR » 0 which is associated with a large Stokes shift. It is observed in molybdates and tungstates, whose luminescence is based on charge transfer processes, as well as in $s^2 \rightarrow s^1p^1$ transitions observed in s^2-ions such as in Sn^{2+} and Pb^{2+} ions. The quenching occurs mainly by tunneling effects, with a low quenching temperature due to the low intersection point [23, 28].

2.11 Activator ions

In this work Eu^{3+}, Eu^{2+} and Dy^{3+} are used as activators which will be described in the next section regarding their luminescence.

2.11.1 Eu^{3+}

Europium belongs to the lanthanide group and occurs in the oxidation states +II and +III. The trivalent cation has an electron configuration of [Xe] $4f^6$. Using Russel-Saunders terminology, the ground state term can be determined as ^7F_J with the quantum numbers of the total angular momentum $J = 0, 1, 2, 3, 4, 5, 6$. Above these there are ^5D_J, ^5L_J and ^5H_J states. By absorbing photons, the electrons relax without radiation from the excited states to the $^5D_0$ level. From here, the emission lines result from the transition to the ^7F_J states, which are based on spin and parity forbidden intraconfiguration transitions and are shown in Table 4 [22, 25].

Table 4: Emission lines of the electronic transitions of Eu^{3+} within 4f-4f intraconfiguration transitions, taken from [22] and modified

Transition	Wavelength / nm
$^5D_0 \rightarrow {}^7F_0$	~ 580
$^5D_0 \rightarrow {}^7F_1$	~ 590 – 600
$^5D_0 \rightarrow {}^7F_2$	~ 609 – 620
$^5D_0 \rightarrow {}^7F_3$	~ 650
$^5D_0 \rightarrow {}^7F_4$	~ 700
$^5D_0 \rightarrow {}^7F_{5\text{-}6}$	Infrared range

The relevant excitation transition for this work is $^7F_0 \rightarrow {}^5L_6$, which is at around 395 nm [27]. Depending on the host lattice and the inversion symmetrical point position, the $^5D_0 \rightarrow {}^7F_1$ and $^5D_0 \rightarrow {}^7F_2$ transitions correspond to the most intense emission lines and are shown in Figure 8. With respect to the crystallographic position, the transition $^5D_0 \rightarrow {}^7F_1$ dominates if the ion is within an inversion symmetric center, since this transition has a magnetic dipole character and is parity allowed. Outside such a center, the parity prohibition is lifted, allowing the stronger electric dipole transitions to predominate and for $J = 0 \rightarrow \Delta J = 2, 4, 6$ the luminescence intensity dominates [22, 30]. Moreover, since the transitions with $\Delta J = 2$ are hypersensitive to the chemical environment, especially regarding symmetry, they appear dominantly in the spectrum by even a small deviation from inversion symmetry and are called the forced electric dipole transition. Thus, the transition $^5D_0 \rightarrow {}^7F_2$ dominates outside of an inversion symmetric center [23].

As already mentioned, the 4f electrons are well shielded, resulting in a small Stokes shift. The O^{2-} - Eu^{3+} charge transfer of oxides as YAG:Eu^{3+} is usually between 200 and 300 nm. By excitation via the charge transfer as described in chapter 2.10, it is possible to use Eu^{3+} as a red emitter.

2.11.2 Eu^{2+}

Europium with the oxidation state +II has the electron configuration [Xe] $4f^7$ and it is stable due to the half-filled 4f shell. According to the Russel-Saunders terminology, the ground state term is $^8S_{7/2}$. The optical transition $4f^65d^1 \rightarrow 4f^7$ ($^8S_{7/2}$) is based on a spin and parity allowed transition, resulting in broad emission bands and short lifetimes (only µs). This transition is shown in Figure 8. The spectral position of the emission band $4f^65d^1 \rightarrow 4f^7$ depends on the centroid shift, the strength of crystal field splitting and on the Stokes shift [25].

The centroid shift describes the decrease in the energy of excited states and is caused by the nephelauxetic effect, which depicts the partial shift of electron density of a central atom to that of the surrounding ligand [28]. As the covalent bond between Eu^{2+} and the ligands increases, the energy difference between the $4f^7$ and $4f^65d^1$ configuration decreases. Furthermore, the crystal field describes the interaction between the ligands, which are considered as negative point charges, and the outer d-electrons. A strong crystal field leads to a large splitting of the d-orbitals, resulting in a lower energy position of the lowest energy level of the $4f^65d^1$ configuration. Thus, depending on the host lattice, the emission lines can extend from the UV range to the red part of the optical spectrum [25].

2.11.3 Dy^{3+}

As europium, dysprosium belongs to the lanthanide group. It occurs in the oxidation state +III with the corresponding electron configuration [Xe] $4f^9$. The luminescence is based on spin and parity forbidden intraconfiguration transitions. Due to the shielding of the 4f electrons as in Eu^{3+}, a weak electron-phonon coupling is present, which results with the forbidden transitions in a low absorption cross-section and sharp emission lines. The excitation occurs from the ground state with the Russel-Saunders term $^6H_{15/2}$ to the higher energy levels of the $4f^9$ configuration, after which the excited electrons relax in the energy levels $^4I_{15/2}$ and $^4F_{9/2}$ [23, 29].

In this work, the relevant excitation transition is $^6H_{15/2} \rightarrow {}^4I_{11/2}$, which lies at around 365 nm. Depending on the host lattice and the inversion symmetrical point position, the most intense emission lines are at 450 nm – 460 nm ($^4I_{15/2} \rightarrow {}^6H_{15/2}$), 470 nm – 500 nm ($^4F_{9/2} \rightarrow {}^6H_{15/2}$) and 570 nm – 600 nm ($^4F_{9/2} \rightarrow {}^6H_{13/2}$). . The transition $^4F_{9/2} \rightarrow {}^6H_{13/2}$ with $\Delta J = 2$ is hypersensitive. Further transitions are listed in Table 5 while the most intense transitions are shown in Figure 8 [23, 29].

Table 5: Emission lines of the electronic transitions of Dy^{3+} within 4f-4f intraconfigurational transitions, taken from [22] and modified

Transition	Wavelength /nm
$^4I_{15/2} \rightarrow {}^6H_{15/2}$	~ 450 – 460
$^4F_{9/2} \rightarrow {}^6H_{15/2}$	~ 470 – 500
$^4F_{9/2} \rightarrow {}^6H_{13/2}$	~ 570 – 600
$^4F_{9/2} \rightarrow {}^6H_{11/2}$	~ 600 – 675
$^4F_{9/2} \rightarrow {}^6H_{13/2}$	~ 700 – 720
$^4I_{15/2} \rightarrow {}^6H_{9/2}$	~ 750 – 770

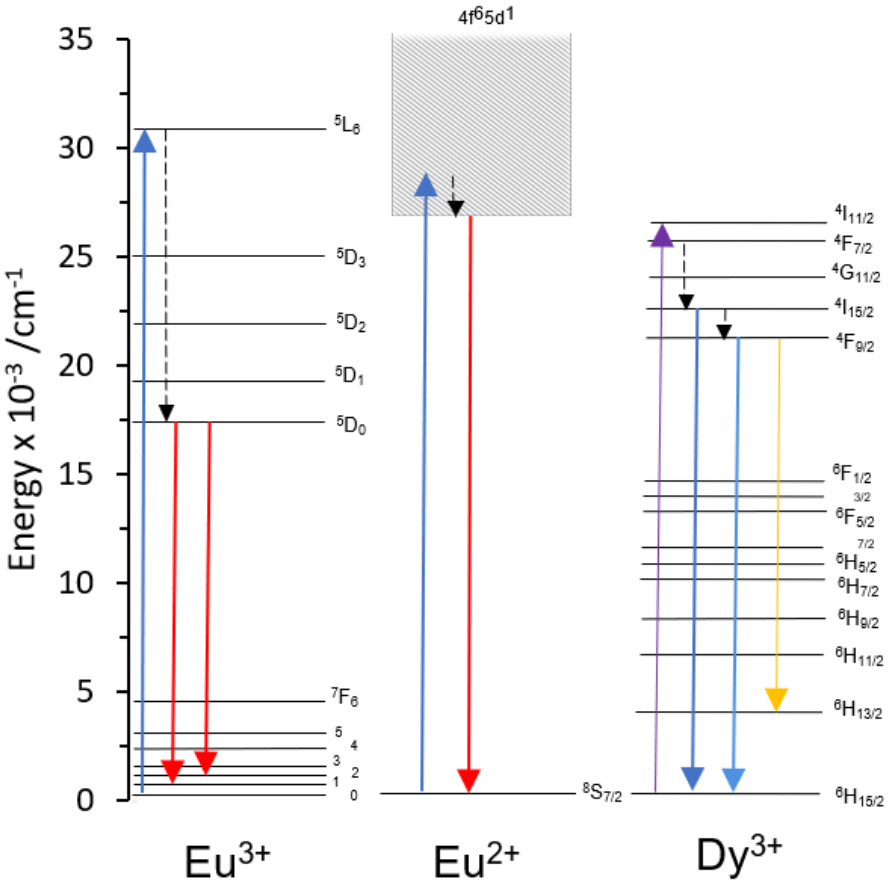

Figure 8: Illustration of relevant absorption and emission transitions of Eu^{3+}, Eu^{2+} and Dy^{3+} for this work, taken from [25, 26, 29] and modified

3 Measurement Techniques

To qualify the phosphors, spectroscopic investigations are carried out as well as the determination of the phase purity (chapter 3.1). After verifying the suitability of these phosphors, the prepared paints must be first calibrated. If the paint fulfils the criteria listed in chapter 1, these reference data are needed for further experiments e.g. for tests in the wind tunnel. The intensity method, lifetime method and mechanical tests are used for calibration and will be described in chapter 3.2.

3.1 Characterization methods of phosphors

3.1.1 X-ray powder diffraction

X-ray powder diffraction (XRD) is used to perform phase purity and crystallinity examinations by determining a match with a reference XRD. The measurements are carried out using the

Miniflex II instrument from *Rigaku*, operating in Bragg-Brentano geometry and with a *Toshiba Analix A 21* x-ray tube at 30 kV and 15 mA. The anode material is copper. A Ni filter is used to remove higher energy radiation from the X-ray tube. [26] In addition, as an X-ray detector a NaI:Tl scintillation counter is installed. The powder samples are mounted on a glass sample holder and measured in the region of 2θ between 20° and 80° in 0.02° steps with an integration time of 1 s. The reference diffractograms of the measured phosphors are taken from the database *Pearson's Crystal Data*.

3.1.2 Particle size distribution

The particle size of the phosphors is determined by using the *LA-950V2* from *Horiba*, which is equipped with a red laser beam (650 nm) and a blue LED (405 nm). From the light scattering behavior of these two, the particle size distribution of the phosphor samples is determined by the instrument software. The phosphor sample is placed in water and is suspended by using ultrasound. The ultrasound is set to level 5 for 4 minutes, the circulation speed to level 7 and the stirring speed to level 3. A refractive index of 1.333 is entered for water. The refractive indices of the phosphors are listed in Table 6.

Table 6: Refractive indices of the phosphors

Phosphor	Refractive index at λ = 405 nm	Refractive index at λ = 650 nm
$(Sr_{1-x}Ca_x)AlSiN_3:Eu^{2+}$	1.930	1.930
$YVO_4:Dy^{3+}$	1.972	2.021
$Y(V,P)O_4:Eu^{3+}$	1.972	2.021
$YAG:Eu^{3+}$	1.833	1.833
$YAG:Dy^{3+}$	1.833	1.833
$LuAG:Dy^{3+}$	1.842	1.842

3.1.3 Excitation and emission

Excitation (Ex) and emission (Em) spectra were measured by the *FLS 920* spectrometer from *Edinburgh*. As the excitation source a 450 W xenon discharge lamp operated at 25 A is used. The spectrometer is equipped with a Peltier-cooled single-photon counting photomultiplier *R2658P* from *Hamatsu*, two *TMS300* monochromators from *Bentham Instruments* and mirror optics. An integrated reference detector is used to correct the excitation. Correction of the emission spectra is performed by using a tungsten incandescent lamp certified by the *NPL* (national Physics Laboratory, UK) [31]. The measurement parameters of the excitation and

emission spectroscopies are shown in Table 7 and 8, which are also used for the thermal quenching measurements in chapter 3.1.4.

Table 7: Measurement parameters of the excitation spectra

Parameter	$SCASN:Eu^{2+}$	$YVO_4:Dy^{3+}$	$Y(V,P)O_4:Eu^{3+}$	$YAG:Eu^{3+}$	$YAG:Dy^{3+}$, $LuAG:Dy^{3+}$
Emission wavelength /nm	618	574	619,5	590,5	582
Measuring range /nm	200 - 600	200 - 550	200 - 550	200 - 550	200 - 550
Filter /nm	590	530	550	550	550
Band width (Ex) /nm	1	1	0,5	1	1
Band width (Em) /nm	0.7	0.7	0.5	1	3
Step /nm	1	1	1	1	1
Dwell time /s	0.5	0.5	0.5	0.5	0.5

Table 8: Measurement parameters of the emission spectra

Parameter	$SCASN:Eu^{2+}$	$YVO_4:Dy^{3+}$	$Y(V,P)O_4:Eu^{3+}$	$YAG:Eu^{3+}$	$YAG:Dy^{3+}$, $LuAG:Dy^{3+}$
Excitation wavelength /nm	450	366,5	395,5	394	366
Measuring range /nm	450 - 800	450 - 800	550 - 750	550 - 800	450 - 800
Filter /nm	550	420	550	550	420
Band width (Ex) /nm	0.7	1	0.5	1	3
Band width (Em) /nm	1	1	0,5	1	1
Step /nm	1	1	1	1	1
Dwell time /s	0.5	0.5	0.5	0.5	0.5

3.1.4 Thermal quenching

The temperature dependent emission and excitation spectra of the phosphors are measured in the range between 25 °C and 450 °C in 50 °C steps. The spectrometer is used as described in in chapter 3.1.3. The *EUC 442* universal controller from *Enda* is used as the temperature controller and the *PPS-11815* is used for the power supply. The sample holder is designed by the workgroup itself and consists of a corundum ceramic manufactured heater, which is located underneath the cavity for the sample. Furthermore, the heater consists of a *CHROM60* filament from *ISA* with a diameter of 0.5 mm [32]. The phosphor samples are dissolved in ethanol and

applied to the sample holder using a pipette, leaving a flat solid sample after evaporation of ethanol. The housing of the sample holder is actively cooled with water using a submersible pump.

3.1.5 Reflection

Reflectance spectra were performed on the *Edinburgh FS 920* spectrometer equipped with a polytetrafluoroethylene coated integrating sphere, a 450 W xenon discharge lamp, two *TMS300* monochromators from *Bentham Instruments* and a *R2658P* Peltier-cooled single-photon counting photomultiplier from *Hamamatsu*. $BaSO_4$ (Sigma Aldrich 99.99%), which has high reflectivity, is used as the white standard. Two individual measurements are made, which are merged after the measurements. For the measurement between 480 and 800 nm a 455 nm filter is used because of to the 2nd order of the excitation wavelength. A step size of 1 nm is chosen for recording the spectra. Synchronous scan is used, so that the excitation and emission monochromators are scanned simultaneously along the wavelengths. Furthermore, the excitation bandwidth is set to 10 nm and the emission bandwidth is set to 0,06 nm.

3.1.6 External quantum efficiency

The external quantum efficiency (EQE) is measured using the equipment as from the reflection section. This value represents the efficiency of a phosphor and gives the ratio between the number of emitted photons ($\mathrm{N_{em}}$) and the absorbed photons ($\mathrm{N_{abs}}$) of the excitation wavelength of a phosphor [33].

$$EQE = \frac{N_{em}}{N_{abs}} \tag{8}$$

3.2 TSP measurements

3.2.1 Intensity-based method

As it was already mentioned in chapter 2.2, the luminescence intensity of the TSP decreases with increasing temperature. To capture this, the intensity-based method is used. Here, the intensities are measured at different temperatures using a spectrometer to assess the sensitivity of the TSP.

3.2.1.1 Measurement setup

For this measurement the spectrometer *FP-6500* from *JASCO* is used. It is equipped with a DC-powered 150 W Xenon lamp, concave holographic grating monochromators and two photomultiplier tubes. The second detector is used for observation and compensation of intensity variations of the light source [datasheet]. The spectrometer is connected to a temperature controller and a computer, which can be used to set parameters such as bandwidth, excitation and emission wavelength for the measurement. The temperature controller is connected to an air-locked latched calibration chamber, which is sealed with a quartz glass plate to allow optical access. The sample is located in this chamber. Accordingly, the setup is designed so that the fiber optic cables for exciting and recording the emission spectra are located above the chamber (see Figure 9). In addition, a Peltier element is located below the sample in the calibration chamber, which can be heated and cooled using the connected temperature controller. This makes it possible to measure the sample on the Peltier element at different temperatures. In addition, a higher cooling rate can be achieved with the use of nitrogen to cool down the sample in the calibration chamber. For this purpose, a nitrogen bottle and a pressure regulator are connected to the calibration chamber. Furthermore, a vacuum pump is connected, which allows a controlled supply of nitrogen. Above the calibration chamber there is a tube pointing at the quartz glass and connected to a pressurized air bottle. This pressurized air flow is intended to cool the glass, as it can fog up at high temperatures and lead to non-reproducible measurement results.

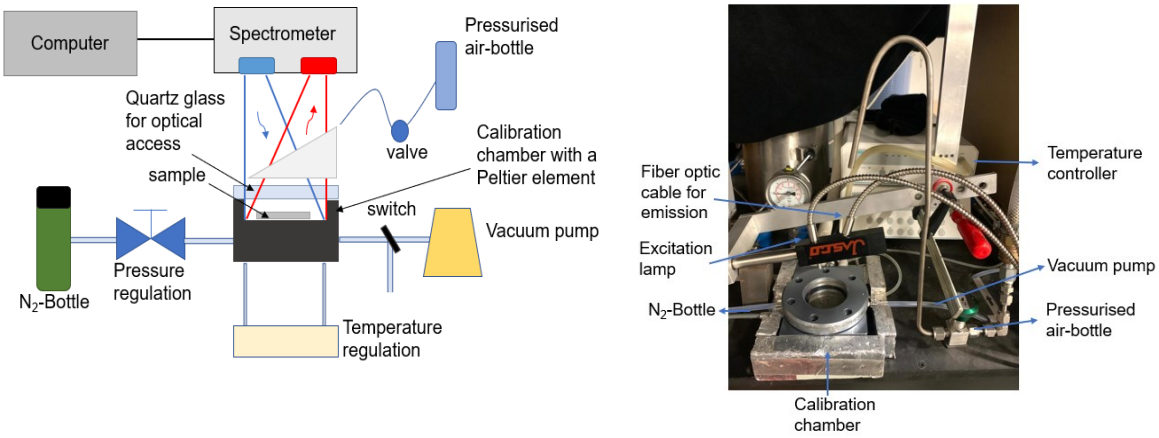

Figure 9: Schematic measurement set up (left) and section of actual measurement setup (right) of the intensity-based method

All samples are measured at a *High* sensitivity. The measurement of the spectra are taken at an excitation and emission band width of 3 nm, except for $YVO_4:Dy^{3+}$, $(Sr_{1-x}Ca_x)AlSiN_3:Eu^{2+}$

and $Y(V,P)O_4:Eu^{3+}$. For these, 10 nm was selected for the excitation bandwidth due to the broad excitation band of the phosphors (see chapter 4.4).

Depending on the luminescence properties of the phosphors all measurements are taken at an emission band width of 3 nm and at an excitation band width of 3 or 10 nm. The measured spectra are compared with a reference TSP, which is measured with the same settings and can already be used in wind tunnels due to its suitable properties and high luminescence. This reference TSP is *OV322*, which consists of an europium 1,3-diketone complex embedded in a polyurethane polymer [34]. For this work the sample OV322-2 from 25.01.2022 is used for measurement.

3.2.1.2 Data analysis

Using the measured excitation wavelengths, the emission spectra at different temperatures are measured and compared. In addition, the sensitivity T_{sens} can be calculated with the equations (9) and (10) [3].

$$IR_{\pm} = \frac{I_{ref}}{I(P,T_{ref}\pm\Delta T)} \tag{9}$$

$$T_{sens}(P) = \frac{(IR_{+} - IR_{-})*100}{\frac{(IR_{+} + IR_{-})}{2}*(2*\Delta T)} \tag{10}$$

To plot the sensitivity, the mean values of the measured intensities in a certain wavelength range are plotted over temperature. From the obtained trend line and the resulting equation, the mean intensity values for the entire measured temperature range with ΔT= 10 °C are calculated. Using these data and the equations from (9) and (10), the sensitivity values can be visualized as graphs and the change in sensitivity can be observed for larger temperature ranges.

3.2.2 Lifetime-based method

Similar to the intensity-based method, the lifetime-based method can be used to measure the temperature via the lifetime, as the lifetime values decrease with increasing temperature due to thermal quenching. This method is based on the observation that the luminescence intensity decreases exponentially with time which can be illustrated with a decay curve, according to equation (7). The pulse method is used, which enables the measurement of time-resolved intensities.

3.2.2.1 Measurement setup

The sample is placed in a heating chamber, which is sealed with a quartz glass plate to allow optical access and is connected to a computer to regulate the temperature, making it possible to measure between 30 and 59 °C (see Figure 10). The sample is excited by a pulsed LED, which is triggered by a phase locked TTL signal from a frequency generator (FG). At the same time, the FG outputs a further signal to trigger the oscillator. The signal from the LED is picked up by a photodiode and the resulting luminescence intensity is detected by a photomultiplier tube (PMT). These signals are visualized by the oscilloscope. The LEDs are set to pulse at rate of 1 kHz and 32 images are recorded, each with a pulse width of 100 µs.

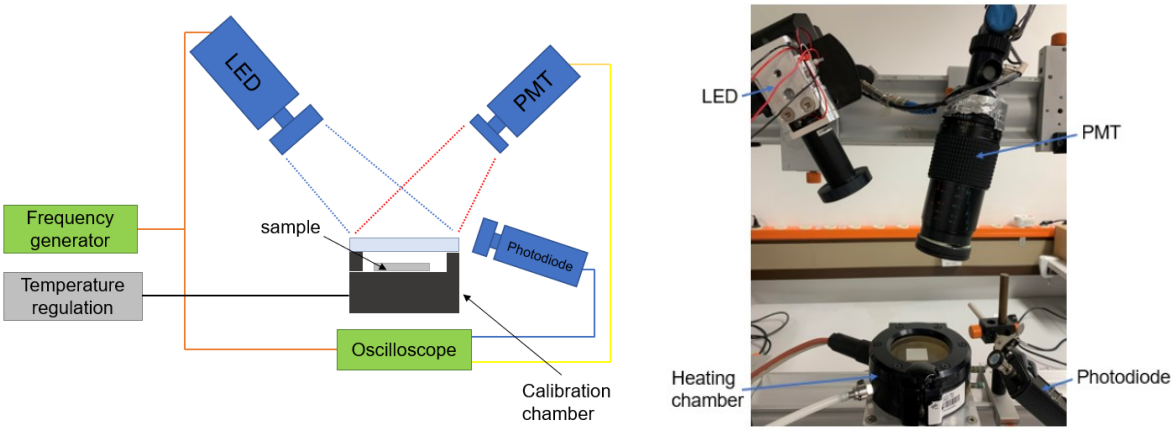

Figure 10: Schematic measurement set up (left) and section of actual measurement setup (right) of the lifetime-based method

3.2.2.2 Data analysis

The luminescence intensities of the 32 recorded images are averaged, normalized to 1 and logarithmically plotted against time. Using a single- or multi-exponential function to fit the decay curve, the lifetime can be determined, which has dropped to 1/e of the initial intensity after switching off the excitation source:

$$I(t) = A_0 + B_1 * exp\left(\frac{-t}{\tau_1}\right) + B_2 * exp\left(\frac{-t}{\tau_2}\right) + \ldots + B_n * exp\left(\frac{-t}{\tau_n}\right) \quad (11)$$

where A_0 is the background intensity and B_n are proportionality parameters [26, 28]. A deviation from a simple mono-exponential decay as suggested by equation (7) can be caused by different crystallographic sites of the activator, by quenching processes or by energy transfer to defects [22].

3.2.3 Mechanical tests

In addition to lifetime and intensity measurements, mechanical tests are also performed. Among these, the surface roughness of the coatings is measured, since low roughness is a requirement for successful TSP for high Mach and Reynolds numbers. This requirement prevents the instability of vortex crossflows at the boundary layer [35].

For the measurement of the roughness the Perthometer *S2* from *Mahr* is used. It is equipped with a diamond at the top of a probe arm, which scans the surface at a constant speed. With this method it is possible to analyze the roughness profile (R-profile), which is standardized according to DIN EN ISO 4287. For this project the parameter R_z is relevant because it gives information about the mean roughness depth. This value is determined by the arithmetic mean value of single roughness depths within the evaluation length. As it was already mentioned in chapter 1, a R_z-value between 1 and 10 µm is desirable. A further description of related parameters to the R-profile can be found in [36] .
If the TSP coating has too high a roughness value, the surface needs to be mechanically workable. In this case, the surface is sanded with 1000 grit sandpaper and subjected to another roughness measurement so that the values before and after grinding can be compared. This clarifies whether an improvement in roughness is possible. The *9500* measuring device from *Automation Dr. Nix* is used to record the layer thickness. Here, the minimum of the layer thickness is desired, since the heat transport of the ambient temperature through the coating can occur faster and fast flow changes can be better resolved with the help of the TSP. However, the thinner the coating, the lower the emission intensity. For this reason, better cameras or more powerful excitation sources are required to detect the intensities [37]. Furthermore, the wettability of the TSP is also investigated by sticking an adhesive tape on the sample and pulling it off. Good adhesion is especially important in hypersonic conditions, as it is possible that the TSP will not adhere at high Mach numbers.
For a closer look at microcracks, this can be additionally examined with the *VHX-2000* microscope from *Keyence*.
The thickness layer influences the response time of TSP. Therefore, it is measured with the coating thickness gauge *9500* from *Automation Dr. Nix.*

4 Experimental

4.1 Synthesis

The phosphor powders are prepared by solution combustion synthesis (SCS). The synthesis is schematic illustrated in Figure 11. Metal oxides and nitrides serve as reactants. While the metal nitrides are dissolved in a minimum amount of distilled water, the metal oxides are dissolved in boiling nitric acid to convert the oxides to nitrides. The solutions are then mixed. Tris(hydroxymethyl)aminomethane (TRIS) is added to the aqueous solution in a 2:1 molar ratio (TRIS:cations) to act as a fuel. The water is evaporated at 90 °C before nitroso gases evolve. A viscous gel is formed, which is burned at a higher temperature. When this exothermic reaction occurs, a black fluffy powder is formed. It is placed overnight for 16 h in a muffle oven at 150 °C. The next day it is crushed in an agate mortar and placed in porcelain crucibles. The crucibles are pre-calcined in air to remove organic residues. After the pre-calcination step, a white mass is formed. To this 2 wt.% flux is added to improve the crystallization process and luminescence properties. After being mortared, it is calcinated in air in a corundum crucible.

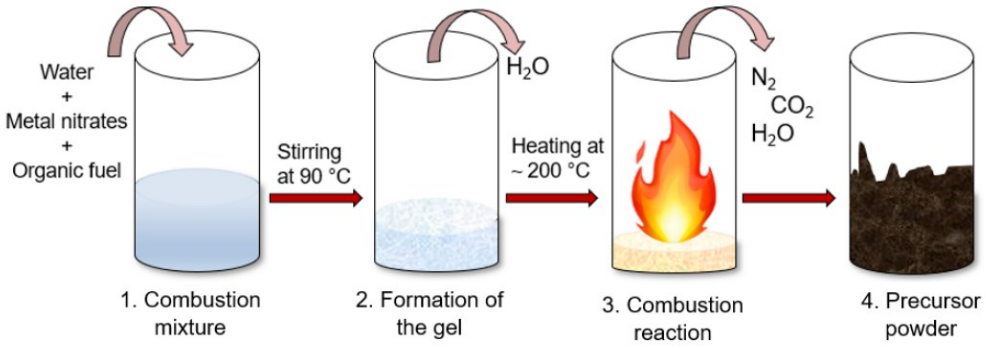

Figure 11: Schematic illustration of the SCS procedure

YAG:Eu^{3+}

Y_2O_3, $Al(NO_3)_3 \cdot 9H_2O$, Eu_2O_3 and TRIS are weighed in stoichiometric amounts for a twofold preparation, each with a preparation of 15 mmol (see appendix, Table 18). After the exothermic reaction, the black powder is dried overnight at 150 °C. The next day, it is pulverized in an agate mortar and pre-calcined at 1000 °C for 2 hours in a porcelain crucible in a chamber oven. The resulting white mass is mortared with 2 wt.% BaF_2 as flux. Then it is transferred to a corundum crucible and calcined at 1600 °C for 3 hours with a heating/cooling rate of 200 °C per hour. A total of 16.5 g of YAG:Eu^{3+}(2%) is synthesized.

$YVO_4:Dy^{3+}$

Y_2O_3, NH_4VO_3, Dy_2O_3, and TRIS are weighed in stoichiometric amounts for one batch of 35 mmol and two batches of 15 mmol (see appendix, Table 18). After the exothermic reaction, the black powder is dried overnight at 150 °C. It is pulverized in an agate mortar and pre-calcined at 1000 °C for two hours in a porcelain crucible in a chamber oven. The resulting white mass is mortared with 2 wt.-% Na_2CO_3 as a flux. Then it is transferred to a corundum crucible and calcined at 1100 °C for 3 hours with a heating/cooling rate of 200 °C per hour in air. The phosphor is calcinated twice to improve the crystallinity. A total of 12.8 g of $YVO_4:Dy^{3+}$(2%) is synthesized.

4.2 X-ray powder diffraction

To determine the crystallinity of the synthesized phosphors, the powder X-ray diffractograms are examined, apart from the selected commercially phosphors.

Figure 12 shows the obtained diffractograms of the garnets YAG:Dy^{3+} and YAG:Eu^{3+} as well as of LuAG:Dy^{3+}, which occupies yttrium sites with Lu^{3+}, and the corresponding reflections of the reference diffractograms from the PCD database. The garnets crystallize in the cubic crystal system with the space group Ia3d [20]. All measured reflections agree with the reflections from the reference diffractograms and show no extraneous reflections. Thus, pure crystalline powder phosphors are obtained.

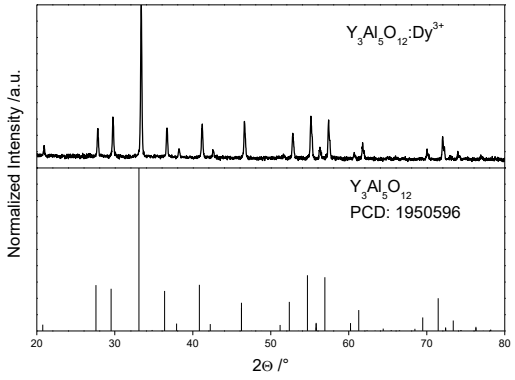

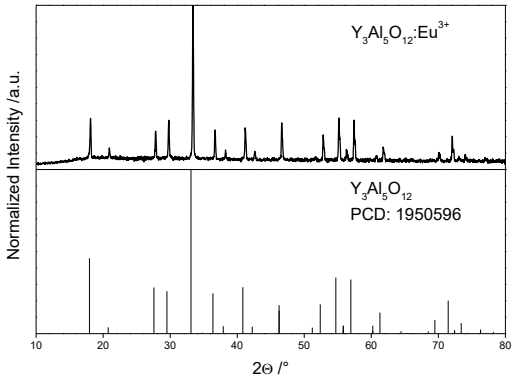

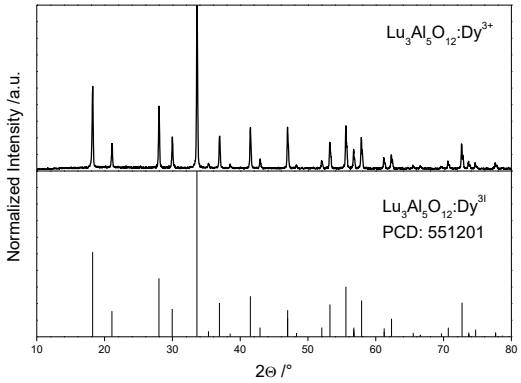

Figure 12: XRD patterns of YAG:Eu^{3+}, YAG:Dy^{3+} and LuAG:Dy^{3+} and the corresponding reference diffractograms from the PCD database

$YVO_4:Dy^{3+}$ was calcined a second time in a chamber furnace at 1100 °C after the XRD patterns showed a strong signal to noise ratio. The result of the second calcination process is given in Figure 13. Compared to the reference diffractogram, it still shows a strong signal-to-noise ratio, which indicates an incomplete crystallization. However, the reflections of the prepared $YVO_4:Dy^{3+}$ powder sample correspond to those of the reference diffractogram from the PCD database. YVO:Dy^{3+} crystallizes in the tetragonal crystal system with the space group I41 [38].

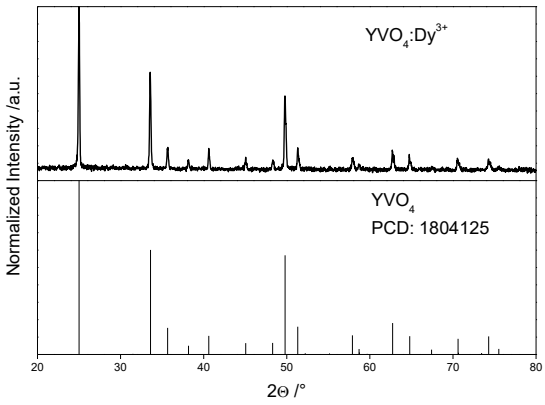

Figure 13: XRD pattern of $YVO_4:Dy^{3+}$and the corresponding reference diffractogram from the PCD database

4.3 Particle size ditribution

The particle size of the phosphors has an influence on the spectroscopy properties as well as a particular influence on the adhesion of the TSP, which is why the aim is to achieve the smallest possible particle size. This can be accomplished by nanoscale reactants, sufficient mortaring and by grinding the phosphors in a ball mill. The median value (d_{50} **–** value) of the particle sizes are given in Table 9 and were taken from the measured particle size distributions (see appendix, Figure 40). The values are > 5 µm and are not ground for the first attempts (see chapter 4.6).

Table 9: measured d_{50} - values of the phosphors

Phosphor	d_{50} – value /µm
$(Sr_{1-x}Ca_x)AlSiN_3:Eu^{2+}$	14.20
$YVO_4:Dy^{3+}$	22.69
$Y(V,P)O_4:Eu^{3+}$	5.86
$YAG:Eu^{3+}$	18.76
$YAG:Dy^{3+}$	21.21
$LuAG:Dy^{3+}$	13.0

4.4 Photoluminescence spectroscopy

After the phosphors have been verified for their phase purity and crystallinity, they are spectroscopically examined by quantum efficiency, excitation and emission and reflection measurements at room temperature.

$(Sr_{1-x}Ca_x)AlSiN_3:Eu^{2+}$

In the excitation spectrum of $(Sr_{1-x}Ca_x)AlSiN_3:Eu^{2+}$ (see Figure 14), the electric-dipole transition [Xe] $4f^7 \rightarrow$ [Xe] $4f^6 5d^1$ is shown with an excitation maxima at 450 nm. This transition is parity and spin allowed, which results in short lifetimes in the µs range. Due to the excitation with blue light and presumably due to a strong nephelauxetic effect and a strong crystal field splitting of the 5d levels, red luminescence occurs, so that $\Delta R \neq 0$ applies. The emission spectrum exhibits a broad emission band ranging from 550 nm to 750 nm and peaking at 618 nm (see Figure 14). This emission corresponds from relaxation of the excited [Xe] $4f^6 5d^1$ state to the [Xe]$4f^7$ ground state of Eu^{2+}.

The reflection spectrum (see Figure 15) was measured by a member of Prof. Jüstel's research group and shows a broad absorption band between 250 nm and 625 nm due to the allowed

transition of Eu^{2+}. Based on the turning point of the band edge at about 575 nm, an orange body color of the phosphor results. The calculated quantum efficiency is 54 %, which is lower than the literature values for $CaAlSiN_3:Eu^{3+}$ between 80 % and 91 % [33]. Since the ratio between Sr^{2+} and Ca^{2+} as well as the Eu^{3+} concentration is not known, these deviations may occur.

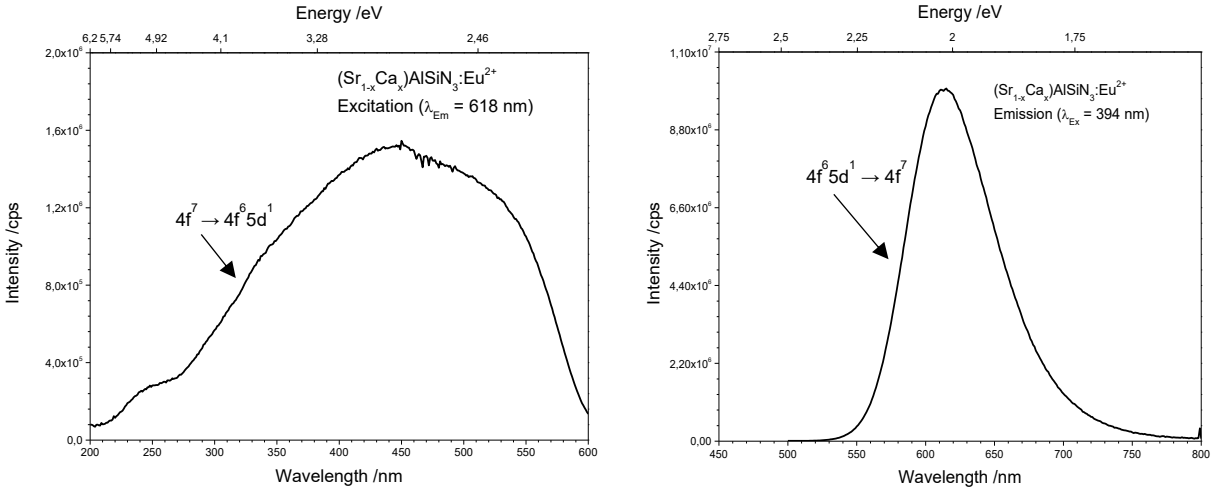

Figure 14: Excitation (left) and emission spectra (right) of $(Sr_{1-x}Ca_x)AlSiN_3:Eu^{2+}$

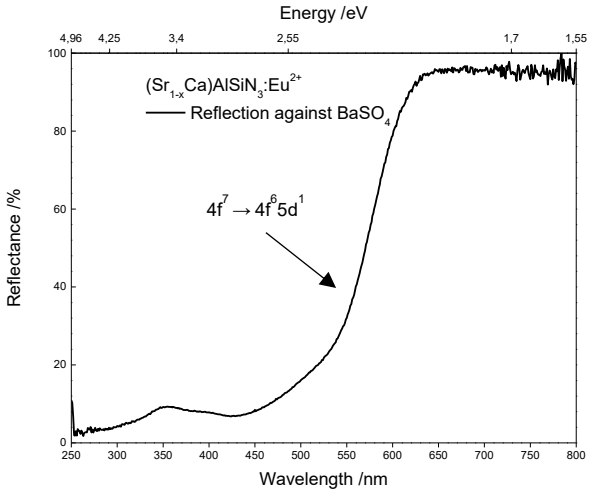

Figure 15: Reflection spectrum of $(Sr_{1-x}Ca_x)AlSiN_3:Eu^{2+}$

$YVO_4:Dy^{3+}$

The excitation spectrum of $YVO_4:Dy^{3+}$ consists of a broad intense band and several narrow lines (see Figure 16). The broad band is observable in the ultraviolet region between 200 nm and 350 nm, which is attributed to the charge transfer of the oxygen ligands to the central

vanadium atom in the VO_4^{3-} group. The shoulder at 260 nm could be an indication that this is an overlap with the Dy^{3+} - O^{2-} charge transfer. In the near ultraviolet and visible range, the narrow peaks are attributed to the intra-configurational 4f - 4f transitions of Dy^{3+}, so that $\Delta R = 0$ applies. The transition $^6H_{15/2} \rightarrow {}^4I_{11/2}$ is located at 365 nm and is used as the excitation wavelength for this work, as it fulfils the requirements for a TSP (see chapter 1). Since the transition is parity and spin forbidden, it results in long lifetimes in the ms range and weak emission lines. The emission lines are observed for the transitions $^4F_{9/2} \rightarrow {}^6H_{15/2}$ (480 nm), $^4F_{9/2} \rightarrow {}^6H_{13/2}$ (574 nm) and $^4F_{9/2} \rightarrow {}^6H_{11/2}$ (655 nm) and $^4F_{9/2} \rightarrow {}^6H_{9/2}$ (755 nm) (see Figure 16). The second mentioned transition is hypersensitive and shows the most intense emission line, which indicates that there is no complete inversion symmetrical environment. As a result, the parity selection rule can be weakened and the emission line is more intense.

The reflection spectrum in Figure 17 shows a broad absorption band in the ultraviolet region, which is caused by the V^{5+} - O^{2-} ligand to metal charge transfer of VO_4^{3-}. This band overlaps with another broad band that extends from the blue range over the entire visible electromagnetic spectrum and is not identifiable. The unidentifiable band and the low reflectance over the entire visible spectral range could indicate a high defect density. This could be the reason for the low quantum efficiency of 1 %, as the probability of energy transfer to a defect and a following radiationless release of the energy is high at a high defect density. Since the broad bands absorbs mostly in the UV and blue range, there is a slightly yellow body color. Furthermore, narrow absorption bands are observed at 365 nm and 760 nm which correspond to the $^6H_{15/2} \rightarrow {}^4I_{11/2}$ and $^6H_{15/2} \rightarrow {}^6F_{3/2}$ transitions [26, 39].

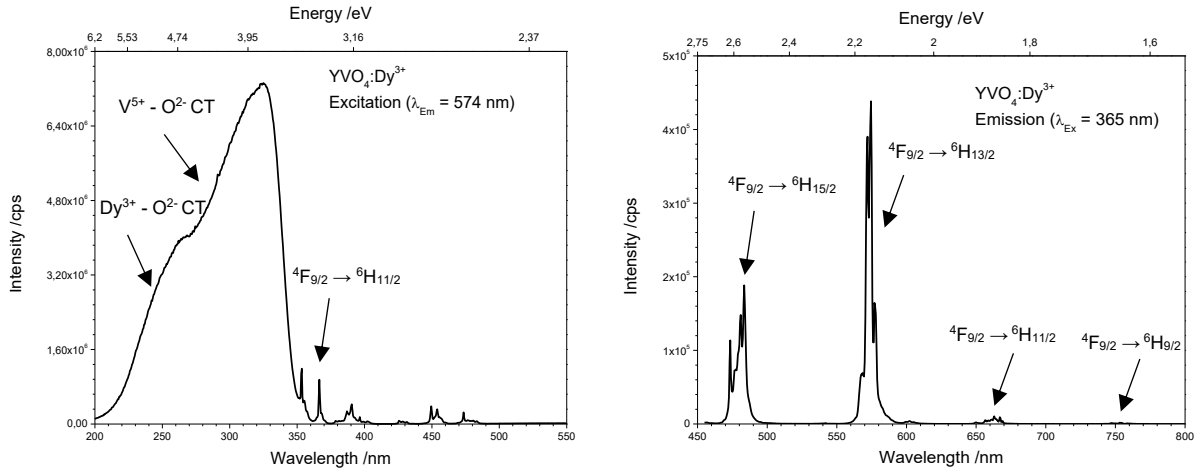

Figure 16: Excitation (left) and emission spectra (right) of $YVO_4:Dy^{3+}$

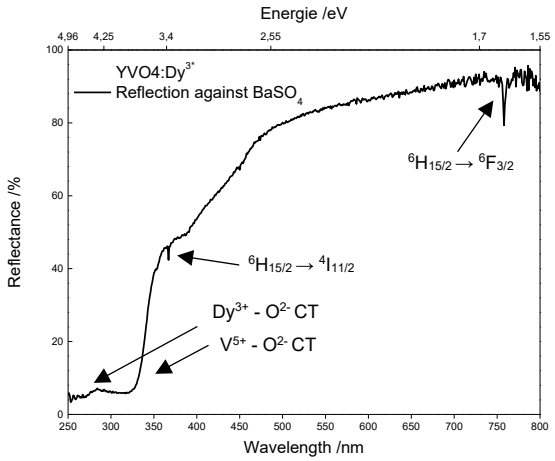

Figure 17: Reflection spectrum of $YVO_4:Dy^{3+}$

$Y(V,P)O_4:Eu^{3+}$

$Y(V,P)O_4:Eu^{3+}$ shows a broad band with a less intense shoulder in the UV region and several narrow lines in the long wavelength region in the excitation spectrum (see Figure 18). The observed broad band is centered at about 325 nm and can be attributed to the V^{5+} - O^{2-} charge transfer in the VO_4^{3-} group while the shoulder at 270 nm can be attributed to the overlap of the V^{5+} - O^{2-} with the Eu^{3+} - O^{2-} charge transfer transition [40] . The narrow lines correspond to the intra-configurational 4f - 4f transitions of the Eu^{3+}, which are parity and spin forbidden. The most intense line is at 395 nm and is assigned to the $^7F_0 \rightarrow {}^5L_0$ transition. Since the 4f electrons are shielded by the 5s and 5p orbitals, $\Delta R = 0$ applies. Due to a low-lying charge transfer state, emission lines appear in the red region of the electromagnetic spectrum. Excitation at 395 nm yields the characteristic transitions of Eu^{3+}. The transitions $^5D_0 \rightarrow {}^7F_1$ (595 nm), $^5D_0 \rightarrow {}^7F_2$ (615 nm and 619 nm), $^5D_0 \rightarrow {}^7F_3$ (652 nm) and $^5D_0 \rightarrow {}^7F_4$ (695 nm and 705 nm) are observed (see Figure 18). The emission spectrum is dominated by the hypersensitive transition $^5D_0 \rightarrow {}^7F_2$ and indicates an absence of a center of inversion symmetry. The broad absorption bands in the UV region in the reflection spectrum (see Figure 19) are attributed to the Eu^{3+} - O^{2-} and V^{5+} - O^{2-} charge transfer and are responsible for the white body color of $Y(V,P)O_4:Eu^{3+}$. Furthermore, the transitions $^7F_0 \rightarrow {}^5L_0$ (395 nm), $^7F_0 \rightarrow {}^5D_2$ (465 nm) and $^7F_0 \rightarrow {}^5D_1$ (537 nm) are observed, which show narrow less intense absorption bands [41] The calculated quantum efficiency is 40 % and is lower than the literature value of $YVO_4:Eu^{3+}$ with a quantum efficiency of 70 % [42]. Since the ratio between V^{5+} and P^{5+} as well as the Eu^{3+} concentration is not known, these deviations may occur.

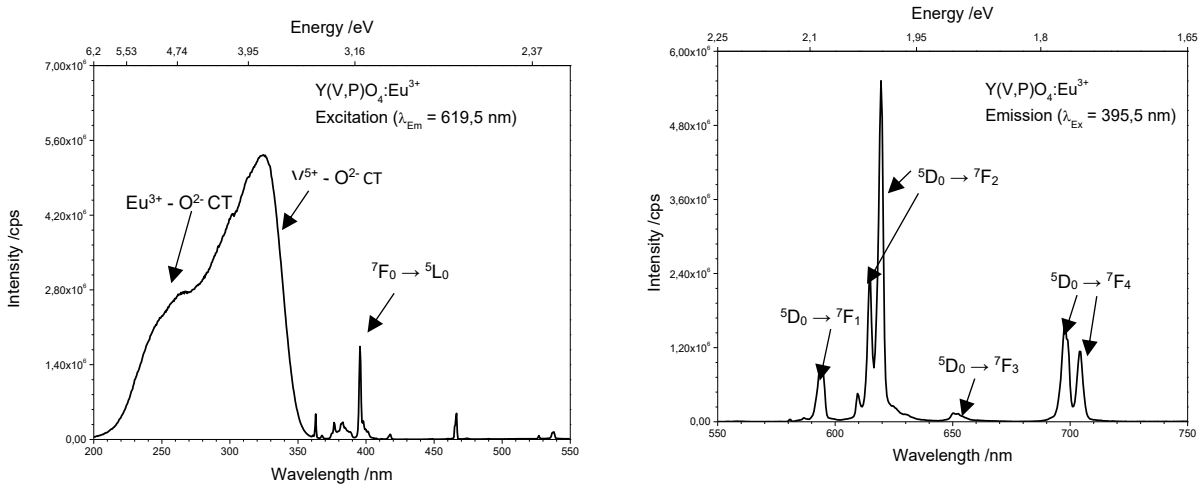

Figure 18: Excitation (left) and emission (right) spectra of $Y(V,P)O_4:Eu^{3+}$

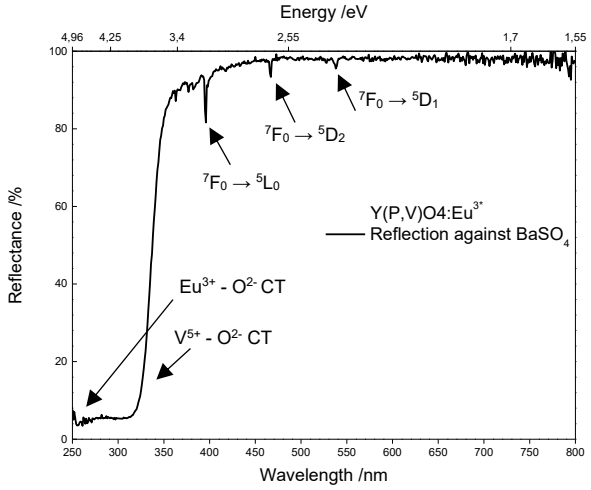

Figure 19: Reflection spectrum of $Y(V,P)O_4:Eu^{3+}$

YAG:Eu^{3+}

The excitation spectrum of YAG:Eu^{3+} (see Figure 20) shows an intense, broad band between 200 nm and 265 nm, which can be attributed to the ligand-metal charge transition between O^{2-} and Eu^{3+} [43] . In addition, there are several sharp lines in the longer wavelength region that can be attributed to the f-f transitions within the $4f^6$ configuration of Eu^{3+}. The sharp lines result from the shielded 4f electrons leading to $\Delta R = 0$ and a short Stokes shift. These transitions are spin and partially parity forbidden, leading to long lifetimes. The most intense line is at 394 nm and is due to the $^7F_0 \rightarrow {}^5L_6$ transition. By exciting the sample at 394 nm, the transitions $^5D_0 \rightarrow {}^7F_1$ (590 and 598 nm), $^5D_0 \rightarrow {}^7F_2$ (609 nm and 630 nm), $^5D_0 \rightarrow {}^7F_3$ (649 and 655 nm) and $^5D_0 \rightarrow {}^7F_4$ (696 and 712 nm) can be observed in the emission spectrum.

(see Figure 20). In contrast to $YVO_4:Eu^{3+}$, the $^5D_0 \rightarrow {}^7F_1$ transition has the most intense emission line at 590 nm. This indicates that there is inversion symmetry at the site of the Eu^{3+} ion. Consequently, the $^5D_0 \rightarrow {}^7F_1$ transition dominates the spectrum, since it occurs as a magnetic-dipole transition and obeys the selection rule J = 0, ±1. The broad absorption band in the range between 250 nm and 300 nm, which is due to Eu^{3+} - O^{2-} charge transfer, dominates the reflection spectrum (see Figure 21). This determines the white body color of the sample. Furthermore, the narrow absorption band at 395 nm shows the $^7F_0 \rightarrow {}^5L_6$ transition. The quantum efficiency measurement results in a value of 41 % for which no comparable literature values could be found. Due to the Eu^{3+} activator, a weak electron-phonon coupling applies and thus a high quantum efficiency is expected, which is why the measured value appears low and can be caused by quenching processes.

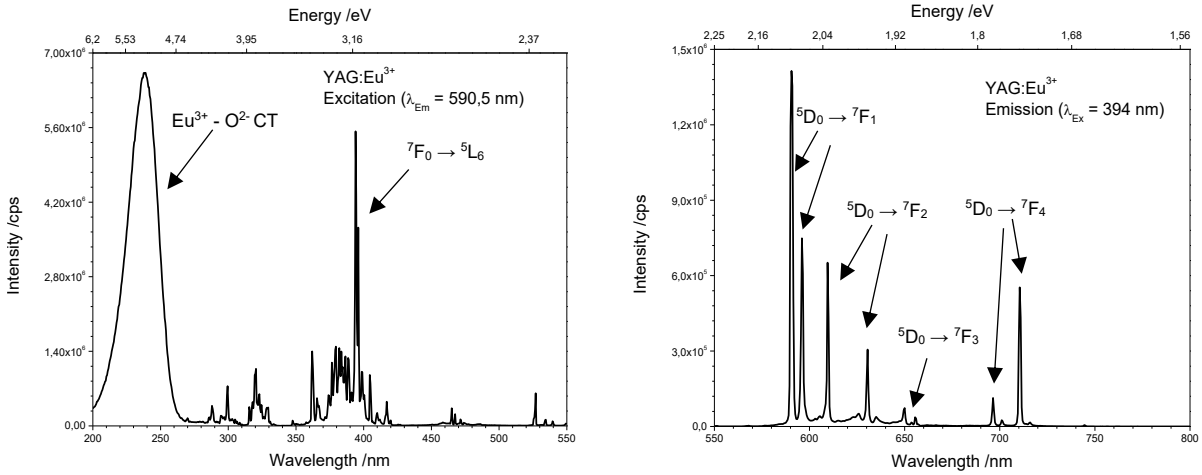

Figure 20: Excitation (left) and Emission (right) spectra of $YAG:Eu^{3+}$

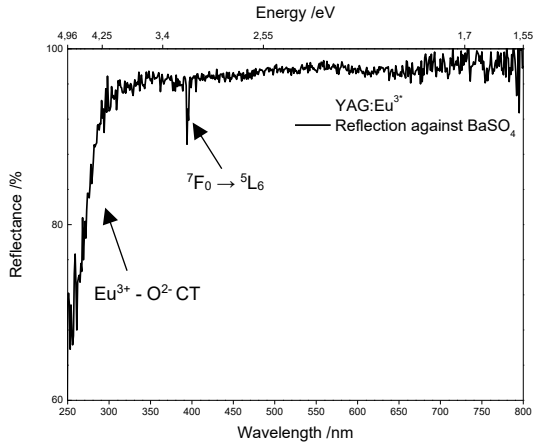

Figure 21: Reflection spectrum of $YAG:Eu^{3+}$

YAG:Dy^{3+} and LuAG:Dy^{3+}

YAG:Dy^{3+} and LuAG:Dy^{3+} show almost identical spectroscopic properties and are therefore investigated commonly in this section. In the excitation spectra, there are several broad but less intense bands in the UV range between 200 nm and 240 nm, which presumably correspond to the Dy^{3+} - O^{2-} charge transfer. Furthermore, there are several narrow peaks in the near ultraviolet and in the visible range, which are due to the intra-configurational 4f - 4f transitions of the Dy^{3+}, so that R = 0 applies. The most intense excitation wavelengths are at 355 nm and 366 nm, which are attributed to the $^6H_{15/2} \rightarrow {}^4M_{11/2}$, $^6P_{7/2}$ and $^6H_{15/2} \rightarrow {}^4I_{11/2}$ transitions (see Figure 22). According to the selection rules, these transitions are forbidden, which is why narrow emission lines result. Excitation by 366 nm results in several emission lines in the emission spectra which are observed in the blue (470 nm - 400 nm), yellow (560 nm - 600 nm), red (660 nm - 680 nm) and infra-red (760 - 770 nm) region, corresponding to $^4F_{9/2} \rightarrow {}^6H_{15/2}$, $^4F_{9/2} \rightarrow {}^6H_{13/2}$, $^4F_{9/2} \rightarrow {}^6H_{11/2}$ and $^4F_{9/2} \rightarrow {}^6H_{9/2}$ transitions (see Figure 23). The first two transitions result in the most intense emission lines. While the blue transition has a magnetic dipole character, the yellow transition is hypersensitive and strongly influenced by the chemical environment surrounding Dy^{3+} ions. Since the $^4F_{9/2} \rightarrow {}^6H_{15/2}$ transition is more intense than the $^4F_{9/2} \rightarrow {}^6H_{13/2}$ transition in the emission spectra, this is presumably due to inversion symmetry at the site of the Dy^{3+} ion. Depending on the ratio of these two emission lines, a white emission results for the two phosphors.

In the reflection spectrum, a broad absorption band in the UV range is visible, which presumably corresponds to the Dy^{3+} - O^{2-} charge transfer and is responsible for the white body color of the samples. Furthermore, two narrow absorption bands between 350 nm and 400 nm can be observed, which are caused by the transitions $^4F_{9/2} \rightarrow {}^6H_{15/2}$ and $^4F_{9/2} \rightarrow {}^6H_{13/2}$ (see Figure 24). The quantum efficiency of YAG:Dy^{3+} is 20 % and of LuAG:Dy^{3+} 63 % [44]. Due to the Dy^{3+} activator, a weak electron-phonon coupling applies and thus a high quantum efficiency is expected as for Eu^{3+}, which is why the measured values appear low and can be caused by quenching processes.

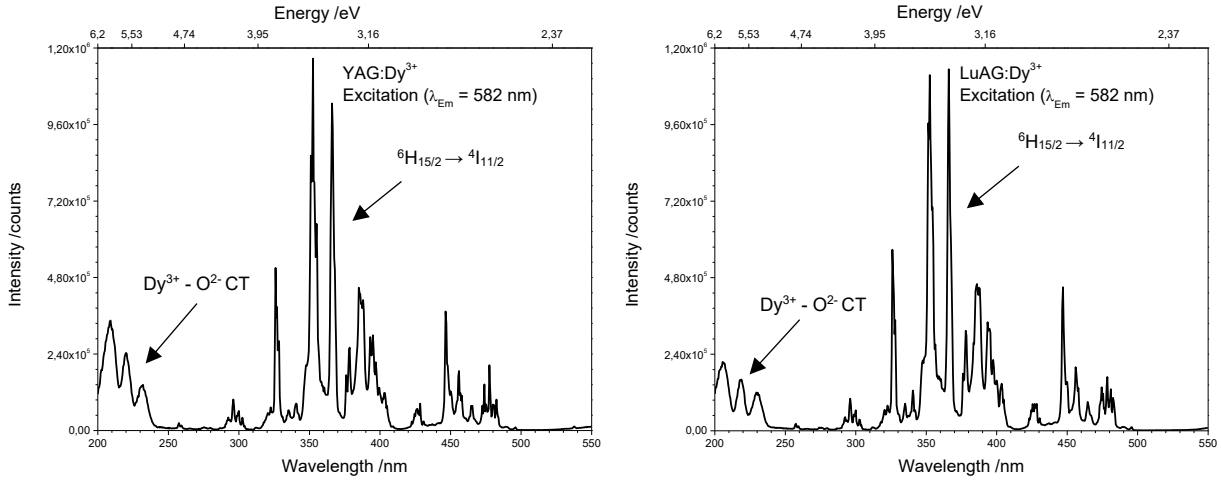

Figure 22: Excitation spectra of YAG:Dy^{3+} (left) and LuAG:Dy^{3+} (right)

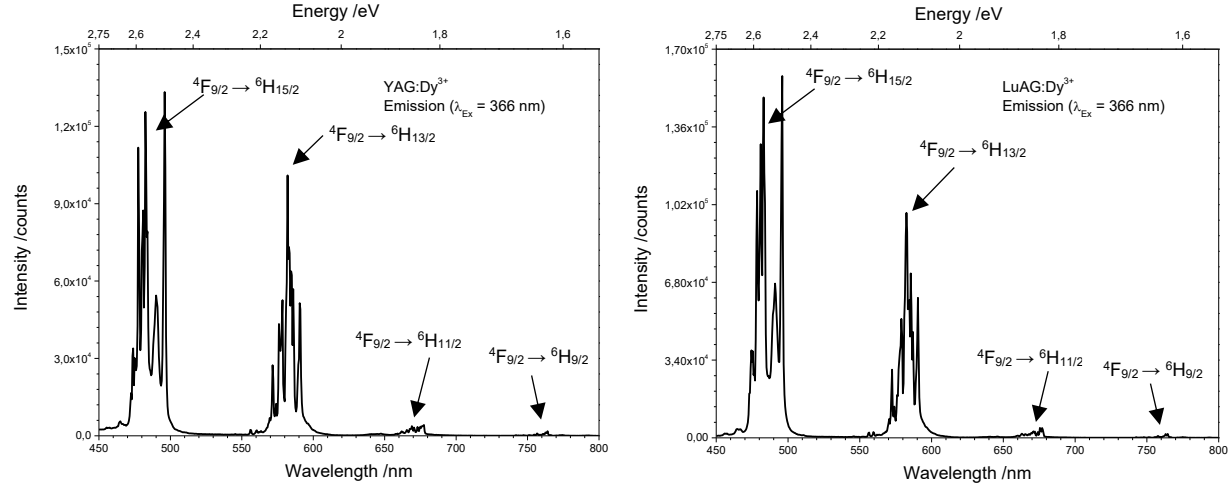

Figure 24: Emission spectra of YAG:Dy^{3+} (left) and LuAG:Dy^{3+} (right)

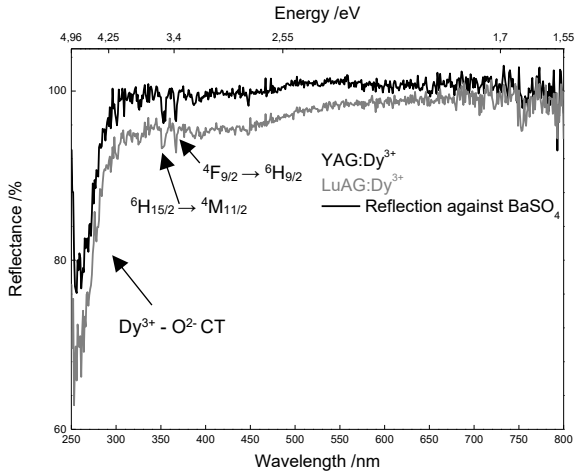

Figure 23: Reflection spectra of YAG:Dy^{3+} and LuAG:Dy^{3+}

4.5 Thermal quenching

In order to determine the influence of temperature on luminescence and to examine in which temperature range the phosphors are sensitive, temperature dependent excitation spectra are measured and if possible, the corresponding quenching curves of the phosphors are determined based on the measured temperature dependent emission spectra.

4.5.1 Nitride phosphor

The temperature dependent excitation and emission (see Figure 25) spectra of $(Sr_{1-x}Ca_x)AlSiN_3:Eu^{2+}$ indicate that the excitation and emission intensity decrease with increasing temperature through thermal quenching. Figure 26 shows normalized integrated values of the $(Sr_{1-x}Ca_x)AlSiN_3:Eu^{2+}$ emission spectra. Through a Boltzmann sigmoidal fit of the temperature dependent emission integrals and the resulting turning point of the course, $T_{1/2}$ can be calculated at 323 °C which describes the temperature that has decreased to the half of the maximum intensity of an emission integral [26]. The thermal quenching curve of the phosphor decreases only slightly up to 175 °C and can exhibit thermal stability up to this temperature. From this point, the curve drops rapidly to 425 °C, showing a strong sensitive temperature range between 175 and 425 °C. According to the temperature dependent emission spectra and the integrated values, increasing blackbody radiation occurs at higher temperatures, which is why the value at 475 °C is not calculated in the thermal quenching curve.

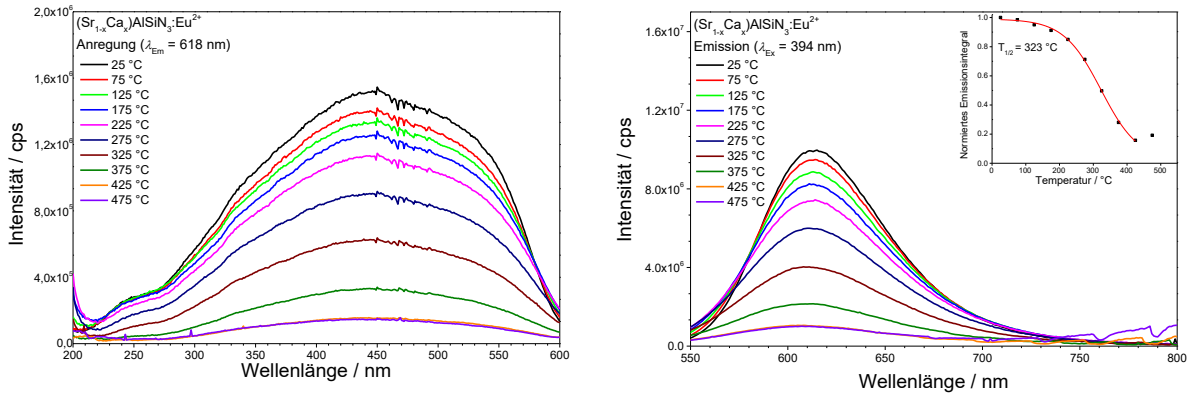

Figure 25: Temperature dependent excitation (left) and emission spectra (right) of $(Sr_{1-x}Ca_x)AlSiN_3:Eu^{2+}$

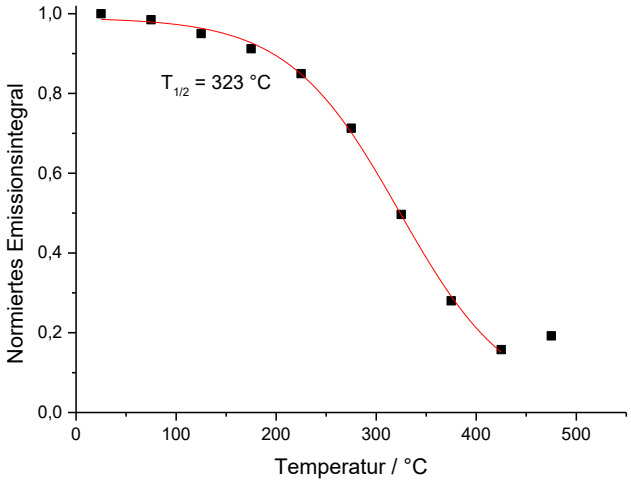

Figure 26: Thermal quenching curve of $(Sr_{1-x}Ca_x)AlSiN_3:Eu^{2+}$ between room temperature and 500 °C

4.5.2 Vanadate phosphors

The orthovanadate anion VO_4^{3-} exhibits a broad absorption in the ultraviolet range due to the V^{5+} - O^{2-} charge-transfer. This host lattice has the property that the charge transfer state is low-lying and shifts to longer wavelengths with increasing temperature, as it is observable in the temperature dependent excitation spectra of $YVO_4:Dy^{3+}$ and $Y(V,P)O_4:Eu^{3+}$ [45]. Consequently, the f-f excitation wavelengths of $YVO_4:Dy^{3+}$ at 366 nm and of $Y(V,P)O_4:Eu^{3+}$ at 395 nm overlap with the CT excitation band with increasing temperature and result in an increasing emission intensity (see Figure 27 and 28).

The inset in Figure 27 shows normalized integrated values of the temperature dependent emission spectra of $YVO_4:Dy^{3+}$ which are based on the excitation wavelength at 366 nm. The course of the data points shows an increase up to 275 °C due to the shift of the CT excitation band. Following this, it drops rapidly through thermal quenching. This could result in a sensitive temperature range between 275 °C and 450 °C for $YVO_4:Dy^{3+}$. The temperature ranges are speculative, as further measuring points would be required to be able to interpret the exact course. Since the integrated values do not follow a typical sigmoidal curve, the curve fitting and the determination of the quenching temperature are not carried out.

The course of the normalized integrated values of the temperature dependent emission spectra of $Y(V,P)O_4:Eu^{3+}$ shows a decrease up to 325 °C in the inset of Figure 28, due to thermal quenching and since there is no overlap yet between the CT excitation band and the

excitation wavelength at 395 nm. From this temperature upwards, the emission intensity increases and thus also the integrated values increase. Since the measurement could only be carried out up to 475 °C, the maximum temperature at which the highest emission intensity can be achieved as well as the sensitive temperature range due to the shift of the CT excitation band are unknown. As for $YVO_4:Dy^{3+}$, the curve fitting and the determination of the quenching temperature are not carried out.

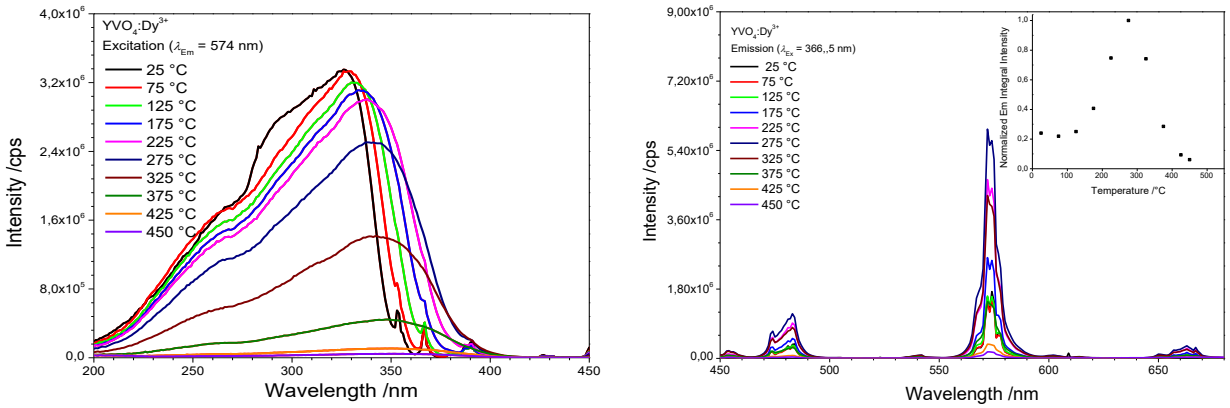

Figure 27: Temperature dependent excitation (left) and emission spectra (right) spectra of $YVO_4:Dy^{3+}$

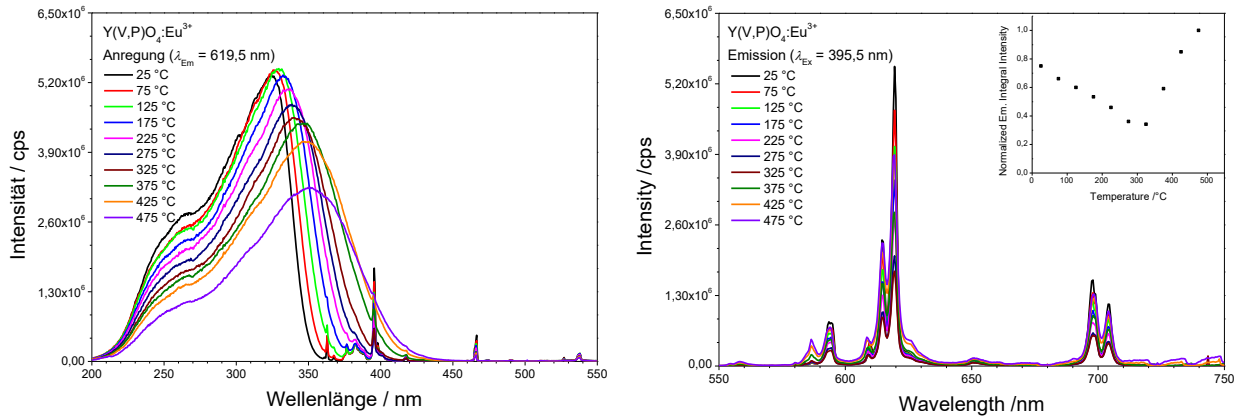

Figure 28: Temperature dependent excitation (left) and emission spectra (right) of $Y(V,P)O_4:Eu^{3+}$

4.5.3 Garnet phosphors

As the nitride phosphor, the investigated garnets $YAG:Eu^{3+}$, $YAG:Dy^{3+}$ and $LuAG:Dy^{3+}$ show a decrease in excitation and emission intensity (see Figure 29-31) with increasing temperature. The course of the normalized integrated values of the temperature dependent emission spectra of $YAG:Eu^{3+}$ (see inset of Figure 29) could show a part of the temperature sensitive range due to

a rapid decline. From a temperature of 375 °C upwards the integrated values increase as the excitation and the emission intensity is higher at 425 °C than at 375 °C which could be caused by a measurement error since this phenomenon is not known in the literature. The courses of the normalized integrated values of the phosphors YAG:$Dy^{3+}$and LuAG:Dy^{3+} show a flat decline. At a temperature of 475 °C the emission integrals have decreased to about 60 % of their maximum value, indicating that a further decrease is to be expected which agrees with the literature [4]. For this reason, the garnets are intended for temperatures up to 1000 °C for this work, but due to limitations in equipment, they can only be investigated up to 200 °C at DLR in Göttingen. Since the courses of the integrated values of the garnets do not show a sigmoidal curve or a turning point, the curve fitting and the determination of the quenching temperature are not carried out.

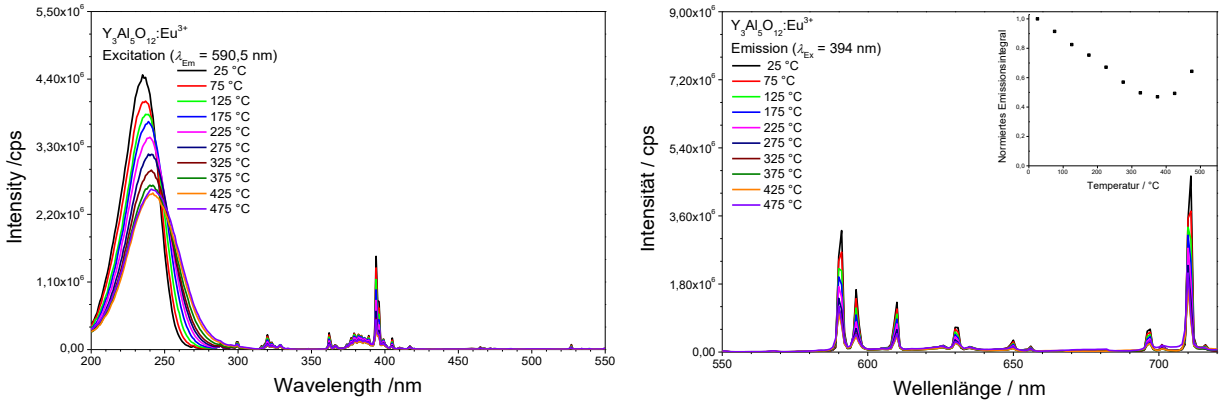

Figure 30: Temperature dependent excitation (left) and emission spectra (right) with emission intensity integrals (inset) of YAG:Eu^{3+}

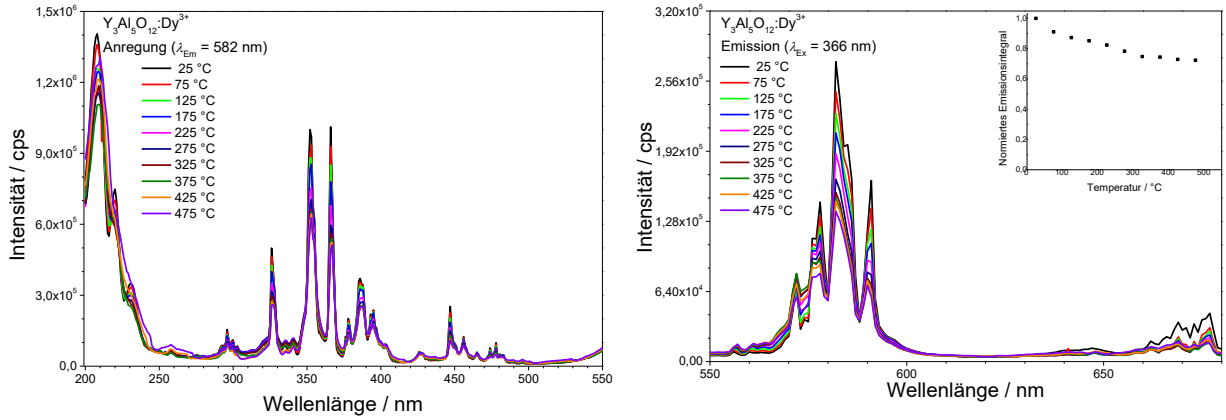

Figure 31: Temperature dependent excitation (left) and emission spectra (right) with emission intensity integrals (inset) of YAG:Dy^{3+}

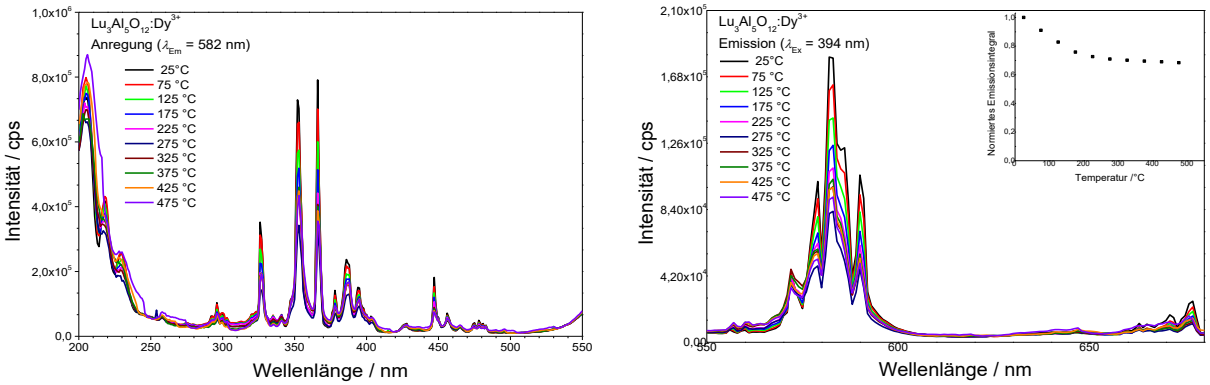

Figure 32: Temperature dependent excitation (left) and emission spectra (right) with emission intensity integrals (inset) of LuAG:Dy^{3+}

4.6 Development process of a TSP

To develop a TSP, paint samples are produced in different concentrations using the selected phosphors and binders described in chapter 2.4 and, if necessary, a suitable solvent, according to the laboratory reports (see appendix). The components are stirred and placed in an ultrasonic bath for 20 minutes. During preparation, attention must be paid to miscibility and viscosity to ensure sprayability. Then, the paint samples are sprayed with different layers on plates consisting of a nickel-steel alloy or of aluminum with a 3 cm x 3 cm size with the help of an airbrush gun equipped with a 1.2 mm needle. The plates are first sandblasted and cleaned with acetone to improve wettability. After spraying, the plates are dried at room temperature for 2 h and, if necessary, cured in a chamber oven at high temperatures which depend on the binder. The cured samples are stored in CD boxes.

The samples are first examined by temperature dependent emission spectra between 30 and 200 °C, according to the measurement technique from chapter 3.2.1. Subsequently, mechanical tests are carried out as described in chapter 3.2.3. Since the measurement of the temperature dependent lifetimes consumes a lot of time and a sufficient emission intensity is necessary, it is only carried out for samples with higher concentrations, which have good mechanical properties and high emission intensities.

As already mentioned in chapter 3.2.1.1, the paint samples are compared to the *OV322* TSP to determine if the paint samples show sufficient intensity to be considered as a new TSP. The emission spectrum of the reference TSP is measured at *high* sensitivity and at the same band widths as the paint samples. These include 3 nm and 10 nm for the excitation band width and 3 nm for the emission band width (see Figure 32). The emission spectrum with the band widths

10 nm x 3 nm reaches a maximum at ~ 580 cps while the emission spectrum with the band widths 3 nm x 3 nm peaks at ~ 140 cps at the emission peak 617 nm and an excitation wavelength of 395 nm.

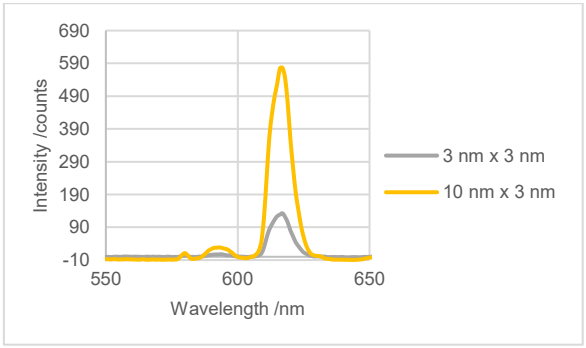

Figure 33: Emission spectra of OV322 with the band widths 3 nm x 3 nm and 10 nm x 3 nm

4.6.1 First attempt

To carry out first attempts with the selected binders and to find possible concentrations of the phosphors in the binders, they were combined with an alternative phosphor, the red emitting $Y_2O_3:Eu^{3+}$ phosphor.

4.6.1.1 Sample preparation

In order to reduce the viscosity of the binders, they were mixed with different solvents. Ceramabind 643-1, Ceramabind 880 and the ZAP Binder mixed with Thinner C25/90S formed two phases, while a white flaky precipitate was formed with ethanol. Nevertheless, they could be successfully mixed with distilled water. Through previous research at DLR, it was known to use concentrations with at least 100 mmol/L for inorganic TSPs. Therefore, phosphor concentrations of 100 mmol/L, 300 mmol/L and 700 mmol/L were used for each binder, according to the laboratory report in appendix, Figure 41 and 42. Since there was only one type of plate available in the beginning, the Ceramabind 643-1 samples were sprayed on aluminum plates while the Ceramabind 880 and the ZAP Binder samples were sprayed on nickel-steel alloy plates to be able to measure at higher temperatures. The plates were coated with 30 layers. After drying at room temperature, the Ceramabind 880 and the ZAP Binder samples have formed bubbles on the surface which is due to the high viscosity of the binders. The samples with Ceramabind 643-1 were cured for 1,5 h at 95 °C, 1,5 h at 175 °C and 1,5 h at 260 °C [7] while the samples with Ceramabind 880 were cured for 1 h at 230 °C [8]. The ZAP Binder samples were cured for 1 h at 600 °C as described in the data sheet [8]. However, this paint came off almost completely after curing, which was due to the high temperature paint according to a phone call with the *ZYP* company and recommend curing at room temperature.

Owing a low availability of Y_2O_3:Eu^{3+}, this attempt could not be repeated for the ZIP binder.

4.6.1.2 Intensity measurement

The emission spectra of the paint samples with Ceramabind 643-1 and Ceramabind 880 (see Figure 33) were measured at 30 °C and 200 °C with an excitation wavelength of 395 nm. As expected, a decrease in emission intensity with increasing temperature is observed, as well as an increase in emission intensity at higher concentrations. The emission spectra show that the Ceramabind 643-1 embedded sample reaches ~ 51 counts while the Ceramabind 880 embedded sample reach ~ 6 counts at the highest concentration. This indicates that the last-mentioned binder has a stronger interaction with the phosphor, which may also be the reason why no emission intensity could be measured for the sample with a low phosphor concentration of 100 mmol/L.

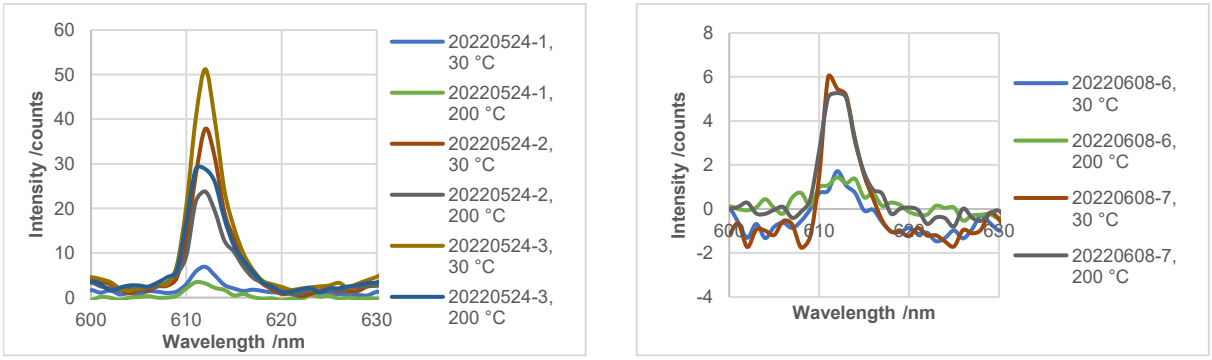

Figure 34: Temperature dependent emission spectra of Y_2O_3:Eu^{3+} with Ceramabind 643- 1 (left) and with Ceramabind 880 (right)

4.6.1.3 Mechanical Tests

The tape-test showed that the coating with Ceramabind 880 adhere well to the plate while the coating with Ceramabind 643-1 is almost removed from the plate, which can be seen from samples at a phosphor concentration of 300 mmol/L in Figure 34. With the help of the microscope it is possible to investigate the remaining residues on the plates (see Figure 35). It is shown that the microcracks gets smaller and the residues gets bigger with increasing concentration, so that the adhesion is improved.

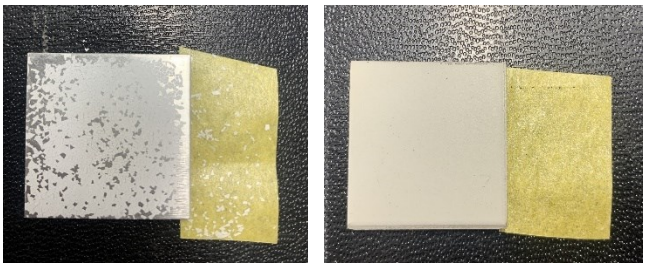

Figure 35: Samples 20220524-2 and 20220608-2 after the tape-test has been carried out

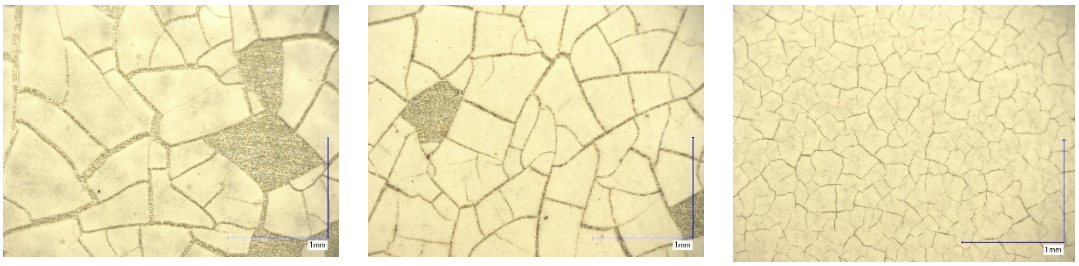

100 mmol/L 300 mmol/L 700 mmol/L

Figure 36: Illustration of microcracks on samples surfaces for different phosphor concentrations with a scale of 1 mm

Moreover, the samples with Ceramabind 880 have a mechanically workable surface and show roughness values below 10 µm which are in the desirable range. In comparison to those the samples with Ceramabind 641-1 show higher R_z-values (see Table 10).

Table 10: R_z-values for 20220524-1 to -3 and 20220608-5 to -7 samples

Sample number	Concentration /mmol*L^{-1}	R_z before sanding /µm	R_z after sanding /µm
20220524-1	100	33.2	-
20220524-2	300	19.7	-
20220524-3	700	14.6	-
20220608-5	100	2	1.23
20220608-6	300	2.99	2.85
20220608-7	700	2.96	2.18

4.6.1.4 Conclusion

To conclude, the viscosity of the selected binders can be reduced with water. A concentration of at least 300 mmol/L should be used for the samples to be able to measure emission intensity. Of the binders examined in chapter 4.4.1.2, the samples with Ceramabind 643-1 show the lowest interaction with the phosphor, but also high roughness values, which could not be reduced due to a non-mechanically workable surface. Meanwhile, Ceramabind 880 samples show comparatively low intensities but acceptable roughness values.

4.6.2 Second attempt

Based on the results from the first attempt, the phosphors to be examined for this project were mixed with the binders at a concentration of 300 mmol/L. As already mentioned in chapter 2.4, Ceramabind 880 is used for the phosphors $(Sr_{1-x}Ca_x)AlSiN_3:Eu^{2+}$, $YVO_4:Dy^{3+}$ and $Y(V,P)O_4:Eu^{3+}$ while Ceramabind 643-1 and ZIP binder are used for $YVO_4:Dy^{3+}$, $Y(V,P)O_4:Eu^{3+}$, $YAG:Eu^{3+}$, $YAG:Dy^{3+}$ and $LuAG:Dy^{3+}$.

4.6.2.1 Sample preparation

Due to the low availability of $LuAG:Dy^{3+}$ and $YAG:Dy^{3+}$ and their similar chemical properties, only $YAG:Dy^{3+}$ will be investigated with ZAP Binder. In contrast to the previous attempt, the Ceramabind 880 and ZAP Binder samples were mixed with water to prevent the formation of bubbles on the surface. The prepared Ceramabind 643-1 paint samples were sprayed on aluminum plates, while the Ceramabind 880 and the ZAP Binder samples were sprayed on nickel-steel alloy plates with 16 layers each which were then air dried and cured according to the labotary reports in the appendix, Figure 43 and 44. An overview of the samples are shown in Table 11.

4.6.2.2 Intensity measurement

After measuring the excitation wavelength of each sample at room temperature (see Table 11) the emission spectra of the samples were measured between 30 and 200 °C. After cooling the samples, they were measured again at 30 °C to control the hysteresis deviation, which corresponds to the changed intensity at the same temperature due to heating and cooling processes of the sample.

Table 11: Overview and excitation wavelength of the prepared samples 20220520-1 to -5 and 20220616-1 to -7

Sample number	Phosphor	Binder	Excitation wavelength / nm
20220520-1	$YVO_4:Dy^{3+}$	Ceramabind 643-1	368
20220520-2	$LuAG:Dy^{3+}$	Ceramabind 643-1	366
20220520-3	$Y(V,P)O_4:Eu^{3+}$	Ceramabind 643-1	395
20220520-4	$YAG:Eu^{3+}$	Ceramabind 643-1	397
20220520-5	$YAG:Dy^{3+}$	Ceramabind 643-1	366
20220616-1	$YVO_4:Dy^{3+}$	Ceramabind 880	370
20220616-2	$(Sr_{1-x}Ca_x)AlSiN_3:Eu^{2+}$	Ceramabind 880	450
20220616-3	$Y(V,P)O_4:Eu^{3+}$	Ceramabind 880	397

20220616-4	$YVO_4:Dy^{3+}$	ZAP Binder	370
20220616-5	$Y(V,P)O_4:Eu^{3+}$	ZAP Binder	399
20220616-6	$YAG:Eu^{3+}$	ZAP Binder	395
20220616-7	$YAG:Dy^{3+}$	ZAP Binder	366

As expected, the emission spectra of the samples show a decreasing emission intensity with increasing temperature with the exception of $YVO_4:Dy^{3+}$. By comparing the samples with the different binders, it is observed that the Ceramabind 643-1 binder has the lowest interaction with the phosphors, followed by the Ceramabind 880 and the ZAP Binder. In addition, the samples with the ZAP Binder show a dark discoloration after measuring at 200 °C (see appendix, Figure 45), which indicates a temperature instability of the binder or interaction and oxidation process between the binder and sample substrate material. For the phosphors $YAG:Dy^{3+}$ and $LuAG:Dy^{3+}$, barely any emission intensity could be measured, which can be attributed to the binder.

The maximum emission intensity is for the sample $YVO_4:Dy^{3+}$ with Ceramabind 643-1 at 200 °C and a wavelength of 575 nm, which reaches over 1000 cps and is no longer detectable due to an increasing intensity caused by the shift of the CT excitation band. In comparison to that, the sample 20220616-1 peaks at ~ 63 cps while 20220616-4 peaks at ~ 57 cps at 200 °C (see Figure 36). In contrast to the OV322 sample, these two samples show low intensities, which is why higher concentrations should be chosen. It is noticeable that there is no hysteresis deviation for any of the samples, which emphasizes the stability of the colors. The measured spectra of each sample at different temperatures can be found in the appendix, Figure 46.

In contrast to $YVO_4:Dy^{3+}$, $Y(V,P)O_4:Eu^{3+}$ shows less intensity. Sample 20220520-2 displays at 30 °C and a wavelength of 620 nm an emission intensity maximum at ~ 98 cps with a high hysteresis deviation of 22 %, while sample 20220616-3 shows no deviation with a maximum intensity at ~ 28 cps and sample 20220616-5 peaks at ~ 11 cps with a drop of 18 % (see appendix, Figure 46). In addition, sample 20220616-3 shows a broad peak between 550 and 650 nm, which indicates contamination with $(Sr_{1-x}Ca_x)AlSiN_3:Eu^{2+}$. However, these values are not comparable, since an increasing intensity is to be expected from a temperature of 325 °C and only this temperature range becomes interesting for this project.

$(Sr_{1-x}Ca_x)AlSiN_3:Eu^{2+}$ indicates a broad emission band at 30 °C and at a wavelength of 605 nm, which peaks at ~ 172 cps and shows a drop of 11 %, as can be seen in Figure 37. Compared to the OV322 TSP, the intensity still appears low. The lowest emission intensity is shown for $YAG:Eu^{3+}$ with ~ 23 cps for 20220520-4 and ~ 9 cps for 20220616-6, while the last one shows a high hysteresis deviation of 66 % (see Figure 37)

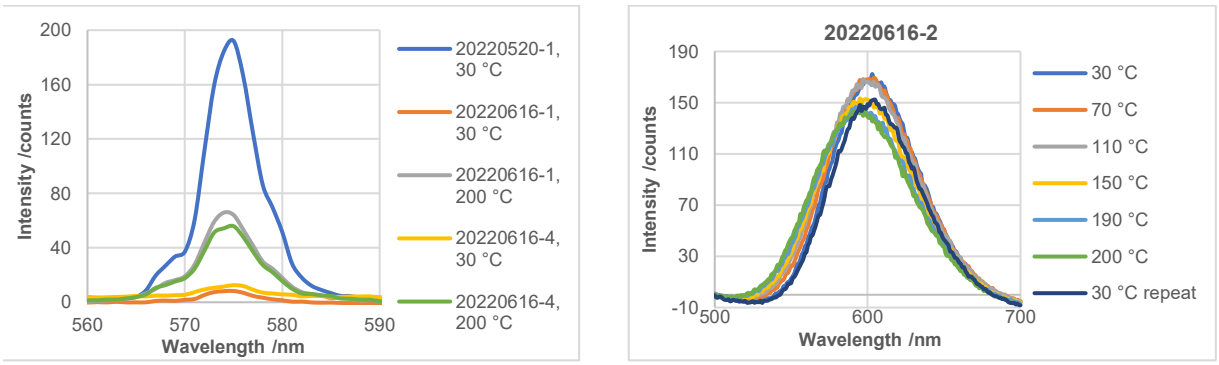

Figure 37: Temperature dependent emission spectra of YVO4:Dy^{3+} with different binders and of sample number 20220616-2

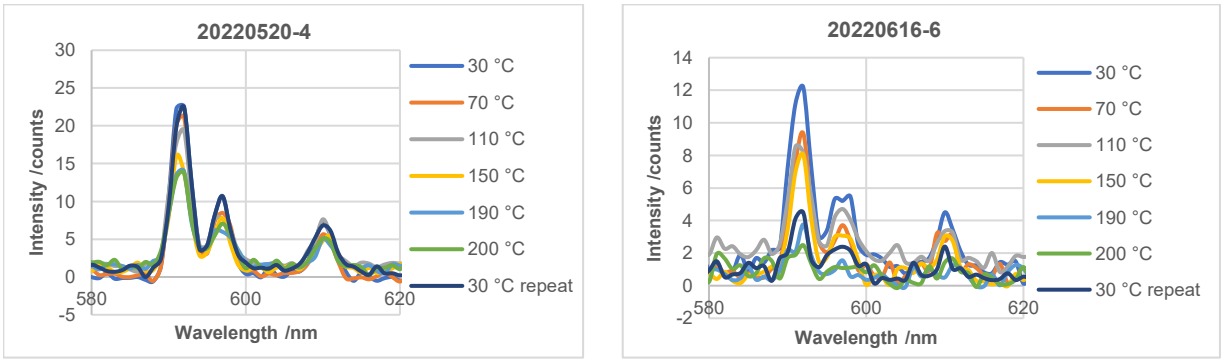

Figure 38: Temperature dependent emission spectra of YAG:Eu^{3+} with Ceramabind 880 (left) and with ZAP Binder (right)

4.6.2.3 Mechanical Tests

From the tape test it can be concluded that the coating of the samples 20220520-1 to -5 does not adhere to the aluminium plates as in the first attempt, while the Ceramabind 880 and ZAP Binder samples adhere easily to the nickel-steel samples and have a smooth surface. In contrast to the Ceramabind 643-1 samples, these also show a low roughness, a mechanically workable surface and layer thickness values below 20 µm (see Table 12), although values below 10 µm are aimed for.

Table 12: R_z-values and layer thickness values of the samples 20220520-1 to -5 and 20220616-1 to -7

Sample number	R_z before sanding /µm	R_z after sanding /µm	Layer thickness /µm
20220520-1	20.24	-	-
20220520-2	18.0	-	-
20220520-3	20.5	-	-
20220520-4	21.4	-	-
20220520-5	23.1	-	-
20220616-1	2.38	2.06	22.5
20220616-2	3.75	3.18	13.9
20220616-3	3.42	2.39	22.4
20220616-4	12	8.9	15.2
20220616-5	4.57	3.48	12.8
20220616-6	15.8	9.2	14.4
20220616-7	13.7	6.63	12

4.6.2.4 Conclusion

The measurements show that the Ceramabind 643-1 binder have a smaller interaction with the phosphors than the other binders which results in high emission intensities, but the resulting values and properties from the mechanical tests are far below the desired range, which could be due to the plates, the large particle sizes and the quenching influence of the components of the binder. Furthermore, it turns out that the intensity hysteresis deviation is not only dependent on the phosphor, there is also a dependence on the binder. In addition to the lowest emission intensities and the coloration during heating up to 200 °C, ZAP binder shows the greatest intensity hysteresis deviations.

4.6.3 Third attempt

Based on the results from the second attempt, the particle sizes of the phosphors were reduced by a ball mill at the FH Münster University of Applied Sciences to improve the mechanical properties. The d_{50} **–** values of the particle sizes are given in Table 12 and are taken from the measured particle size distributions (see appendix, Figure 47). Since the particle size could influence the spectroscopic properties of the phosphors, the spectroscopic measurements described in chapter 3.1 should be repeated. Due to time limitations, only the measurements from the previous chapter will be repeated to determine the extent of the influence.

Table 13: measured d_{50} - values of the phosphors after optimization

Phosphor	d_{50} – value /µm
$(Sr_{1-x}Ca_x)AlSiN_3:Eu^{2+}$	12.39
$YVO_4:Dy^{3+}$	6.55
$Y(V,P)O_4:Eu^{3+}$	4.97
$YAG:Eu^{3+}$	10.71
$YAG:Dy^{3+}$	8.56
$LuAG:Dy^{3+}$	8.51

4.6.3.1 Sample preparation

All the prepared paint samples were sprayed on nickel-steel alloy plates with 16 layers each which were then air dried and cured according to the laboratory reports in the appendix, Figure 48. Due to the low availability of $LuAG:Dy^{3+}$ and $YAG:Dy^{3+}$, $YAG:Dy^{3+}$ will be only investigated with ZAP Binder and $LuAG:Dy^{3+}$ with Ceramabind 643-1. An overview of the samples is shown in Table 14.

Table 14: Overview of the prepared samples 20220630-1 to -11

Sample number	Phosphor	Binder
20220630-1	$YVO_4:Dy^{3+}$	Ceramabind 643-1
20220630-2	$YVO_4:Dy^{3+}$	Ceramabind 880
20220630-3	$YVO_4:Dy^{3+}$	ZAP Binder
20220630-4	$Y(V,P)O_4:Eu^{3+}$	Ceramabind 643-1
20220630-5	$Y(V,P)O_4:Eu^{3+}$	Ceramabind 880
20220630-6	$Y(V,P)O_4:Eu^{3+}$	ZAP Binder
20220630-7	$YAG:Eu^{3+}$	Ceramabind 643-1
20220630-8	$YAG:Eu^{3+}$	ZAP Binder
20220630-9	$(Sr_{1-x}Ca_x)AlSiN_3:Eu^{2+}$	Ceramabind 880
20220630-10	$LuAG:Dy^{3+}$	Ceramabind 643-1
20220630-11	$YAG:Dy^{3+}$	ZAP Binder

4.6.3.2 Intensity measurement

The temperature dependent emission spectra were measured under the same conditions and at the same excitation wavelengths as in chapter 4.4.2.2 (see appendix, Figure 49). The spectra show no shift of the emission wavelengths. The emission intensity of the Ceramabind 643-1 samples has decreased due to the optimization of the particle sizes. This is most noticeable for $YVO_4:Dy^{3+}$ due to the significant drop from over ~ 1000 cps to ~ 140 cps at 200 °C and for $Y(V,P)O_4:Eu^{3+}$ due to the drop from ~ 95 cps to ~ 25 cps at 30 °C. In contrast, an increase in emission intensity is observable for the Ceramabind 880 and the ZAP Binder samples. A strong increase is especially observable for $YVO_4:Dy^{3+}$ with Ceramabind 880, as the intensity doubled to 120 cps at 200 °C. The optimization did not improve the intensity hysteresis deviation except for the sample 20220630-9 which barely shows any deviation anymore. Furthermore, no emission intensity could be measured for the $YAG:Dy^{3+}$ and $LuAG:Dy^{3+}$ samples and the ZAP Binder samples show a dark discoloration, as in the previous attempt.

4.6.3.3 Mechanical tests

The results of the mechanical tests show good adhesion, low roughness values < 10 µm and an improvement in the layer thickness of the Ceramabind 880 and ZAP binder samples, as can be seen in Table 15. Furthermore, an improvement in the adhesion of the garnet phosphors with Ceramabind 643-1 samples can be observed, as well as mechanically workable surfaces, whereby the high roughness values can be improved. However, no improvement in the mechanical properties of the vanadate phosphors with Ceramabind 641-1 can be observed.

Table 15: R_z - and layer thickness values of the samples 20220630-1 to -11

Sample number	R_z before sanding /µm	R_z after sanding /µm	Layer thickness /µm
20220630-1	19.9	-	-
20220630-2	3.23	2.11	14.6
20220630-3	7.15	3.93	6.7
20220630-4	27.5	-	-
20220630-5	6.03	2.65	7.3
20220630-6	4.68	3.60	12.3
20220630-7	35.6	16.9	23
20220630-8	13.8	9.1	16.9
20220630-9	3.49	2.23	13.5

20220630-10	20.3	9.8	13.4
20220630-11	6.49	2.94	11
20220630-10	20.3	9.8	13.4
20220630-11	6.49	2.94	11

4.6.3.4 Conclusion

The measurements show overall positive results due to the optimization of the particle sizes, except for the measurement of the emission intensities of the Ceramabind 643-1 samples due to the drop in intensity. The ZAP Binder samples show comparatively low intensities and discolouration, which leads to an unsuitability of this binder for the development of a TSP. The phosphors YAG:Dy^{3+} and LuAG:Dy^{3+} do not show measurable emission intensities, which is why further tests with these phosphors in combination with the available binders are not carried out. Furthermore, the adhesion of the Ceramabind 643-1 samples could only be improved with the garnet phosphors. For this reason, this binder will only continue to be investigated in combination with YAG:Eu^{3+}.

4.6.4 Fourth attempt

Based on the results of the fourth attempt, the phosphors $(Sr_{1-x}Ca_x)AlSiN_3:Eu^{2+}$, $YVO_4:Dy^{3+}$ and $Y(V,P)O_4:Eu^{3+}$ in combination with the binder Ceramabind 880 as well as YAG:Eu^{3+} with Ceramabind 643-1 are examined in different high concentrations and layers to improve the emission intensities and layer thickness.

4.6.4.1 Sample preparation

To achieve an applicable TSP, samples were prepared with phosphor concentrations between 600 mmol/L and 1500 mmol/L depending on the availability of the phosphor and the coat-layers were varied. When spraying the samples on nickel-steel alloy plates, the airbrush gun was clogged for the vanadate phosphor samples at a concentration of 1500 mmol/L, therefore the concentration was reduced to 1200 mmol/L by adding distilled water for successful spraying. The laboratory report can be found in the appendix (see Figure 50-52) and an overview of the samples is given in Table 16.

Table 16: Overview of the prepared samples 20220707-1 to -4, 20220713-1 to -10 and 20220719-1,2

Sample number	Phosphor	Concentration / mmol*L^{-1}	Coat-layers
20220707-1,2	$(Sr_{1-x}Ca_x)AlSiN_3:Eu^{2+}$	900	8, 14
20220707-3,4	$(Sr_{1-x}Ca_x)AlSiN_3:Eu^{2+}$	1500	8, 12
20220713-1,2	$YAG:Eu^{3+}$	600	10, 14
20220713-3,4	$YVO_4:Dy^{3+}$	900	8, 14
20220713-5,6	$YVO_4:Dy^{3+}$	1200	6, 10
20220713-7,8	$Y(V,P)O_4:Eu^{3+}$	900	8, 14
20220713-9,10	$Y(V,P)O_4:Eu^{3+}$	1200	6, 10
20220719-1,2	$YAG:Eu^{3+}$	900	8, 14

4.6.4.2 Intensity measurement

The samples were excited with the same wavelengths as in chapter 4.6.2 and the emission spectra were measured between 30 and 200 °C. As expected, the samples show higher emission intensities with increasing concentration and number of coated layers (see appendix, Figure 53). The $(Sr_{1-x}Ca_x)AlSiN_3:Eu^{2+}$ samples clearly show the highest emission intensities, whereby sample 20220707-4 shows intensities above 1000 cps and is no longer detectable. Sample 20220707-1 already shows a maximum intensity of ~ 500 cps at a phosphor concentration of 900 mmol/L and 8 coat-layers (see Figure 39), which exhibits sufficient intensity in comparison with the OV322 sample to be considered as a TSP with regard to the luminescence properties. It should be noted that the intensity hysteresis deviation is below 5% for all four $(Sr_{1-x}Ca_x)AlSiN_3:Eu^{2+}$ samples.

The $YVO_4:Dy^{3+}$ sample 20220713-3 shows an emission maximum of ~ 210 cps (see Figure 38) at the lowest used concentrations and lowest number of coat-layers in this attempt while the emission maximum of the sample 20220713-6 with the highest concentration and coat-layers peaks at 540 cps at 200 °C. Since an increase in emission intensity can be expected at higher temperatures, a concentration of 900 mmol/L could already be sufficient to reach intensity values close to those of the OV322 sample. Meanwhile, the $Y(V,P)O_4:Eu^{3+}$ samples still show comparatively low intensities. The sample 20220713-10 with the highest concentration and the largest number of coat-layers reaches an emission maximum of ~ 165 cps at 30 °C (see Figure 38). As already mentioned, an increase in emission intensity can be expected from about 325 °C, which is why this phosphor could become interesting at higher temperatures.

YAG:Eu^{3+} still shows comparably the lowest intensities. The highest intensity of the four investigated YAG:Eu^{3+} samples is shown by sample 20220713-2, which peaks at ~ 28 cps (see Figure 38). These samples as well as the samples with the vanadate phosphors show an improvement of the intensity hysteresis deviation in this attempt, which is below 10 % for all these samples.

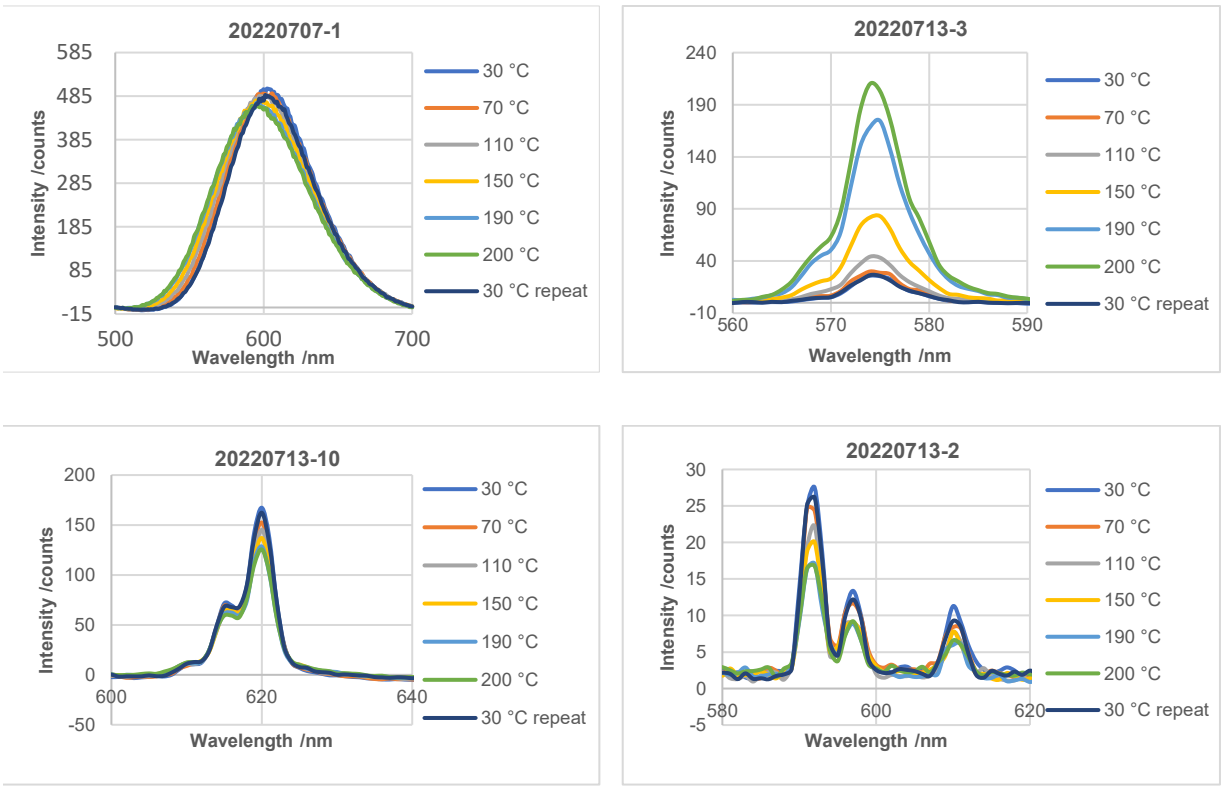

Figure 39: Temperature dependent emission spectra of the samples 20220707-1 and 20220713-2, 3, 10

Moreover, the temperature sensitivities of the $(Sr_{1-x}Ca_x)AlSiN_3:Eu^{2+}$ and YAG:Eu^{3+} paint samples were potted (see appendix, Figure 54), according to the equations 9 and 10. Temperatures sensitivities at 100 and 200 °C of those samples.are given in Table 17. As expected, the values show an increase in sensitivity with increasing temperature. To observe higher values, emission spectra would have to be measured at higher temperatures to cover the entire sensitive range.

Table 17: Temperature sensitivities calculated with equation 9 and 10 for samples 20220707-1 to -3, 20220719-1,2 and 20220713-2 at 100 and 200 °C

Sample number	T_{sens} at 100 °C /% * °C^{-1}	T_{sens} at 200 °C /% * °C^{-1}
20220707-1	0.080	0.103
20220707-2	0.003	0.017
20220707-3	0.002	0.007
20220713-2	1.432	4.231
20220719-1	1.345	12.01
20220719-2	1.426	2.366

4.6.4.3 Mechanical Tests

All 16 samples were mechanically workable and not affected by the tape test. Table 18 gives the results of the roughness measurements before and after sanding as well as the layer thickness measurements of all samples. The data show that the roughness values could be improved. Nevertheless, it should be noted that the Ceramabind 643-1 samples show high roughness values at 900 mmol/l and the Ceramabind 880 samples at a concentration of 1500 mmol/L mmol/l. The layer thickness values are between 10 and 30 µm and therefore not in the desired range, which is why a reduction of the number of layers is necessary mmol/l before sanding. The layer thickness values are between 10 and 30 µm and therefore not in the desired range, which is why a reduction of the number of layers is necessary.

Table 18: R_z - and layer thickness values of the samples 20220707-1 to -4, 20220713-1 to -10 and 20220719-1,2

Sample number	R_z before sanding / µm	R_z after sanding / µm	Layer thickness / µm
20220707-1,2	8.16, 5.83	5.93, 3.56	11.1, 21.5
20220707-3,4	26.4, 34.8	11.60, 14.70	13.8, 21.2
20220713-1,2	24.1, 18.6	9.26, 6.44	18.1, 28
20220713-3,4	11.6, 9.3	4.90, 5.64	12.7, 19
20220713-5,6	10.2, 5.34	7.36, 3.00	24.1, 29.1
20220713-7,8	7.49, 2.36	2.53, 2.16	19.1, 29.8
20220713-9,10	6.44, 4.41	3.43, 3.19	13.2, 28.4
20220719-1,2	36.4, 40.8	12.7, 13.5	10.6, 21.5

4.6.4.3 Lifetime measurement

Lifetime measurements were conducted at approximately 0, 30 and 60 °C using the method described in chapter 3.2.2. Using a 395 nm LED from *HARDsoft*, no signal could be measured for the $Y(V,P)O_4:Eu^{3+}$ and $YAG:Eu^{3+}$ samples, which is due to the low emission intensities. Similarly, by using a 366 nm LED from *Osram*, barely any signal could be measured for the $YVO_4:Dy^{3+}$ samples, which is caused by the low emission intensities at the measured temperatures, but also due to the long switch-off process of the LED, which completely overlaps with the low signal of the sample. To reduce this process, the power electronics of the LED must be modified for future investigations. Using a 450 nm LED from *HARDsoft,* samples 20220707-1,3 could be measured successfully. For sample 20220707-3, a measurement error occurred at 60 °C, which is why only two measurement points are considered. It is found that the decay curves of the $(Sr_{1-x}Ca_x)AlSiN_3:Eu^{2+}$ samples can be well fitted by the mono-exponential function (see Figure 39). In the case of sample 20220707-1 values of τ are 0,77, 0,74 and 0,73 µs while the measured values of sample 20220707-3 are 0,80 and 0,78 µs. It is shown that τ values decrease with increasing temperature due to thermal quenching. The deviation of the lifetimes of the two samples is ~ 5 % and could be caused by the variation of the coat-layers as well as the amount of the embedded phosphor.

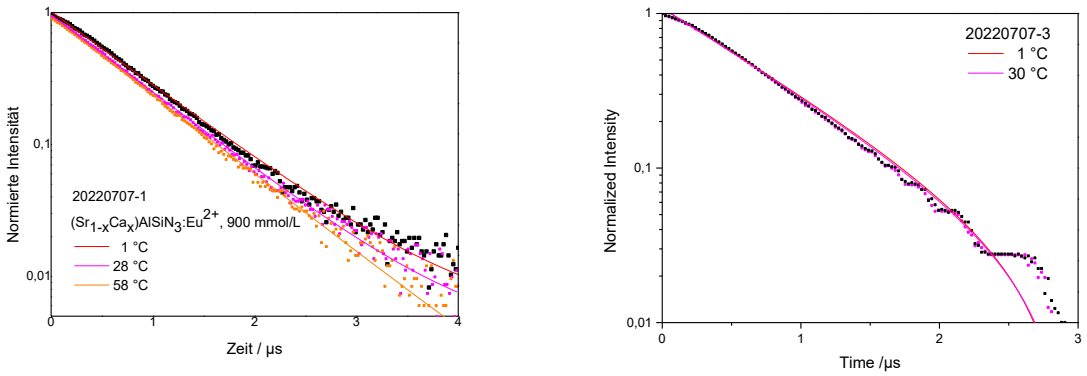

Figure 40: Decay curves of the samples 20220707-1 and -3 in the temperature range 0 - 60 °C

4.6.4.3 Conclusion

The attempt has shown that the roughness values increase at high concentrations, which is why arbitrarily high concentrations are not always practical in addition to the high material consumption. The phosphor $YAG:Eu^{3+}$ embedded in Ceramabind 643-1 shows low emission intensities despite high concentrations, which is why no lifetimes could be measured. Similarly, this also applies to the phosphors $YVO_4:Dy^{3+}$ and $Y(V,P)O_4:Eu^{3+}$ embedded in Ceramabind 880. However, these show an increase in emission intensity at higher temperatures, which is

why this attempt should be repeated at high temperatures if possible and the concentration and number of layers can be reduced according to the results. The attempt proved to be successful for the samples with $(Sr_{1-x}Ca_x)AlSiN_3:Eu^{2+}$, as the results of the intensity and lifetime measurements as well as those of the mechanical tests, which can be further optimized, are in agreement with the requirements of a TSP.

5 Conclusions and Outlook

The results of the characterization methods for qualifying the phosphors $(Sr_{1-x}Ca_x)AlSiN_3:Eu^{2+}$, $YVO_4:Dy^{3+}$, $Y(V,P)O_4:Eu^{3+}$, $YAG:Eu^{3+}$, $YAG:Dy^{3+}$ and $LuAG:Dy^{3+}$ have shown that the phosphors can be excited in the near UV range as well as for $(Sr_{1-x}Ca_x)AlSiN_3:Eu^{2+}$ in the blue range at 450 nm. The sharp emission lines corresponding to the phosphors with the weak electron-phonon coupling and the broad emission band of the Eu^{2+} phosphor are between 570 nm and 620 nm, which ensures a large Stokes shift. However, the measured quantum efficiencies of the synthesized phosphors show low values compared with the literature values, which could be improved by optimizing the synthesis such as a stepwise calcination. In addition, $YVO_4:Dy^{3+}$ shows an extremely low quantum efficiency of 1 %, which is also shown in the reflectance spectrum and the XRD pattern, which is why significantly improved spectroscopic properties can be expected if the synthesis is optimized. Furthermore, by measuring temperature dependent excitation and emission spectra between 25 and 450 °C, a red shift of the V^{5+} - O^{2-} CT band could be observed for the vanadate phosphors, which is why the emission intensities increase with increasing temperature up to a certain point when excited via the f-f transition and then drop due to thermal quenching. Therefore, it can be concluded that these phosphors are particularly interesting for this project because of their high quenching temperatures. For the exact course of the thermal quenching curves, further measurements should be carried out at higher temperatures in future and measurements with smaller temperature intervals should be carried out when the emission intensity increases. The garnets show only one part of the thermal quenching curve in the measured temperature range, which indicates a high thermal stability, while for $(Sr_{1-x}Ca_x)AlSiN_3:Eu^{2+}$a quenching temperature of 323 °C could be determined. The measurements show that the phosphors could reach higher quantum efficiencies but still fulfil the requirements for a suitable phosphor for the first step towards the development of a high temperature TSP.

The emission spectra of the embedded phosphors in the binders have shown that the ZAP binder is unsuitable for this project due to the discoloration at measurements up to 200 °C. Furthermore, the samples with the Ceramabind 643-1 binder show less favorable mechanical

properties compared to the ZAP and Ceramabind 880 binders, which could only be improved for the garnet samples by optimization of the particle sizes. Nevertheless, the two other binders provide better mechanical properties due to low roughness values, high adhesion to the nickel-steel alloy plates and a smooth surface. It is also remarkable that the particle size has an influence on the optical properties of the phosphors, which is why the phosphors should be ground down before characterizing the phosphors in future.

Moreover, the emission spectra of the prepared paints show that the selected binders strongly interact with the phosphors, resulting in hardly any emission intensities for the YAG:Dy^{3+} and LuAG:Dy^{3+} samples and low emission intensities for the YAG:Eu^{3+} and Y(V,P)O_4:Eu^{3+} samples despite high concentrations up to 1200 mmol/L, which is why no lifetimes could be measured. Meanwhile, the $(Sr_{1-x}Ca_x)AlSiN_3$:Eu^{2+} samples with phosphor concentrations between 900 mmol/L and 1500 mmol/L show high emission intensities compared to the OV322 sample and to the other phosphors, which can also be attributed to the allowed 4f → 5d transition. Therefore, it was possible to measure the lifetimes of the samples, which are ~ 1 µs. In addition, the YVO_4:Dy^{3+} samples also show high emission intensities at 200 °C due to the shift of the charge transfer band. However, the drop in emission could not be observed, as a temperature dependent measurement was only possible up to 200 °C. Furthermore, no lifetimes could be measured for these samples due to weak emission intensities, since the measurement could only be carried out up to 59 °C and no overlap of the excitation wavelength with the charge transfer band takes place up to 125 °C. The low measured emission intensities of the paints can be the result of the activators dissolving out of the host lattice and being concentrated on the surface. The modification of the surface by the binder or the additives, respectively, can lead to a quenching process due to the high lattice vibrations of the binder. These can bind to the activators and cause quenching and increased multiphonon relaxation respectively.

The project has shown that one of the biggest challenges in developing an inorganic TSP is the interaction of the binder with the phosphor and not the phosphor itself. To overcome this problem, phosphors can be coated with an inorganic inert oxide such as SiO_2 or Al_2O_3, so that they no longer interact with the binder and the optical properties can be improved, as already proven in the literature [46, 47].

Nevertheless, a sprayable applicable TSP made of $(Sr_{1-x}Ca_x)AlSiN_3$:Eu^{2+} and Ceramabind 880 with a phosphor concentration of 900 mmol/L for a sensitive temperature range 150 to 450 °C could be successfully developed for wind tunnel testing, which has both fast lifetimes and high emission intensities as well as the desired machinable mechanical properties. However, due to time limitations and low availability of the phosphor, this paint could not be sprayed on a model to conduct first aerodynamic tests. Other possible applicable TSPs are the phosphors

$YVO_4:Dy^{3+}$ and $Y(V,P)O_4:Eu^{3+}$ in combination with Ceramabind 880, which could cover sensitive temperature ranges between 275 and 800 °C. However, no phosphor concentration could be fixed because the maxima of the emission intensities are unknown due to the shift of the charge transfer band. In order to determine this, measurements above 200 °C are required. For this project a heating element was ordered and a suitable heating chamber was constructed (see appendix, Figure 55), which is able to heat up to 800 °C. Due to a delay in shipping, it was not possible to carry out such measurements, so these paint samples should be reexamined at higher temperatures in future. In addition, the particle coating could improve thermal stability and luminescence properties, allowing a lower phosphor concentration to be aimed for and reducing material consumption. In search for further possible inorganic TSPs, the focus could be on phosphors with a moderately strong electron-phonon coupling, which accordingly have short lifetimes in µs and high emission intensities due to an allowed transition. In addition, particle coating could improve the thermal stability and luminescence properties, requiring a lower phosphor concentration and reducing material consumption. Furthermore, they should have a short Stokes shift, since the larger the Stokes shift, the lower the quenching temperature. In this case, the blue-emitting phosphor $BaMgAl_{10}O_{17}:Eu^{2+}$ would be of interest, which could be doped with another activator. The activator Eu^{2+} would act as a sensitizer and transfer the energy to the second activator, which emits at longer wavelengths. A further interesting phosphor is $BaSi_2N_2O_2:Eu^{2+}$, which can be examined as a possible phosphor for the further work of this project.

6 References

[1] N. P. Adamov, M. D. Brodetsky, L. G. Vasenev, V. I. Zvegintsev, I. I. Mazhul, A. M. Kharitonov, J.-C. Paulat, J. Muylaert, W. Kordulla, *Thermophys. Aeromech.* **2006**, *13 (3)*, 317 – 326. DOI: https://doi.org/10.1134/S0869864306030012

[2] Keisuke Asai, Hiroshi Kanda, Tetsuya Kunimasu, Tianshu Liu, and John P. Sullivan, *Journal of Aircraft* **1997** *(1)*, 34 – 42. DOI: https://doi.org/10.2514/2.2132

[3] T. Liu, J. P. Sullivan, K. Asai, C. Klein, Y. Egami, *Pressure and Temperature Sensitive Paints*, 2nd ed., Springer eBook Collection, Springer International Publishing; Imprint Springer, Cham **2021**.

[4] J. Brübach, C. Pflitsch, A. Dreizler, B. Atakan, *Progress in Energy and Combustion Science* **2013**, *39 (1)*, 37 – 60. DOI: https://doi.org/10.1016/j.pecs.2012.06.001

[5] A. H. Khalid, K. Kontis, *Sensors (Basel, Switzerland)* **2008**, *8 (9)*, 5673 – 5744. DOI: https://doi.org/10.3390/s8095673

[6] S. W. Allison, D. L. Beshears, T. Gadfort, T. Bencic, J. Eldridge, W. A. Hollerman, P. Boudreaux, in *19th International Congress on Instrumentation in Aerospace Simulation Facilities: Cleveland, Ohio, August 27 - 30, 2001 ; [record*, IEEE Service Center. Piscataway, NJ **2001**.

[7] https://www.aremco.com/wp-content/uploads/2015/04/A11_15.pdf (Accessed on July 30, 2022).

[8] http://www.zypcoatings.com/wp-content/uploads/ZAP-Binder.pdf (Accessed on July 30, 2022).

[9] S. M. Goedeke, W. A. Hollerman, N. P. Bergeron, S. W. Allison, M. R. Cates, T. J. Bencic, C. R. Mercer, J. I. Eldridge, in *Advances in photonic materials and devices: Proceedings of the 106th Annual Meeting of the American Ceramic Society Indianapolis, Indiana, USA (2004)*, Ceramic transactions, v. 163 (Eds: S. Bhandarkar), American Ceramic Society. Westerville, Ohio **2010**.

[10] S. J. Laurence, H. Ozawa, J. Martinez Schramm, C. S. Butler, K. Hannemann, *Exp Fluids* **2019**, *60 (4)*. DOI: https://doi.org/10.1007/s00348-019-2711-8

[11] H. Ozawa, S. J. Laurence, J. M. Schramm, A. Wagner, K. Hannemann, *Exp Fluids* **2015**, *56 (1)*. DOI: https://doi.org/10.1007/s00348-014-1853-y

[12] T. Sugimoto, Y. Sugioka, D. Numata, H. Nagai, K. Asai, *AIAA Journal* **2017**, *55 (4)*, 1460 – 1464. DOI: https://doi.org/10.2514/1.J054985

[13] M. Kasai, D. Sasaki, T. Nagata, T. Nonomura, K. Asai, *Sensors (Basel, Switzerland)* **2021**, *21 (9)*. DOI: https://doi.org/10.3390/s21093187

[14] J. Gößling, T. Ahlefeldt, M. Hilfer, *Experimental Thermal and Fluid Science* **2020**, *112*, 109915. DOI: https://doi.org/10.1016/j.expthermflusci.2019.109915

[15] https://www.tec-science.com/de/thermodynamik-waermelehre/temperatur/planckssches-strahlungsgesetz/ (Accessed on July 30, 2022).

[16] H. Herwig, *Wärmeübertragung A-Z: Systematische und ausführliche Erläuterungen wichtiger Größen und Konzepte*, VDI-Buch, Springer Berlin Heidelberg, Berlin, Heidelberg, s.l. **2000**.

[17] M. Majka, T. Majka, in *Proceedings of The 2nd World Sustainability Forum*, MDPI. Basel, Switzerland **2012 - 2012**.

[18] https://www.fh-muenster.de/ciw/personal/professoren/juestel/pisa-vis.php (Accessed on August 02, 2022).

[19] S. W. Allison, G. T. Gillies, *Review of Scientific Instruments* **1997**, *68 (7)*, 2615 – 2650. DOI: https://doi.org/10.1063/1.1148174

[20] *Anorganische Chemie* (Eds: E. Riedel, C. Janiak), De Gruyter **2022**.

[21] C. Janiak, D. Gudat, P. Kurz, *Moderne anorganische Chemie*, 5th ed., De Gruyter Studium, De Gruyter, Berlin, Boston **2018**.
[22] A. Reinhardt, A. Zych, I. Köhler, B. Albert, *Journal of Luminescence* **2020**, *218*, 116833. DOI: https://doi.org/10.1016/j.jlumin.2019.116833
[23] G. Blasse, B. C. Grabmaier, *Luminescent materials: With 31 tables*, Springer, Berlin, Heidelberg **1994**.
[24] E. N. Harvey, *A history of luminescence: From the earliest times until 1900*, Dover phoenix editions, Dover Publ, Mineola, NY **2005**.
[25] *Luminescence: From theory to applications* (Eds: C. Ronda), Wiley-VCH, Weinheim **2008**.
[26] Florian Baur, *Rotemittierende Leuchtstoffe mit hohem Lumenäquivalent als Konvertermaterialien in warmweißen leuchtstoffkonvertierten Leuchtdioden* **2017**.
[27] B. Weber, *Koordinationschemie*, Springer Berlin Heidelberg, Berlin, Heidelberg **2021**.
[28] T. Jüstel, S. Schwung, *Leuchtstoffe, Lichtquellen, Laser, Lumineszenz*, Springer Berlin Heidelberg, Berlin, Heidelberg **2019**.
[29] Liudmyla Chepyga, *Development of new phosphors for high temperature thermometry* **2018**.
[30] Dominik Uhlich, *Kristallographische und spektroskopische Untersuchungen an Eu3+-dotierten Molybdaten als potentieller´Konverter für LEDs* **2009**.
[31] J.-N. Keil, H. Jenneboer, T. Jüstel, *Journal of Luminescence* **2021**, *238*, 118307. DOI: https://doi.org/10.1016/j.jlumin.2021.118307
[32] B. Malysa, A. Meijerink, T. Jüstel, *Journal of Luminescence* **2016**, *171*, 246 – 253. DOI: https://doi.org/10.1016/j.jlumin.2015.10.042
[33] David Enseling, *Untersuchungen zur Photolumineszenz-Quanteneffizienzmessung an mikrokristallinen* Dissertationsschrift **2016**.
[34] M. Hilfer, M. Constantini, U. Henne, U. Beifuss, *Development of sensors for ambient temperature measurement* **2018**.
[35] C. J. Sweeney, B. C. Chynoweth, J. Edelman, S. P. Schneider, in *American Institute of Aeronautics and Astronautics 2016? – 54th AIAA Aerospace Sciences*.
[36] http://lab.fs.uni-lj.si/lat/uploads/metrologija/o_hrapavosti_Mahr_publikacija.pdf (Accessed on July 31, 2022).
[37] M. Bitter, M. Hilfer, T. Schubert, C. Klein, R. Niehuis, *Sensors (Basel, Switzerland)* **2022**, *22 (2)*. DOI: https://doi.org/10.3390/s22020657
[38] I. E. Kolesnikov, A. A. Kalinichev, M. A. Kurochkin, E. V. Golyeva, A. S. Terentyeva, E. Y. Kolesnikov, E. Lähderanta, *Scientific reports* **2019**, *9 (1)*, 2043. DOI: https://doi.org/10.1038/s41598-019-38774-6
[39] M. Klimczak, M. Malinowski, J. Sarnecki, R. Piramidowicz, *Journal of Luminescence* **2009**, *129 (12)*, 1869 – 1873. DOI: https://doi.org/10.1016/j.jlumin.2009.04.073
[40] Y. H. Zhou, J. Lin, *Optical Materials* **2005** *(27)*, 1426 – 1432. DOI: https://doi.org/10.1016/j.optmat.2004.10.006
[41] I. E. Kolesnikov, A. A. Kalinichev, M. A. Kurochkin, D. V. Mamonova, E. Y. Kolesnikov, E. Lähderanta, *J. Phys. Chem. C* **2019**, *123 (8)*, 5136 – 5143. DOI: https://doi.org/10.1021/acs.jpcc.9b00284
[42] M. Wu, H. Park, E. G. Lee, S. Lee, Y. J. Hong, S. Choi, *Materials (Basel, Switzerland)* **2020**, *13 (15)*. DOI: https://doi.org/10.3390/ma13153270
[43] X. Li, Q. Li, J. Wang, S. Yang, *Materials Science and Engineering B* **2005** *(131)*, 32 – 35. DOI: https://doi.org/10.1016/j.mseb.2005.12.022

[44] R. Zheng, J. Ding, Q. Zhang, B. Lin, Z. Wang, C. Liu, P. Lv, Yu, Kehan, Wei, Wei, *The American Ceramic Society* **2019** *(102)*, 3510 – 3516. DOI: https://doi.org/10.1111/jace.16210

[45] M. G. Nikolić, D. J. Jovanović, M. D. Dramićanin, *Applied optics* **2013**, *52 (8)*, 1716 – 1724. DOI: https://doi.org/10.1364/AO.52.001716

[46] J. Zhuang, Z. Xia, H. Liu, Z. Zhang, L. Liao, *Applied Surface Science* **2011**, *257 (9)*, 4350 – 4353. DOI: https://doi.org/10.1016/j.apsusc.2010.12.055

[47] S. H. Sohn, J. H. Lee, S. M. Lee, *Journal of Luminescence* **2009**, *129 (5)*, 478 – 481. DOI: https://doi.org/10.1016/j.jlumin.2008.11.022

7 Appendix

Table 19: Weights for the synthesis of YAG:Eu^{3+} and YVO4:Dy^{3+}

Chemical	Target weight / g	Actual weight / g
Y_2O_3	4.9789	4.9792
$Al(NO_3)_3 \cdot 9H_2O$	28.1348	28.1347
Eu_2O_3	0.1584	0.1585
TRIS	25.9569	25.9564
YAG:Eu^{3+} (15 mmol)	8.9609	8.1621

Chemical	Target weight / g	Actual weight / g
Y_2O_3	4.9789	4.9788
$Al(NO_3)_3 \cdot 9H_2O$	28.1348	28.1348
Eu_2O_3	0.1584	0.1584
TRIS	25.9569	29.0734
YAG:Eu^{3+} (15 mmol)	8.9609	8.1621

Chemical	Target weight / g	Actual weight / g
Y_2O_3	3.8726	3.8719
NH_4VO_3	4.0943	4.0942
Dy_2O_3	0.1306	0.1306
TRIS	50.8788	50.8789
Na_2CO_3	0.0543 – 0.1086	0.0926
YVO_4:Dy^{3+} (35 mmol)	7.1860	6.92

Chemical	Target weight / g	Actual weight / g
Y_2O_3	1.6597	1.6601
NH_4VO_3	1.7547	1.7548
Dy_2O_3	0.0560	0.0560
TRIS	21.8052	21.8046
Na_2CO_3	0.0555 – 0.111	0.0946
YVO_4:Dy^{3+} (15 mmol)	3.0797	2.8872

Chemical	Target weight / g	Actual weight / g
Y_2O_3	1.6597	1.6602
NH_4VO_3	1.7547	1.7547
Dy_2O_3	0.0560	0.0562
TRIS	21.8052	21.8052
Na_2CO_3	0.0532 – 0.1064	0.0933
YVO_4:Dy^{3+} (15 mmol)	3.0797	2.7142

Figure 41: Particle size distributions of the examined phosphors

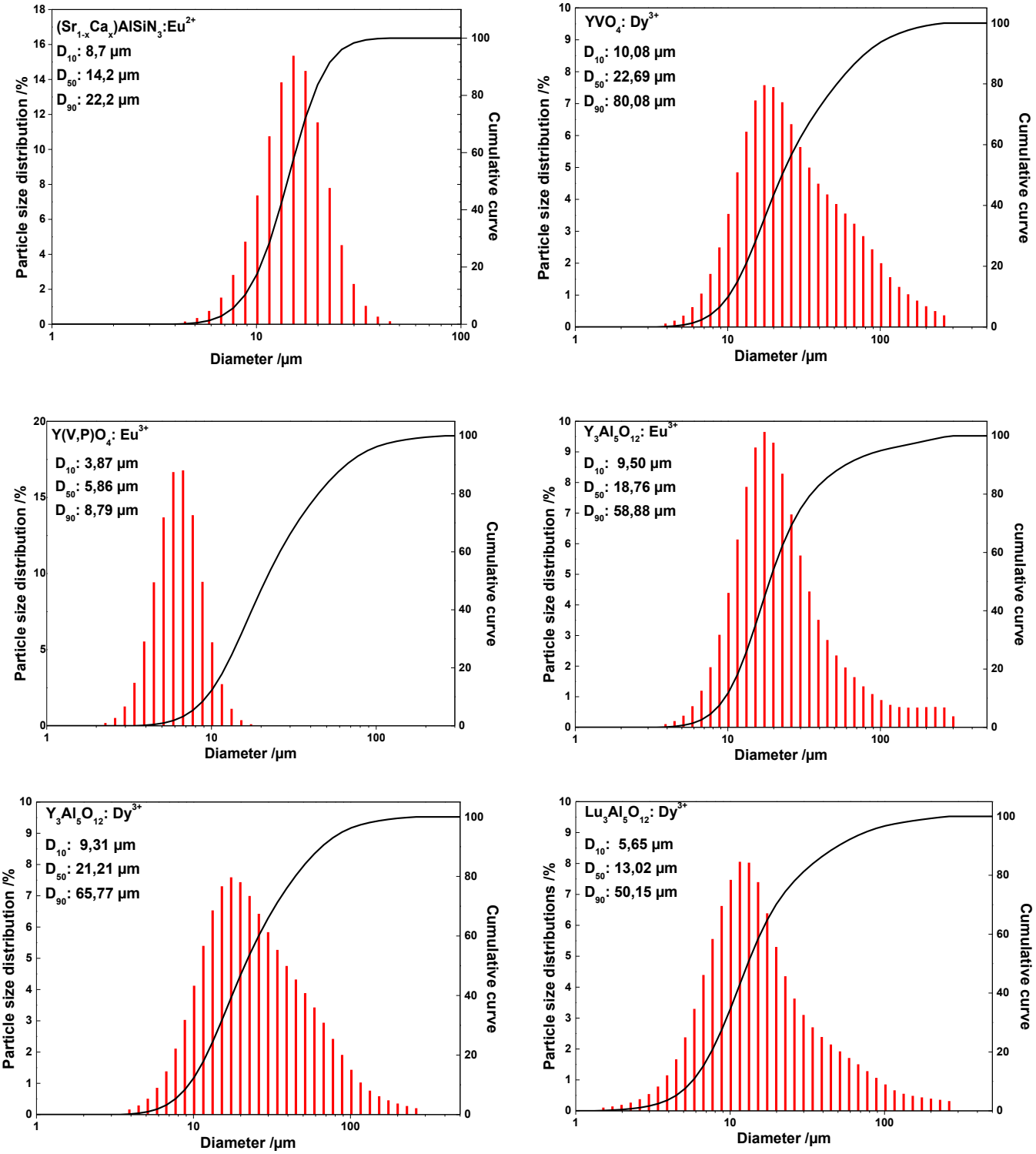

Figure 42: Laboratory report for sample preparations numbers 20220524-1 to -3

20220524-1: In a 30 ml test tube 188.8 mg Y_2O_3:Eu^{3+} (c = 100 mmol·L^{-1}) was dissolved in 5 ml Ceramabind 643-1 under stirring. The mixture was stirred for 10 min with a magnetic stirrer, treated for 20 min in an ultrasonic bath, then transferred to a spray gun and sprayed under a pressure of 1.2 bar onto one 1x1 cm and two 3x3 cm aluminum plates.

20220524-2: In a 30 ml test tube 566.6 mg Y_2O_3:Eu^{3+} (c = 300 mmol·L^{-1}) was dissolved in 5 ml Ceramabind 643-1 under stirring. The mixture was stirred for 10 min with a magnetic stirrer, treated for 20 min in an ultrasonic bath, then transferred to a spray gun and sprayed under a pressure of 1.2 bar onto one 1x1 cm and two 3x3 cm aluminum plates.

20220524-3: In a 30 ml test tube 1.3222 g Y_2O_3:Eu^{3+} (c = 700 mmol·L^{-1}) was dissolved in 5 ml Ceramabind 643-1 under stirring. The mixture was stirred for 10 min with a magnetic stirrer, treated for 20 min in an ultrasonic bath, then transferred to a spray gun and sprayed under a pressure of 1.2 bar onto one 1x1 cm and two 3x3 cm aluminum plates.

All Ceramabind 643-1 samples were air dried for 2 h, cured for 1.5 h at 95 °C, 1.5 h at 175 °C and 1 h at 260 °C.

Figure 43: Laboratory report for sample preparations numbers 20220608-1 to -8

20220608-1: In a 30 ml test tube 188.8 mg Y_2O_3:Eu^{3+} (c = 100 mmol·L^{-1}) was dissolved in 5 ml ZAP Binder under stirring. The mixture was stirred for 10 min with a magnetic stirrer, treated for 20 min in an ultrasonic bath, then transferred to a spray gun and sprayed under a pressure of 1.2 bar onto two 3x3 cm Ni-steel alloy plates.

20220608-2: In a 30 ml test tube 566.6 mg Y_2O_3:Eu^{3+} (c = 300 mmol·L^{-1}) was dissolved in 5 ml ZAP Binder under stirring. The mixture was stirred for 10 min with a magnetic stirrer, treated for 20 min in an ultrasonic bath, then transferred to a spray gun and sprayed under a pressure of 1.2 bar onto two 3x3 cm Ni-steel alloy plates.

20220608-3: In a 30 ml test tube 1.3222 g Y_2O_3:Eu^{3+} (c = 700 mmol·L^{-1}) was dissolved in 5 ml ZAP Binder under stirring. The mixture was stirred for 10 min with a magnetic stirrer, treated for 20 min in an ultrasonic bath, then transferred to a spray gun and sprayed under a pressure of 1.2 bar onto two 3x3 cm Ni-steel alloy plates.

20220608-4: In a 30 ml test tube 1.3224 g Y_2O_3:Eu^{3+} (c = 700 mmol·L^{-1}) was dissolved in 5 ml ZAP Binder and 5 ml H_2O under stirring. The mixture was stirred for 10 min with a magnetic

stirrer, treated for 20 min in an ultrasonic bath, then transferred to a spray gun and sprayed under a pressure of 1.2 bar onto two 3x3 cm Ni-steel alloy plates.

20220608-5: In a 30 ml test tube 188.5 mg $Y_2O_3:Eu^{3+}$ (c = 100 mmol·L^{-1}) was dissolved in 5 ml Ceramabind 880 under stirring. The mixture was stirred for 10 min with a magnetic stirrer, treated for 20 min in an ultrasonic bath, then transferred to a spray gun and sprayed under a pressure of 1.2 bar onto two 3x3 cm Ni-steel alloy plates.

20220608-6: In a 30 ml test tube 566.6 mg $Y_2O_3:Eu^{3+}$ (c = 300 mmol·L^{-1}) was dissolved in 5 ml Ceramabind 880 under stirring. The mixture was stirred for 10 min with a magnetic stirrer, treated for 20 min in an ultrasonic bath, then transferred to a spray gun and sprayed under a pressure of 1.2 bar onto two 3x3 cm Ni-steel alloy plates.

20220608-7: In a 30 ml test tube 1.3221 g $Y_2O_3:Eu^{3+}$ (c = 700 mmol·L^{-1}) was dissolved in 5 ml Ceramabind 880 under stirring. The mixture was stirred for 10 min with a magnetic stirrer, treated for 20 min in an ultrasonic bath, then transferred to a spray gun and sprayed under a pressure of 1.2 bar onto two 3x3 cm Ni-steel alloy plates.

20220608-8: In a 30 ml test tube 1.3226 g $Y_2O_3:Eu^{3+}$ (c = 700 mmol·L^{-1}) was dissolved in 2.5 ml Ceramabind 880 and 2.5 ml H_2O under stirring. The mixture was stirred for 10 min with a magnetic stirrer, treated for 20 min in an ultrasonic bath, then transferred to a spray gun and sprayed under a pressure of 1.2 bar onto two 3x3 cm Ni-steel alloy plates.

All Ceramabind 880 samples were air dried for 2 h and cured for 1 h at 230 °C.

All ZAP binders were air dried for 2 h and cured for 1 h at 600 °C.

Figure 44: Laboratory report for sample preparations numbers 20220520-1 to -5

20220520-1: In a 30 ml test tube 615.9 mg $YVO_4:Dy^{3+}$ (c = 300 mmol·L^{-1}) was dissolved in 10 ml Ceramabind 643-1 under stirring. The mixture was stirred for 10 min with a magnetic stirrer, treated for 20 min in an ultrasonic bath, then transferred to a spray gun and sprayed under a pressure of 1.2 bar onto one 1x1 cm and two 3x3 cm aluminum plates.

20220520-2: In a 30 ml test tube 425.6 mg $LuAG:Dy^{3+}$ (c = 100 mmol·L^{-1}) was dissolved in 5 ml Ceramabind 643-1 under stirring. The mixture was stirred for 10 min with a magnetic stirrer, treated for 20 min in an ultrasonic bath, then transferred to a spray gun and sprayed under a pressure of 1.2 bar onto one 1x1 cm and two 3x3 cm aluminum plates.

20220520-3: In a 30 ml test tube 616.2 mg $Y(V,P)O_4:Eu^{3+}$ (c = 300 mmol·L^{-1}) was dissolved in 10 ml Ceramabind 643-1 under stirring. The mixture was stirred for 10 min with a magnetic stirrer, treated for 20 min in an ultrasonic bath, then transferred to a spray gun and sprayed under a pressure of 1.2 bar onto one 1x1 cm and two 3x3 cm aluminum plates.

20220520-4: In a 30 ml test tube 1.7923 g $YAG:Eu^{3+}$ (c = 300 mmol·L^{-1}) was dissolved in 10 ml Ceramabind 643-1 under stirring. The mixture was stirred for 10 min with a magnetic stirrer, treated for 20 min in an ultrasonic bath, then transferred to a spray gun and sprayed under a pressure of 1.2 bar onto one 1x1 cm and two 3x3 cm aluminum plates.

20220520-5: In a 30 ml test tube 297.7 mg $YAG:Dy^{3+}$ (c = 100 mmol·L^{-1}) was dissolved in 10 ml Ceramabind 643-1 under stirring. The mixture was stirred for 10 min with a magnetic stirrer, treated for 20 min in an ultrasonic bath, then transferred to a spray gun and sprayed under a pressure of 1.2 bar onto one 1x1 cm and two 3x3 cm aluminum plates.

All Ceramabind 643-1 samples were air dried for 2 h, cured for 1.5 h at 95 °C, 1.5 h at 175 °C and 1 h at 260 °C.

Figure 45: Laboratory report for sample preparations numbers 20220616-1 to -7

20220616-1: In a 30 ml test tube 307.6 mg $YVO_4:Dy^{3+}$ (c = 300 mmol·L^{-1}) was dissolved in 2.5 ml Ceramabind 880 and 2.5 ml H_2O under stirring. The mixture was stirred for 10 min with a magnetic stirrer, treated for 20 min in an ultrasonic bath, then transferred to a spray gun and sprayed under a pressure of 1.2 bar onto two 3x3 cm Ni-steel alloy plates.

20220616-2: In a 30 ml test tube 239.7 mg $(Ca,Sr)AlSiN_3:Eu^{2+}$ (c = 300 mmol·L^{-1}) was dissolved in 2.5 ml Ceramabind 880 and 2.5 ml H_2O under stirring. The mixture was stirred for 10 min with a magnetic stirrer, treated for 20 min in an ultrasonic bath, then transferred to a spray gun and sprayed under a pressure of 1.2 bar onto two 3x3 cm Ni-steel alloy plates.

20220616-3: In a 30 ml test tube 308 mg $Y(V,P)O_4:Eu^{3+}$ (c = 300 mmol·L^{-1}) was dissolved in 2.5 ml Ceramabind 880 and 2.5 ml H_2O under stirring. The mixture was stirred for 10 min with a magnetic stirrer, treated for 20 min in an ultrasonic bath, then transferred to a spray gun and sprayed under a pressure of 1.2 bar onto two 3x3 cm Ni-steel alloy plates.

20220616-4: In a 30 ml test tube 307,8 mg $YVO_4:Dy^{3+}$ (c = 300 mmol·L^{-1}) was dissolved in 2.5 ml Ceramabind 880 and 2.5 ml H_2O under stirring. The mixture was stirred for 10 min with a magnetic stirrer, treated for 20 min in an ultrasonic bath, then transferred to a spray gun and sprayed under a pressure of 1.2 bar onto two 3x3 cm Ni-steel alloy plates.

20220616-5: In a 30 ml test tube 308 mg $Y(V,P)O_4:Eu^{3+}$ (c = 300 mmol·L^{-1}) was dissolved in 2.5 ml ZAP Binder and 2.5 ml H_2O under stirring. The mixture was stirred for 10 min with a magnetic stirrer, treated for 20 min in an ultrasonic bath, then transferred to a spray gun and sprayed under a pressure of 1.2 bar onto two 3x3 cm Ni-steel alloy plates.

20220616-6: In a 30 ml test tube 896,1 mg $YAG:Eu^{3+}$ (c = 300 mmol·L^{-1}) was dissolved in 2.5 ml ZAP Binder and 2.5 ml H_2O under stirring. The mixture was stirred for 10 min with a magnetic stirrer, treated for 20 min in an ultrasonic bath, then transferred to a spray gun and sprayed under a pressure of 1.2 bar onto two 3x3 cm Ni-steel alloy plates.

20220616-7: In a 30 ml test tube 297,75 mg $YAG:Dy^{3+}$ (c = 300 mmol·L^{-1}) was dissolved in 2.5 ml ZAP Binder and 2.5 ml H_2O under stirring. The mixture was stirred for 10 min with a magnetic stirrer, treated for 20 min in an ultrasonic bath, then transferred to a spray gun and sprayed under a pressure of 1.2 bar onto two 3x3 cm Ni-steel alloy plates.

All Ceramabind 880 samples were air dried for 2 h and cured for 1 h at 230 °C.

All ZAP Binder samples were air dried for 2 h, no curing necessary.

Figure 46: Sample with ZAP-Binder before and after heating up to 200 °C

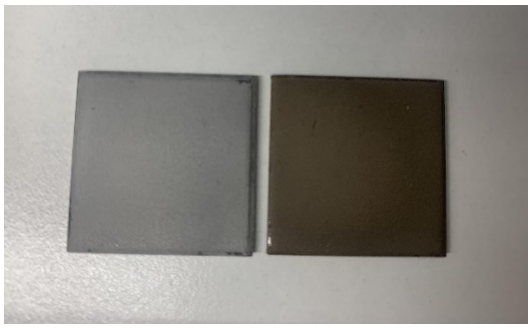

Figure 47: Temperature dependent emission spectra of the samples 20220520-1,4 and 20220616-1,3 to -5

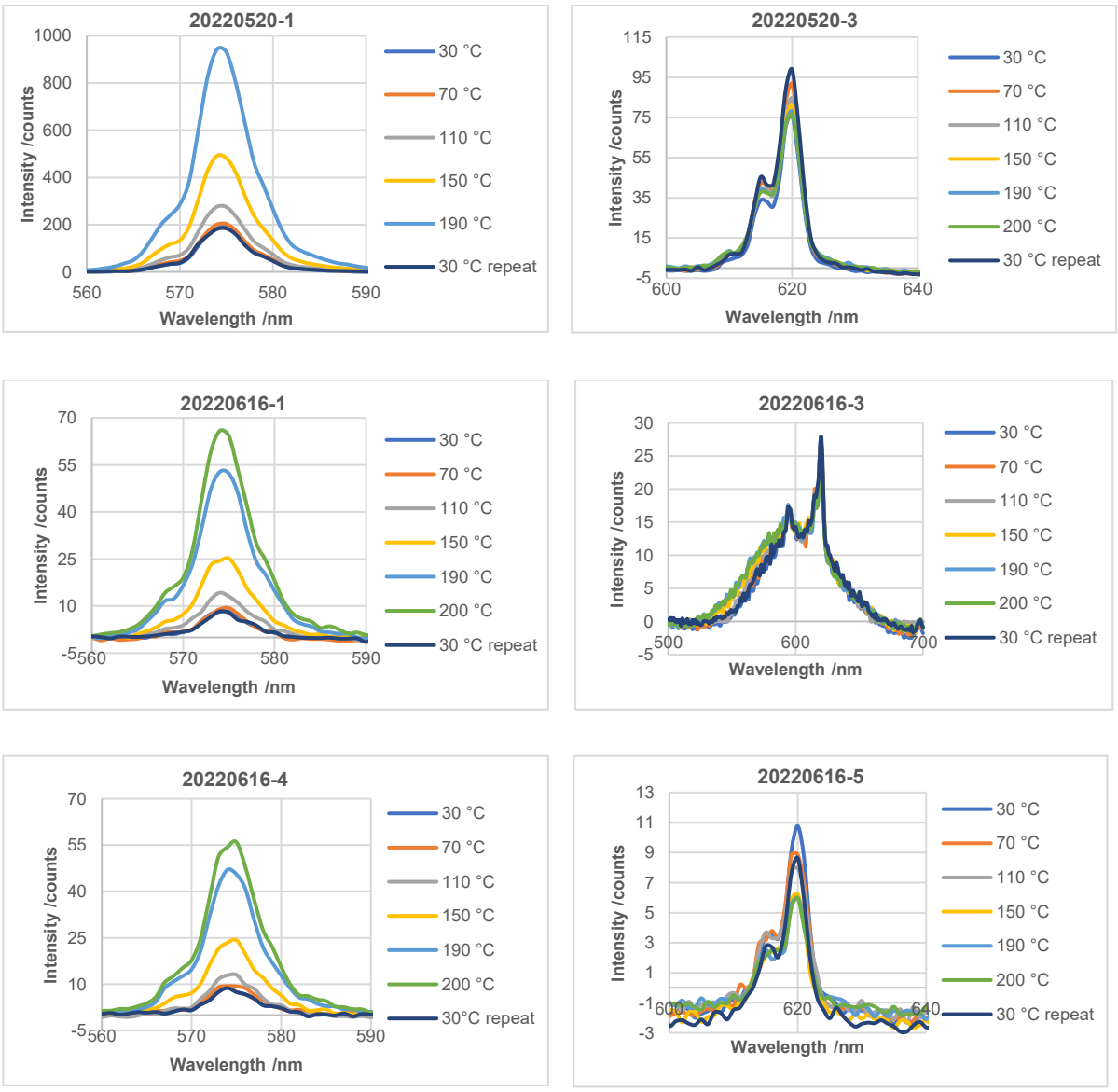

Figure 48: Particle size distributions of the examined phosphors after grounding

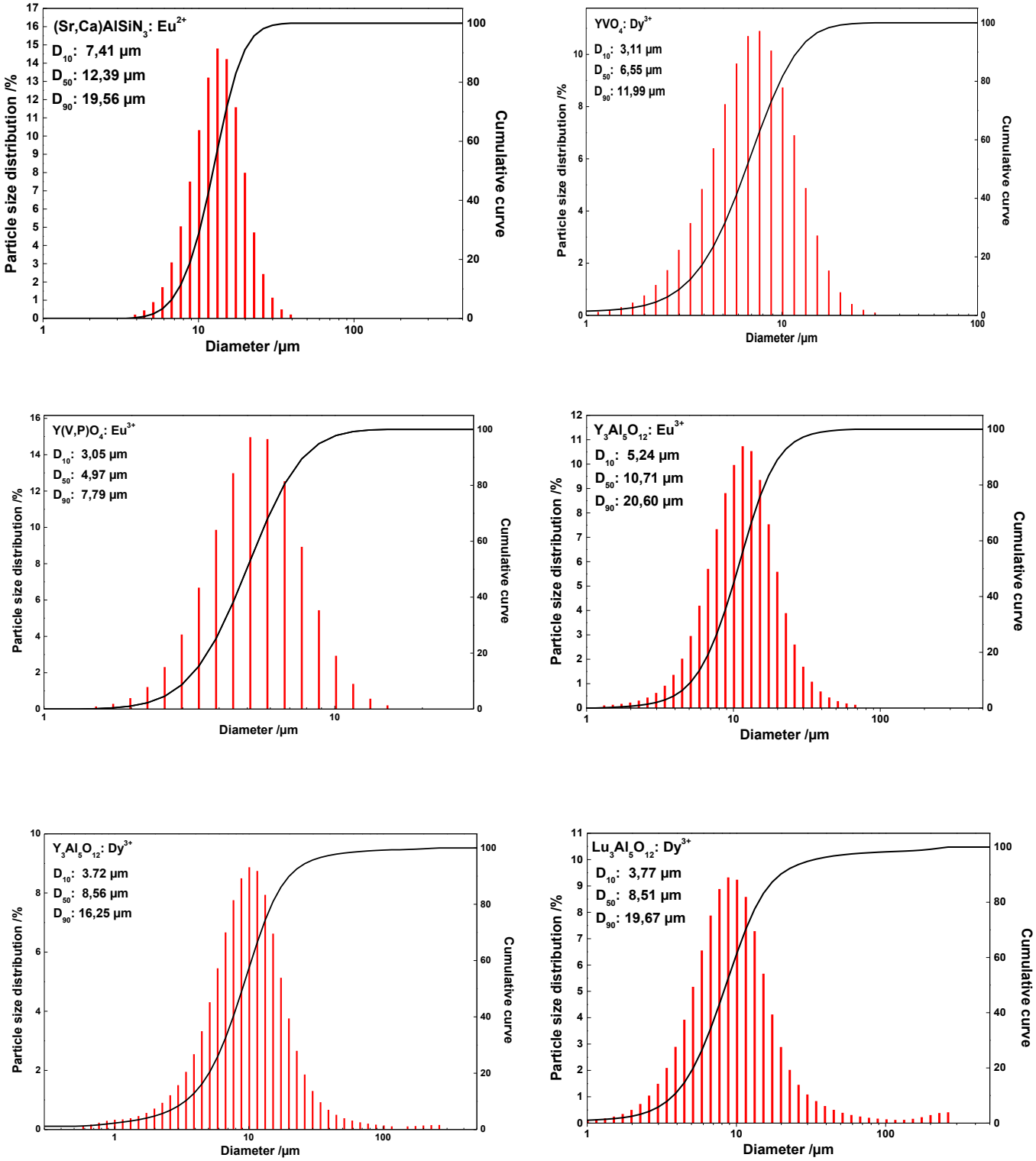

Figure 49: Laboratory report for sample preparations numbers 20220630-1 to -13

20220630-1: In a 30 ml test tube 615,3, mg $YVO_4:Dy^{3+}$ (c = 300 mmol·L^{-1}) was dissolved in 10 ml Ceramabind 643-1 under stirring. The mixture was stirred for 10 min with a magnetic stirrer, treated for 20 min in an ultrasonic bath, then transferred to a spray gun and sprayed under a pressure of 1.2 bar onto two 3x3 cm Ni-steel alloy plates.

20220630-2: In a 30 ml test tube 307,9 mg $YVO_4:Dy^{3+}$ (c = 300 mmol·L^{-1}) was dissolved in 2.5 ml Ceramabind 880 and 2.5 ml H_2O under stirring. The mixture was stirred for 10 min with a magnetic stirrer, treated for 20 min in an ultrasonic bath, then transferred to a spray gun and sprayed under a pressure of 1.2 bar onto two 3x3 cm Ni-steel alloy plates.

20220630-3: In a 30 ml test tube 307,5 mg $YVO_4:Dy^{3+}$ (c = 300 mmol·L^{-1}) was dissolved in 2.5 ml ZAP Binder and 2.5 ml H_2O under stirring. The mixture was stirred for 10 min with a magnetic stirrer, treated for 20 min in an ultrasonic bath, then transferred to a spray gun and sprayed under a pressure of 1.2 bar onto two 3x3 cm Ni-steel alloy plates.

20220630-4: In a 30 ml test tube 616,1 mg $Y(V,P)O_4:Eu^{3+}$ (c = 300 mmol·L^{-1}) was dissolved in 10 ml Ceramabind 643-1 under stirring. The mixture was stirred for 10 min with a magnetic stirrer, treated for 20 min in an ultrasonic bath, then transferred to a spray gun and sprayed under a pressure of 1.2 bar onto two 3x3 cm Ni-steel alloy plates.

20220630-5: In a 30 ml test tube 308,1 mg $Y(V,P)O_4:Eu^{3+}$ (c = 300 mmol·L^{-1}) was dissolved in 2.5 ml Ceramabind 880 and 2.5 ml H_2O under stirring. The mixture was stirred for 10 min with a magnetic stirrer, treated for 20 min in an ultrasonic bath, then transferred to a spray gun and sprayed under a pressure of 1.2 bar onto two 3x3 cm Ni-steel alloy plates.

20220630-6: In a 30 ml test tube 307,9 mg $Y(V,P)O_4:Eu^{3+}$ (c = 300 mmol·L^{-1}) was dissolved in 2.5 ml ZAP Binder and 2.5 ml H_2O under stirring. The mixture was stirred for 10 min with a magnetic stirrer, treated for 20 min in an ultrasonic bath, then transferred to a spray gun and sprayed under a pressure of 1.2 bar onto two 3x3 cm Ni-steel alloy plates.

20220630-7: In a 30 ml test tube 896,1 mg $YAG:Eu^{3+}$ (c = 300 mmol·L^{-1}) was dissolved in 2.5 ml Ceramabind 643-1 and 2.5 ml H_2O under stirring. The mixture was stirred for 10 min with a magnetic stirrer, treated for 20 min in an ultrasonic bath, then transferred to a spray gun and sprayed under a pressure of 1.2 bar onto two 3x3 cm Ni-steel alloy plates.

20220630-8: In a 30 ml test tube 896,0 mg $YAG:Eu^{3+}$ (c = 300 mmol·L^{-1}) was dissolved in 2.5 ml ZAP Binder and 2.5 ml H_2O under stirring. The mixture was stirred for 10 min with a

magnetic stirrer, treated for 20 min in an ultrasonic bath, then transferred to a spray gun and sprayed under a pressure of 1.2 bar onto two 3x3 cm Ni-steel alloy plates.

20220630-9: In a 30 ml test tube 239,7 mg (Ca,Sr)$AlSiN_3$:Eu^{2+} (c = 300 mmol·L^{-1}) was dissolved in 2.5 ml Ceramabind 880 and 2.5 ml H_2O under stirring. The mixture was stirred for 10 min with a magnetic stirrer, treated for 20 min in an ultrasonic bath, then transferred to a spray gun and sprayed under a pressure of 1.2 bar onto two 3x3 cm Ni-steel alloy plates.

20220630-10: In a 30 ml test tube 1,1769 g LuAG:Dy^{3+} (c = 276 mmol·L^{-1}) was dissolved in 2.5 ml Ceramabind 643-1 and 2.5 ml H_2O under stirring. The mixture was stirred for 10 min with a magnetic stirrer, treated for 20 min in an ultrasonic bath, then transferred to a spray gun and sprayed under a pressure of 1.2 bar onto two 3x3 cm Ni-steel alloy plates.

20220630-11: In a 30 ml test tube 539,0 mg YAG:Dy^{3+} (c = 180 mmol·L^{-1}) was dissolved in 2.5 ml ZAP Binder and 2.5 ml H_2O under stirring. The mixture was stirred for 10 min with a magnetic stirrer, treated for 20 min in an ultrasonic bath, then transferred to a spray gun and sprayed under a pressure of 1.2 bar onto two 3x3 cm Ni-steel alloy plates.

All Ceramabind 643-1 samples were air dried for 2 h, cured for 1.5 h at 95 °C, 1 h at 175 °C and 1 h at 260 °C.

All Ceramabind 880 samples were air dried for 2 h and cured for 1 h at 230 °C.

All ZAP Binder samples were air dried for 2 h, no curing necessary.

Figure 50: Temperature dependent emission spectra pf the samples 20220630-1 to -9

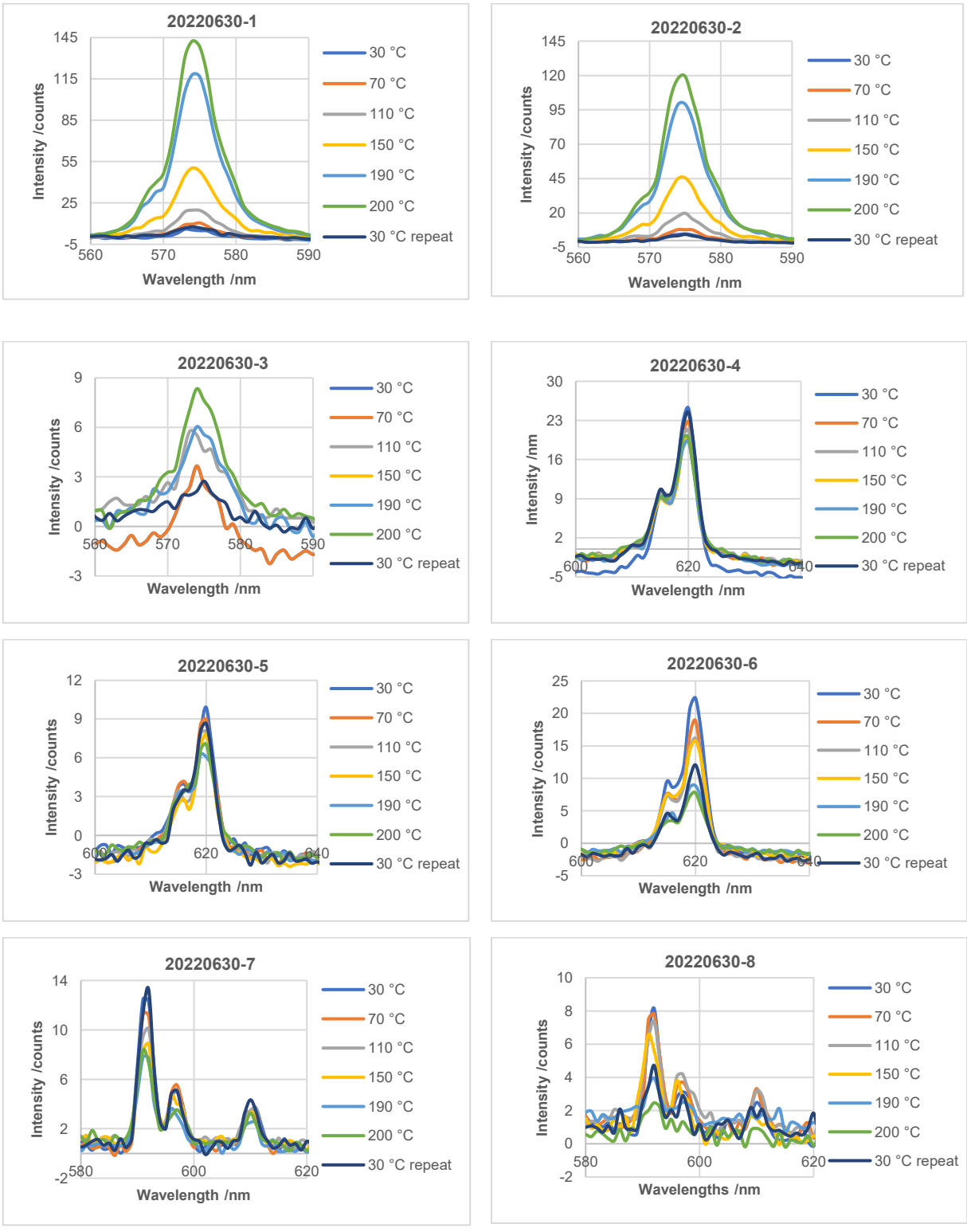

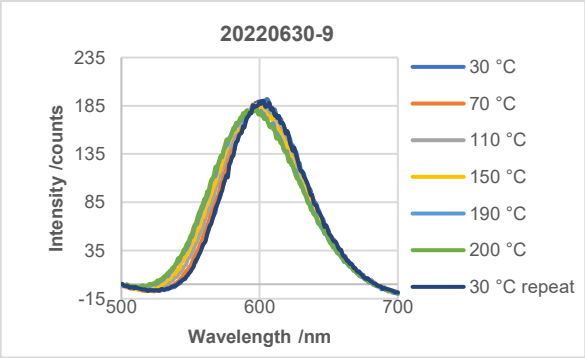

Figure 51: Laboratory report for sample preparations numbers 20220707-1 to -4

20220707-1,2: In a 30 ml test tube 1,4366 g (Ca,Sr)$AlSiN_3$:Eu^{2+} (c = 900 mmol·L^{-1}) was dissolved in 5 ml Ceramabind 880 and 5 ml H_2O under stirring. The mixture was stirred for 10 min with a magnetic stirrer, treated for 20 min in an ultrasonic bath and then two 3x3 cm Ni-steel alloy plates each were coated with 8 layers (1) and 14 layers (2) under a pressure of 1.2 bar.

20220707-3,4: In a 30 ml test tube 2,3970 g (Ca,Sr)$AlSiN_3$:Eu^{2+} (c = 1500 mmol·L^{-1}) was dissolved in 5 ml Ceramabind 880 and 5 ml H_2O under stirring. The mixture was stirred for 10 min with a magnetic stirrer, treated for 20 min in an ultrasonic bath and then two 3x3 cm Ni-steel alloy plates each were coated with 8 layers (3) and 12 layers (4) under a pressure of 1.2 bar.

All Ceramabind 880 samples were air dried for 2 h and cured for 1 h at 230 °C.

Figure 52: Laboratory report for sample preparations numbers 20220713-1 to -10

20220713-1,2: In a 30 ml test tube 1,7921 g YAG:Eu^{3+} (c = 600 mmol·L^{-1}) was dissolved in 5 ml Ceramabind 643-1 and 5 ml H_2O under stirring. The mixture was stirred for 10 min with a magnetic stirrer, treated for 20 min in an ultrasonic bath and then two 3x3 cm Ni-steel alloy plates each were coated with 10 layers (1) and 14 layers (2) under a pressure of 1.2 bar.

20220713-3,4: In a 30 ml test tube 1,8459 g YVO_4:Dy^{3+} (c = 900 mmol·L^{-1}) was dissolved in 5 ml Ceramabind 880 and 5 ml H_2O under stirring. The mixture was stirred for 10 min with a magnetic stirrer, treated for 20 min in an ultrasonic bath and then two 3x3 cm Ni-steel alloy plates each were coated with 8 layers (3) and 14 layers (4) under a pressure of 1.2 bar.

20220713-5,6: In a 30 ml test tube 3,0765 g $YVO_4:Dy^{3+}$ (c = 1200 mmol·L^{-1}) was dissolved in 5 ml Ceramabind 880 and 5 ml H_2O under stirring. The mixture was stirred for 10 min with a magnetic stirrer, treated for 20 min in an ultrasonic bath and then two 3x3 cm Ni-steel alloy plates each were coated with 6 layers (5) and 10 layers (6) under a pressure of 1.2 bar.

20220713-7,8: In a 30 ml test tube 1,2320 g $Y(V,P)O_4:Eu^{3+}$ (c = 900 mmol·L^{-1}) was dissolved in 5 ml Ceramabind 880 and 5 ml H_2O under stirring. The mixture was stirred for 10 min with a magnetic stirrer, treated for 20 min in an ultrasonic bath and then two 3x3 cm Ni-steel alloy plates each were coated with 8 layers (7) and 14 layers (8) under a pressure of 1.2 bar.

20220713-9,10: In a 30 ml test tube 3,08 g $Y(V,P)O_4:Eu^{3+}$ (c = 1200 mmol·L^{-1}) was dissolved in 10 ml Ceramabind 880 and 2 ml H_2O under stirring. The mixture was stirred for 10 min with a magnetic stirrer, treated for 20 min in an ultrasonic bath and then two 3x3 cm Ni-steel alloy plates each were coated with 6 layers (9) and 10 layers (10) under a pressure of 1.2 bar.

All Ceramabind 643-1 samples were air dried for 2 h, cured for 1.5 h at 95 °C, 1 h at 175 °C and 1 h at 260 °C.

All Ceramabind 880 samples were air dried for 2 h and cured for 1 h at 230 °C.

Figure 53: Laboratory report for sample preparations numbers 20220719-1,2

20220719-1,2: In a 30 ml test tube 5,3763 g $YAG:Eu^{3+}$ (c = 900 mmol·L^{-1}) was dissolved in 5 ml Ceramabind 643-1 and 5 ml H_2O under stirring. The mixture was stirred for 10 min with a magnetic stirrer, treated for 20 min in an ultrasonic bath and then two 3x3 cm Ni-steel alloy plates each were coated with 8 layers (1) and 14 layers (2) under a pressure of 1.2 bar.

All Ceramabind 643-1 samples were air dried for 2 h, cured for 1.5 h at 95 °C, 1 h at 175 °C and 1 h at 260 °C.

Figure 54: Temperature dependent emission spectra of the samples 20220707-1,3, 20220713-1 to -9 and 20220719-1,2

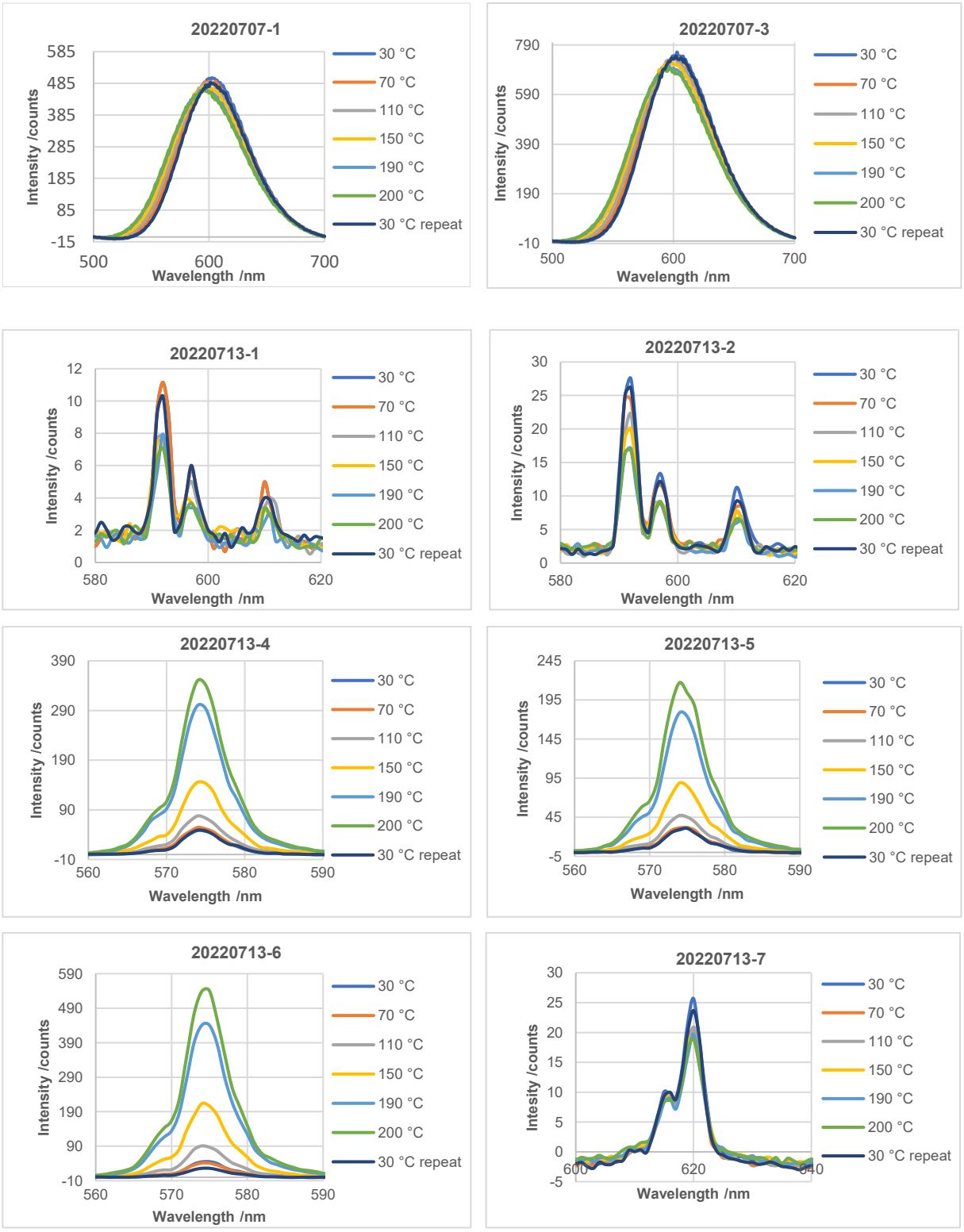

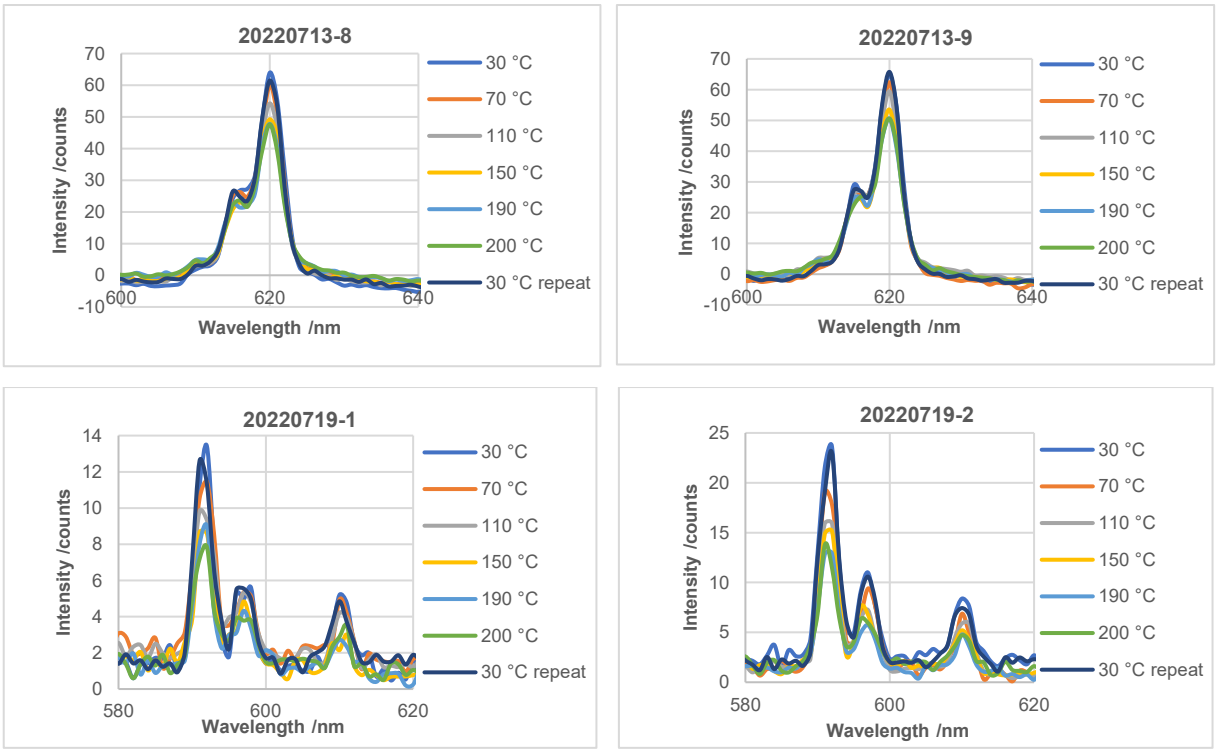

Figure 55: Calculated temperature sensitivities of the samples 20220707-1 to -3, 20220713-2 and 20220719-1,2

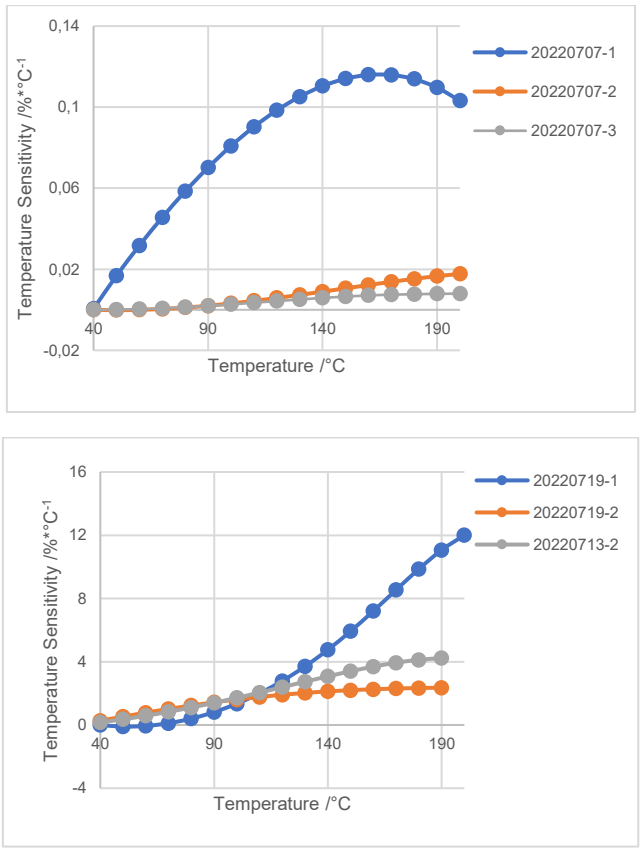

Figure 56: Construction plan for the heating chamber